Robust Control of Brake Systems with Decoupled Architecture

Dissertation zur Erlangung des
akademischen Grades Doktor-ingenieur (Dr.-Ing.)

vorgelegt der Fakultät für Maschinenbau
der Technischen Universität Ilmenau

von Dipl.-Ing. Dzmitry Savitski

1. Gutachter: Univ.-Prof. Dr.-Ing. Klaus Augsburg
2. Gutachter: Prof. Dr. Alessandro Victorino
3. Gutachter: Dr.-Ing. Jan Sendler

Tag der Einreichung: 12.11.2018
Tag der wissenschaftlichen Aussprache: 16.09.2019

urn:nbn:de:gbv:ilm1-2019000424

Table of contents

List of figures

List of tables

Chapter 1

Introduction

1.1 Motivation

Vehicle automation, new safety regulations, environmental restrictions and customer demands are forming principally new requirements to vehicle brake system design and control. As a consequence, automotive companies are faced with a task of producing reliable brake system control and design, which simultaneously ensure better brake performance, lower emission level and ride quality. Due to this fact, brake system architecture is going towards full decoupling of brake pedal and actuators, which is known as the x-by-wire system design. This produces more flexibility in system control, guarantees quicker system response and extends operational frequency of the system.

Despite having various approaches in terms of hardware components design of decoupled brake systems, there is still a demand in control methodology, which can cover aforementioned system requirements and be applicable for various vehicle system types and vehicle automation levels. This leads to the need in extensive analysis of the brake system control methods guaranteeing robust system operation during all braking modes and providing necessary interfaces for future integration with other vehicle dynamics control systems.

In this sense, wheel slip control (WSC) and anti-lock braking system (ABS) remain a core active safety systems on the vehicle. In their basic functionality, they serve for maintaining maximal braking force, stability and steerability during emergency braking situations. Nowadays, WSC is used as the low-level controller in vehicle stability control (VSC), which is directly dependent on control precision and robustness of WSC. Emergency braking assist (EBA), which is a more recent technology, also uses ABS control at the low level when wheels are tending to lock during automated braking situations.

Aforementioned facts underline demand in development of the robust brake control system based on the brake-by-wire (BBW) system. In particular, it is necessary to understand

potentials of the existing BBW actuators in terms of control performance in WSC mode. Development of robust WSC algorithms presents the main contribution of this research to the topic of vehicle active safety and considers requirements to the brake control system for electric and automated vehicles.

1.2 Terminology

The terminology follows the ISO and SAE standards, whereas the divergent terminology is defined according to the relevant literature sources and represented below.

Chassis [1, 2] is the sum of all vehicle systems that are responsible not only for the generation of forces between the tires and the road surface, but also for the transfer of these forces to the road in order to enable driving, steering, and braking.

Active chassis systems [3] are related to all chassis control systems in the vehicle. They can be separated into categories according to their application, namely, vehicle dynamics control systems, vehicle comfort control systems and driver assistance systems.

Vehicle subsystem [4] is the physical device dedicated to realize various vehicle functions as steering, acceleration, braking etc.

Brake system [5] is the chassis subsystem responsible for decelerating the vehicle, holding the vehicle in stand still position, maintaining vehicle speed during downhill motion.

Anti-lock braking system (ABS) [6] is the braking-system closed-loop control devices which prevent wheel lock when braking and, as a result, retain the vehicle's steerability and stability.

Vehicle active safety [7] is the reserve in the longitudinal, lateral and vertical vehicle motion to the physical limits in actual driving situation. Active vehicle safety systems (e.g. ABS or ESC) are the control systems in the vehicle, which are responsible for avoiding road collisions involving ground vehicles.

Energy efficiency [8] is the use of less energy to produce the same amount of useful output. In presence of electric machines on the vehicle, energy efficiency can also mean

maximal recuperation of energy to produce the same amount of the braking torque.

Jerk [9] is the time rate of change of acceleration of the vehicle. This term is widely used for quantitative assessment of the ride quality [10].

Ride quality [11] characterizes the smoothness of the vehicle motion. Lower values of jerk correspond to better ride quality, while dynamic oscillations with high level of jerk negatively influence driver perception and lead to worse ride quality.

Root mean square deviation (RMSD) or *standard deviation* (STD) [12] is the square root of the mean of the squared deviation from the mean value of considered set of measurements. This metric is used for studying dispersion in statistics, but also found an application in control engineering for evaluation of the control quality.

Chapter 2

State of the Art

In its classical definition, brake system is responsible for decelerating the vehicle, holding the vehicle in stand still position and maintaining vehicle speed during downhill motion [5]. With the invention of new types of the braking and control systems, this should also provide maximally possible braking torque in emergency situations, maintain steerability and stability of the vehicle, be able to recuperate kinetic energy during the braking process and achieve minimal particle and noise emissions.

Evolution in brake system design has a tendency of fully decoupling the actuators and the brake pedal. In such configuration, brake actuators are directly controlled by the electronic control unit (ECU), while calculations of wheel torque demand are based on the information from a pedal travel sensor. Brake pedal feel is emulated by hydraulic or electromechanical simulator to provide necessary feedback force to the driver. Aforementioned system configuration represents so-known brake-by-wire (BBW) architecture, which nowadays finds more and more application on the vehicles [13–15]. Such system concept is realized by the use of several types of brake actuators: (i) electrohydraulic (EHB), (ii) electromechanical (EMB), (iii) magnetorheological (MRB), (iv) electric motors (EM) and (v) hybrid.

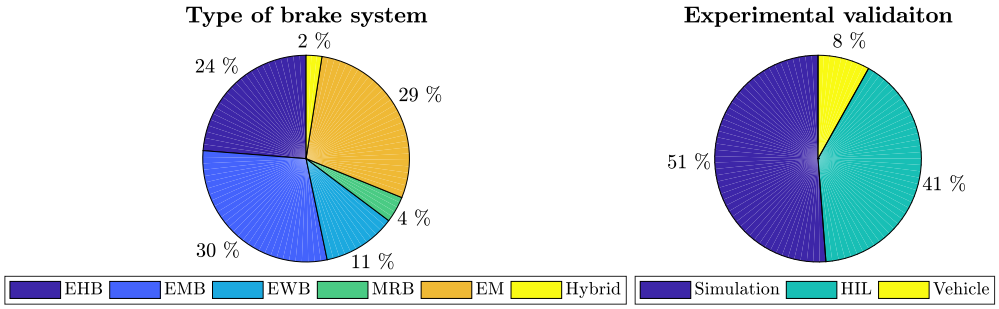

Fig. 2.1 Research and technical papers in area of brake system control and design: left - classification by system type (left) and by validation method (right)

To analyze gaps in the area of decoupled brake systems control, ScienceDirect, SAE, IEEE Xplore and Google Scholar technical literature sources were analyzed. As it can be seen in Figure 2.1, the most attention has been given to electromechanical (29%), regenerative (29%) and electro-hydraulic (24%) brakes. Such types of automotive brake systems have advantages due to their high dynamics and capabilities in energy recuperation, as in case of electric motors. Several promising solutions like magnetorheological brakes are still rarely explored in the literature (4%) due to existing issues with braking performance. Speaking about the vehicles without electric powertrain, hybrid brake systems have not received much attention (3%), despite the fact that they are capable of resolving issues with system redundancy in case of EMB systems.

Provided by decoupled brake system architecture, individual wheel torque control has principally new opportunities in vehicle dynamics control, driving comfort, energy efficiency and can be even used for purposes of ride comfort, see e.g. [16, 17]. However, even in the presence of decoupled brake systems implementations on serial vehicles, corresponding control algorithms are very rarely tested on the vehicles (8%), see Figure2.1. Mostly they are validated in simulation (51%) or (41%) tested on the hardware-in-the-loop (HIL) test rigs.

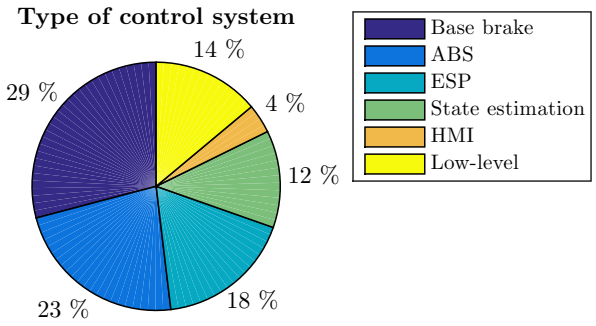

Fig. 2.2 Research and technical papers in area of brake system control

As it is shown in Figure 2.2, base-brake control functions (19%), anti-lock braking (15%) and vehicle stability control (11%) are mostly discussed in published research and technical papers. Despite this fact, new potentials of the decoupled brake systems are usually not analyzed even in case of ABS control functions.

Aforementioned facts motivated the author to analyze state of the art solutions in the area of decoupled brake system design and control. Next subsection presents an overview of existing hardware solutions comparing design solutions by following aspects: (i) braking performance, (ii) energy consumption, actuator dynamics, (iii) fault-tolerance, (iv) wear and (v) maintenance. Basing on this analysis, the most promising solutions are further selected for the experimental analysis and development of relevant control strategies.

2.1 Decoupled brake system design

Nowadays, one of the most popular solutions for BBW systems is the implementation of the electromechanical brakes. The idea of electromechanically actuated brakes was firstly registered in patent [18] in year 1899. Such brakes have several benefits, which were explored and validated in [19] using experimental prototypes. Compared to conventional hydraulic systems, EMB provides several advantages, such as individual wheel torque control, more compact design, adjustable brake pedal feel, realization of ABS functions without necessary implementation of additional components like hydraulic control unit (HCU), direct and continuous control of clamping force, easy maintenance and environment friendliness. All these factors present EMB a very attractive solution for the BBW design and significantly reduce system's production and assembly time. Despite aforementioned advantages and improvements compared to conventional hydraulic systems, several challenges in design and implementation of EMB still exist. Electric motor installed in brake caliper makes possible installation of the system only on the cars with relatively large wheel space like on SUVs [20]. Another drawback is the high energy consumption, as EMB actuators without self-energizing mechanism need high power to produce clamping force. This leads to the use of higher voltage power supply and additional electrical systems. EMB still have not found application on the vehicles without the support of hydraulic systems also due to issues with system redundancy. If electric and/or electronic system fails there is no physical coupling between the brake pedal and brake actuators and backup solution in this case is included. Duplication of actuators and power supply can solve this issue, but leads to significant increase of system costs.

To resolve the problem of high energy consumption of EMB, the wedge mechanism for mechanical self-reinforcement was proposed in electronic wedge brakes. Considering various types of EWB systems, authors in [21] classified EWB into lower-wedge and upper-wedge principles. Many efforts in development of such system were done by Siemens, which developed several modifications and concepts of this brakes type. First prototype with two electric motors and self-reinforcement mechanism was introduced in [22]. As an advantage over known EMB solutions, this significantly reduced energy consumption and allowed the use of 12V vehicle power supply. Having quick dynamics, this actuator also showed benefits in ABS braking mode. In particular, paper [22] demonstrates that force acting on the wheel can be reduced by 10% in approximately 10 ms, which provides agile wheel slip control. Several modifications of these brakes were proposed later and brake mechanism with single motor (instead of two as in [22]) was introduced in [23]. In the same time, MANDO offered EWB with 'Cross Wedge Mechanism' [24]. As an advantage this mechanism provides uniform distribution of braking force and even pad wear, as a consequence. Improvement in

efficiency of braking force generation was achieved by the use of double-wedge mechanism, as shown in paper [25]. Despite attractive functions of EWB, this system has issues with redundancy as in EMB case.

Another perspective solution in the area of decoupled brake systems is presented by magnetorheological brakes. General principle of MRB was patented in 1998 by Lord Corporation [26]. MRB includes magnetorheological fluid which solidifies under application of magnetic field. This phenomenon is based on presence of disperse micron-sized suspensions in magnetorheological fluid. Compared to the friction brakes, MRB resolves such issues as brake pad and disc/drum wear, degradation of braking performance due to the overheating of friction pair and residual torque. Moreover, this system can be used with 12V electrical systems. Design of the MRB for automotive applications was proposed in several publications [27, 28]. This system can be classified into two types depending on the type of rotor used: disc or drum. Developed for automotive applications, MRB prototype was experimentally validated on the test rig in [27]. This research indicates that the required torque for braking a car cannot be achieved with this configuration. In [28] optimization-based solution for disc-type MRB was proposed resolving a trade-off between the brakes size and maximal braking torque. As an advantage this design of MRB has higher brake torque by using the proposed magnetic circuit compared to [27]. Some other challenges in MRB design are indicated in [29] and showing demand in additional research in heat dissipation of MRB and reduction of its weight .

Introduced by the Robert Bosch GmbH in 1996 [30], decoupled electro-hydraulic brake system had principally new architecture compared to the conventional electro-hydraulic brake systems of that time. This has more sophisticated design of the HCU, which includes high-pressure accumulator (HPA), brake pedal simulator (BPS) and additional sensors for observing pressure in brake calipers, HPA and BPS. Presence of higher number of pressure sections in HCU makes necessary installation of additional hydraulic valves for pressure control purposes. As soon as such HCU has complete decoupling from brake pedal, control unit of the brake system has its own low-level pressure control logic and can overtake main brake functions in case of VCU failure. Briefly describing control principles of such DEHB system, pressure is delivered to accumulator by the hydraulic pump to provide high preload pressure (around 180 bar). Information about driver intention is based on measurements of brake pedal travel sensor, which are later post-processed in VCU. Obtaining calculated brake pressure demand from VCU, internal low-level control logic is used to maintain corresponding pressure levels by actuating hydraulic valves in HCU. In the same time, feedback pedal force is produced by BPS which is installed in master cylinder and connected with corresponding hydraulic section in HCU. Conventional hydraulic coupling remains

for front wheels as backup solution. Fulfilling safety requirements and providing better performance than EHB, this system came in serial production in 2001 [31], when Daimler used Sensotronic Brake Control (SBC) on their passenger vehicles [13, 14]. Despite these advantages, bulky design of this systems led to significant increase of the brake system production costs. To solve this issue, more compact DEHB solutions have integrated brake system architecture and use high-performance pressure pump instead of HPA. They are expected to enter automotive market in 2018 and going to be used also in partially automated vehicles [32]. Despite DEHB system's narrower bandwidth and slower response than EMB or EWB, this can perform functions where high-performance brake actuators are required [33] or ensure accurate control of wheel slip control in ABS mode [34].

Requirements in better energy efficiency and environment friendliness, motivated automotive engineers to use electric motors as brake system actuator. The idea of the electric powertrain is not new and the first car propelled by electric motors is presumably was developed by Andreas Flocken [35]. After just over a century this powertrain architecture has become one of key solutions in developing so-known 'green' vehicle concept with significantly reduced emissions level and energy consumption compared to the vehicles with ICE and friction brakes. Besides the traction mode, electric motors are capable of generating braking torque, regenerating energy and providing higher actuator dynamics compared to conventional EHB systems. Nowadays, several configurations of the powertrain systems are known. They able to propel and brake a vehicle with the help of (i) central electric motor, (ii) on-board (OBM) and (iii) in-wheel individual electric motors (IWM). The latter two configurations have the highest potentials not only in improvement of the vehicle energy efficiency, but also in enhancing braking performance. In our days, electric powertrain has found wide application in serial vehicles with hybrid or fully electric powertrain and in motorsport [36]. Nevertheless, this system cannot be used alone without backup or supporting brake system due to limited peak torque in braking mode and fail-safe reasons. These issues were resolved by integration of electric powertrain with friction brake systems.

As it was mentioned before, one of the drawbacks of EMB and electric motors is the absence of backup actuators, which provide physical coupling between brake pedal and calipers in case of electric and/or electronic system failure. For this purpose, alternative solution were proposed and combine, for example, EHB and EMB in scope of one system [37]. The main idea of such configuration is to use the advantages of EMB, which have higher system performance, minimized residual torque and fulfill safety requirements by using hydraulic system. Such architecture can have various layouts and combination of brake actuators, for example, producing brake force by hydraulic system on the front wheels and by EMB or EMs on the rear. It means that in case of system failure, front brakes will be

capable of providing required braking force through direct hydraulic coupling. Some of the hybrid brake systems include EMB and hydraulic piston in one caliper to provide necessary system redundancy. However, they lead to higher system costs, more sophisticated caliper design and difficulties in maintenance.

Analyzing each type of decoupled brake system and taking into account aforementioned advantages and drawbacks of each brake system type, following conclusions can be done about considered decoupled brake system types:

- DEHB system can be used in the vehicle without any supporting or backup systems;
- Electric motors are widely used in the vehicles for traction and braking modes, but cannot fully cover the demanded brake torque and used only in combination with EHB systems;
- EMB still have issues with high energy consumption and need redundant ECU, power supply and, eventually, electrohydraulic brake actuators;
- EWB has advantages over EBM in in terms of energy efficiency consumption but suffering from the issues with high brakes wear;
- MRB provides significant advantages over known EHB and EMB systems and represent a very promising solution; however, this system has not found application in automotive industry due to strong limitations in maximal braking torque.

From these conclusions and performed literature analysis, it can be seen that DEHB system is irreplaceable component of the vehicle even in configurations, where other brake actuators are used. Despite this fact, utilization of OBM and IWM can potentially provide benefits in WSC compared to DEHB. Therefore, DEHB, OBM and IWM brake systems are further considered for brake control system design and experimental studies. Next subsection presents state of the art solutions in the area of ABS control, analyzing its possible enhancements by the use of selected brake actuators and advanced control approaches.

2.2 Anti-lock braking system

During emergency braking situations or braking in severe road conditions, ABS should support the driver by modulating brake pressure in calipers, which allows avoiding wheel lock and degradation of longitudinal and lateral forces, as a consequence. First ABS type with mechanical actuation principle was introduced by Gabriel Viosin in 1929. Development of ABS was initiated in aviation engineering and the system was aimed at avoiding tire

blow-out and spin-outs on icy runways during flight landing. In particular, this system was used in Boeing B-47 bombers. In 1958 ABS was firstly used in motorcycles to safe the driver from falling during braking on wet road surfaces. Already from 1978, ABS produced by Robert Bosch GmbH was widely used in automotive area. Due to significant advancements in vehicle active safety and road safety in general, nowadays, it is mandatory to equip newly produced passenger cars with the ABS systems.

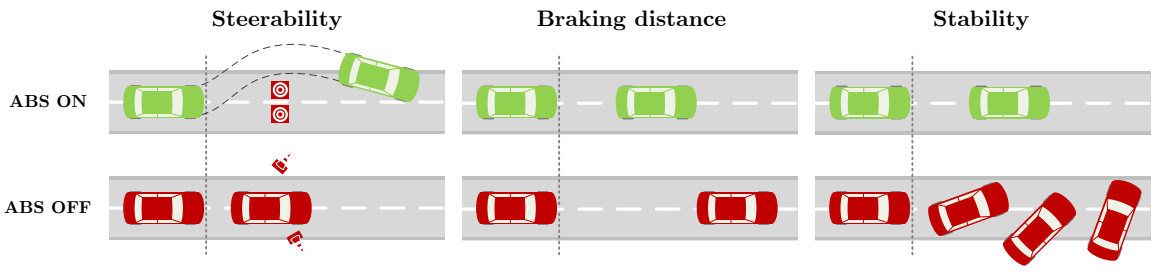

Fig. 2.3 Three main functions of ABS system: maintaining steerability, maximal braking force and vehicle stability

In general, ABS covers three main tasks: (i) realization of maximally possible braking force in current road conditions, (ii) maintaining steerability and (iii) directional stability of the vehicle. These three cases are schematically presented in Figure 2.3. Besides these core functions, ABS should also (a) use low braking torque amplitudes reducing longitudinal force oscillations (b) utilize minimal number of sensors and (c) rapidly adjust to changing road conditions [38].

Main physical phenomena causing longer braking distance is the non-linear relation of the braking force and longitudinal wheel slip, see Figure 2.4. After reaching the peak force value, degradation of braking force occurs with increasing wheel slip ratio. Therefore, task of ABS in terms of braking performance is to keep wheel slip ratio in emergency brake situations so close to the extremum point as possible.Vehicle can also lose stability and steerability due to the similar tendency in lateral force generation, as shown in Figure 2.4. As it can be seen, lateral force significantly decreases at higher values of the wheel slip. Thus, lateral force cannot be maintained for steering a vehicle if wheels are tending or close to the lock situation. Such dangerous situation can be mitigated by holding wheel slip in appropriate area by means of ABS.

Considering conventional EHB system with rule-based algorithm, ABS control is done through actuation of corresponding valves in hydraulic control unit (HCU). Typical HCU of conventional type consists of the following components: inlet and outlet valves, pressure accumulator, hydraulic pump, return pump and pulsation damper. During the service braking, outlet valve is closed and inlet valve is opened to deliver maintained pressure from the master

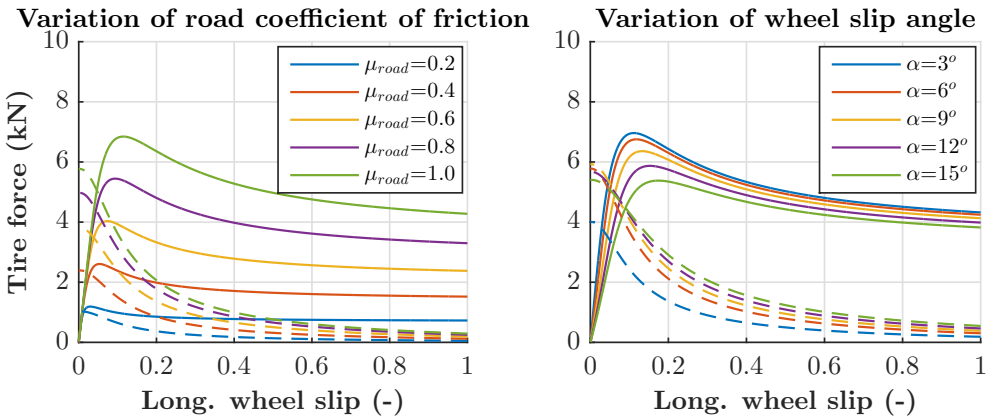

Fig. 2.4 Absolute value of longitudinal (solid line) and lateral (dashed line) force variation in relation to road coefficient of friction and wheel slip angle

cylinder directly to the brake calipers. In case of wheel spin-out, system applies following control phases to avoid loss of braking and steering force: increase, hold and release pressure. ABS is usually based on three possible control principles: wheel slip, wheel deceleration and combined control. There are also some alternative methods, which use direct measurements of the braking force, but they are not commonly used due to the cost of measuring devices [39]. Nowadays, direct wheel slip control is most commonly used in the industry [40]. It is aimed at keeping wheel slip at optimal value in emergency braking cases. Thus, vehicle can realize maximal braking force and maintain vehicle steerability, as a consequence.

2.2.1 Wheel slip control

WSC function belongs to several classes of vehicle active safety algorithms such as ABS, traction control and vehicle stability control (VSC) systems. In the most cases, industrial solutions for WSC in the passenger cars use rule-based braking torque modulation through hydraulic brake actuators. Such approach has sufficient functionality for conventional vehicles to fulfill safety requirements in vehicle active safety. Nevertheless, recent trends in vehicle electrification and automation rise a question about revisiting WSC design that can be argued as follows.

As for electric vehicles, wheel slip control functions can be efficiently realized with individual in-wheel or on-board motors [41, 42]. Recent studies show that electric motors not only allow better tracking of the reference wheel slip, but also provide robust operation in such safety-critical driving situations as driving on split-road surface [43]. However, strict legislative regulations and functional limitations for mass-production vehicles still require blended operation of electric motors and traditional brake systems. WSC in the braking mode

should be realized in this regard with the brake blending with electric motors and friction brakes as actuators.

Another problem of the wheel slip control is recently emerged with the development of automated driving technologies [44, 45]. Coming generations of autonomous vehicles, especially on automation level 4 to 5 in accordance to SAE J3016 standard, should provide better ride quality considering limited awareness of the driver/passenger about an actual driving situation. In particular cases of braking in ABS mode, it means that the deterioration of ride quality caused by undesired oscillations in longitudinal vehicle motion has to be minimized. However, it is very difficult to achieve this target by the conventional rule-based WSC with switching control logic and conventional EHB systems. Such requirements in the area of WSC put demand on the development of appropriate control methods, which are robust to road conditions variation and applicable to the decoupled brake systems. However, nowadays there are no well-established control approaches in this area.

WSC system typically consists of two main components: the slip controller and the reference wheel slip generator. The first part concerns the choice of appropriate controller architecture and control method, while the latter is more related to the state estimation problem. Most of known studies in WSC propose switching control logic methods, which are also traditionally used in industrial ABS. For example, paper [46] demonstrates a solution based on nonlinear state feedback, which guarantees robust system operation. In [47] the control is realized with the fuzzy logic with reference slip estimation through artificial neural network. In general, the switching control logic for WSC predominantly uses the rule-based algorithms, where the control process consists of cyclic alternation of phases for the increase, decrease and holding of the wheel torque depending on selected control thresholds by the wheel slip and acceleration. During several decades there were no alternatives to such an approach due to a limited bandwidth and time response of traditional hydraulic systems. However, from the beginning of 2000s, decoupled brake systems made the implementation of continuous WSC algorithms possible with positive impact on vehicle safety and ride quality.

Continuous WSC system can be potentially realized with many approaches, starting from well-known PID algorithms up to complex hybrid control methods. Considering typical WSC requirements in terms of real-time applicability and robustness to maneuver-/road-related uncertainties, it is difficult to select a priori more suitable control technique. Among possible approaches for continuous WSC, sliding mode (SM) control can be considered as a candidate for robust WSC. One of the first SM solutions for WSC was proposed in [48] including extremum seeking algorithm. In [49] the second-order sliding mode (SOSM) control is utilized together with the estimation of tire-road friction based on the first-order sliding mode observer. Integral-type SM control with state-dependent Riccatti equation as nominal

controller is discussed in [50]. This method takes into account WSC robustness and actuator faults. The study [51] used SM control with conditional integrator to suppress chattering effect. Attenuation of chattering caused by the SM control was also addressed in [52] through offline optimization of controller gains. In [53] several SM control sliding surfaces for WSC in two-wheeled vehicle were analyzed in terms of robustness to uncertainties related to the tire-road interaction. Handling of such uncertainties is also addressed in [54], where Grey system modeling approach was applied to SMC. This approach achieved sufficient reduction of wheel slip oscillations even in cases of significant road friction variation. However, most of the research studies on SM control in WSC area are limited by the lack of experimental validation and, in majority of cases, the reference wheel slip is considered as a constant value.

2.2.2 Reference wheel slip adaptation

Independently from the selected control strategy, WSC should provide reliable generation of the reference wheel slip and its adaption to driving conditions. However, only few published studies are known in this area. Authors of paper [55] have proposed reference slip estimation using the bootstrap Rao-Blackwellized particle filter based on the signals from the wheel speed sensors, accelerometer and GPS. Estimation of the reference slip is also discussed and validated in simulation in [56], where wheel slip dynamics is handled as the second-order system based on LuGre friction model. Feedback linearizing control is given in [57], where the optimal wheel slip area is determined by the extremum seeking algorithm based on the online optimization method, where the uncertain plant with unknown parameters is considered. However, as it can be concluded from the aforementioned published research studies, robust and real-time capable methods of the reference wheel slip estimation are mainly based on the polynomial fitting algorithms. As it was demonstrated in [58],[59],[60], this method allows the determination of extremum position using conventional on-board vehicle sensors. However, there is limited information on relevant publications about the integration of the slip target adaptation mechanisms into the overall control architecture.

2.3 Research demand and thesis outline

Provided technical literature survey shows that the application of novel brake systems is inevitable in the presence of new requirements to system dynamics, reliability and environment friendliness. Due to this fact, decoupled brake system architecture appears to be the most suitable solution for electric and automated vehicles. Among several types of such systems, DEHB, OBM and IWM actuators were selected and considered in this study. Being a key

part of vehicle active safety systems, wheel slip control should be designed for these types of brake systems and consider requirements in robustness, braking performance and ride quality.

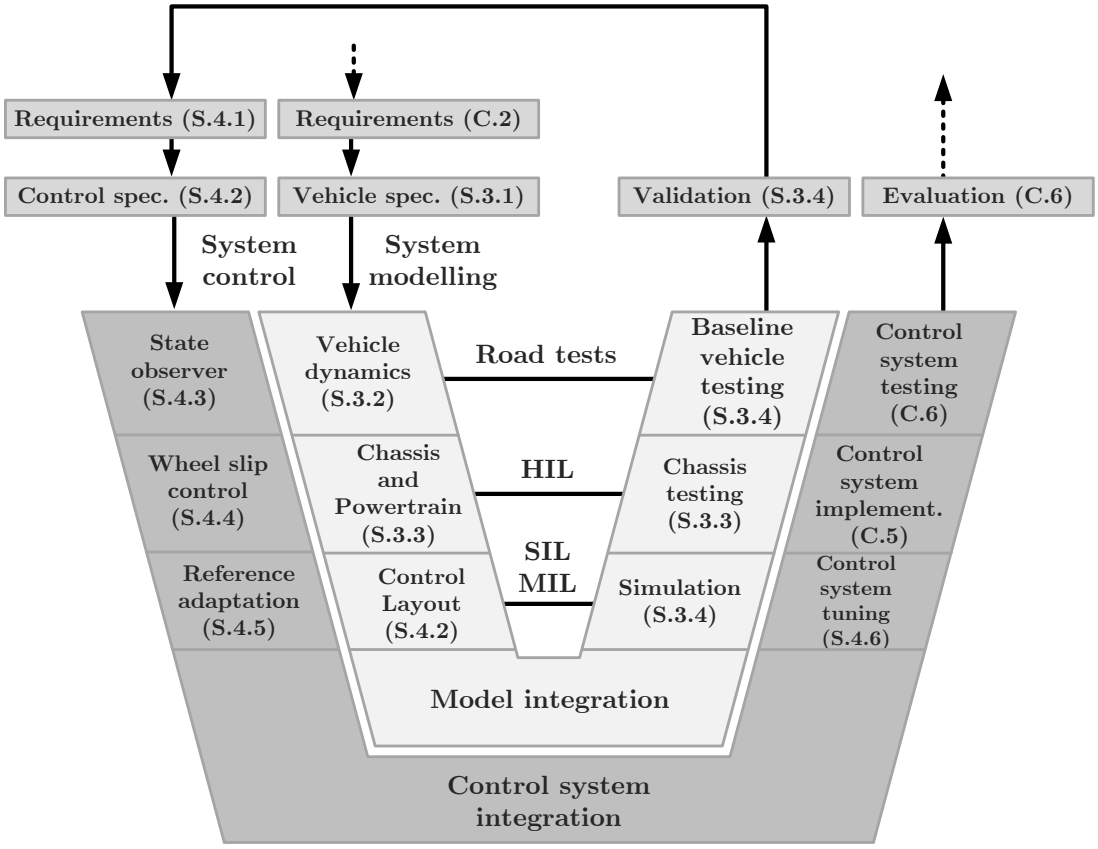

Fig. 2.5 Development flowchart presented as V-model

Considering these remarks and presented literature survey in the areas of decoupled brake system design and ABS control, this thesis is aimed at solving the following tasks:

- Development of robust continuous WSC control, which can handle such uncertainties as road friction variation and vertical load distribution;
- Establishing reference wheel slip adaptation logic, which can provide information about optimal wheel slip value;
- Development of vehicle state estimator based on the measurements with standard on-board vehicle sensors;

- Development of brake blending control strategy, which is aimed at maximal use of electric motors in WSC mode;
- Investigation of continuous WSC functionality in terms of safety, ride quality, control performance, robustness for the DEHB, OBM and IWM brake systems;
- Performing experimental analysis of developed continuous WSC approaches in simulation, hardware-in-the-loop and vehicle road tests.

To cover these tasks, development process of control algorithms is presented as the V-model in Figure 2.5, where each development step has a reference to the corresponding sections in the thesis. In Section 3.1 vehicle type is defined considering customer demands and situation on the passenger vehicles market. Mathematical description of the vehicle motion is given in Section 3.2 to obtain state equations for further development of state observer. Simulation models of chassis and powertrain system is presented in Section 3.3. Vehicle dynamics and subsystems models are validated separately and in scope of MIL/SIL simulations for selecting appropriate simulation environment. Section 3.4 provides comparison with experimental results obtained during preliminary vehicle tests. After summarizing the outcomes of Chapter 3, Section 4.1 presents control objectives and proposes numerical criteria for the evaluation of the developed control algorithms. Section 4.2 proposes overall architecture of the brake system control, which includes main base brake and WSC functions. Theoretical background of vehicle state estimator and brake system controller are given in Section 4.3 and in Sections 4.4,4.5 respectively. Evaluation of the developed algorithms in simulations are performed in Section 5.2, while hardware-in-the-loop tests are performed in Chapter 5. Experimental results, obtained for three vehicle demonstrators, are presented and analyzed in Chapter 6.

Chapter 3

Definition of the vehicle architecture, modeling and experimental validation

3.1 Overall vehicle specifications

Official EU regulations distinguish nine types of passenger vehicles [61]. Among them category J is the relatively younger class of vehicles, which includes sport utility vehicles (SUV) designed both on- and off-road driving conditions. Nowadays, total worldwide share of the small and large SUVs within total fleet of passenger cars is represented by 29 % and 13 % respectively [62]. However, not enough attention has been paid to SUVs previously, as this number was almost six times less fifteen years ago [63]. Active growth of SUV popularity started only two decades ago, as SUVs reached 19 % of the total passenger vehicles sales in the USA market in 1999 [64]. As it is indicated in Figure 3.1, the number of registered SUV vehicle is daringly growing since that time. Compared to the year 2001, approximately 550 % SUVs came to the European market in 2016 which is the highest growth among other passenger vehicle types. Such customer demands forced original equipment manufacturers (OEM) to expand the range of proposed SUV models from 28 to 75 [65].

In terms of the vehicle safety, SUV has set of the constructive features, which require a special attention to vehicle dynamics control systems. In particular it is known that vehicle center of gravity is located relatively high (over 0.7 meters averagely) in the variant with conventional powertrain type. This leads to the several specific control issues related, for example, to the rollover prevention for vehicles of this type [66]. High vehicle mass makes SUVs dangerous in collisions. Therefore, this vehicle type requires robust vehicle dynamics control systems to prevent or to avoid such road situations [67].

Besides specific issues in terms of safety, SUVs have one of the highest fuel consumption

(13.4 liters per 100 km) by performing the standard New European Driving Cycle (NEDC) [68]. It means that installation of electric propulsion can bring significant effect in terms of overall pollution reduction. This also well correlates with the current customers demand in the market of electric vehicles, as the highest percent (50 %) of customers, who would buy EV in future, are the drivers of off-road vehicle represented in particular by SUVs [69].

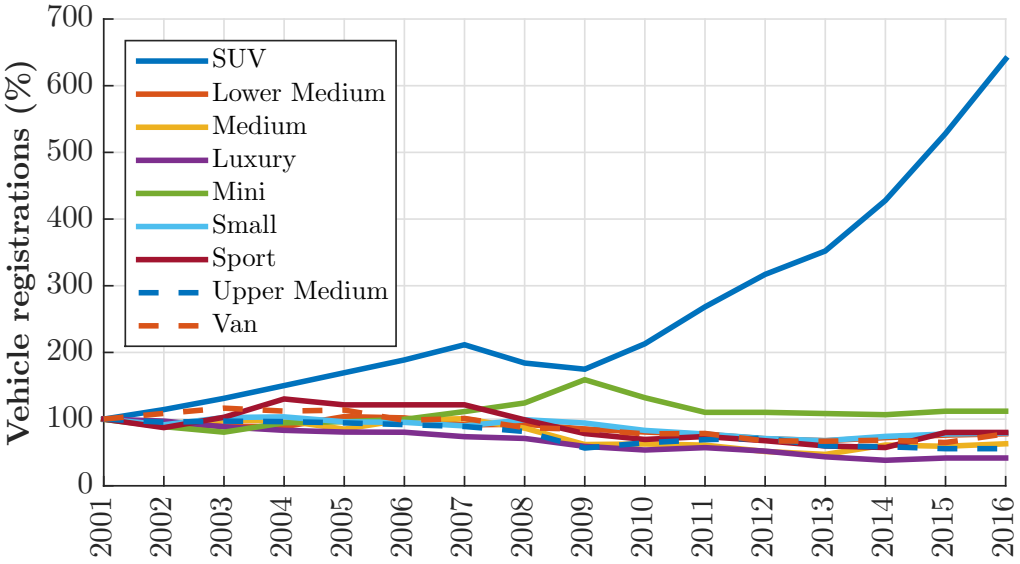

Fig. 3.1 Registrations by vehicle segment [70]

Aforementioned facts allow concluding that SUV as the passenger vehicle is still rarely explored vehicle type which requires special attention in terms of active safety and vehicle dynamics control. Further installation of electric powertrain, high-performance chassis and robust vehicle dynamics control systems can resolve the known traffic safety and environmental issues. These facts have motivated to select SUV as the vehicle prototype for the research in this work. In this thesis, SUV demonstrator with four-wheel electric motors and demonstrator with decoupled electro-hydraulic brake system are further analyzed and represent author's scientific and technical contribution to the European projects E-VECTOORC [71] and EVE [72], respectively. Additional investigation of the brake system control for individual in-wheel electric motors was performed in the framework of European project project CLOVER [73]. Theoretical background on system modeling, control and experimental validation involving three vehicle demonstrators are presented in the next sections.

3.2 Vehicle dynamics model

For the purposes of control design and validation of the developed control strategies in simulation, this section represents the mathematical description of the vehicle motion in three dimensional space. In presence of various approaches for modeling the vehicle motion, it is important to keep a balance between model fidelity and simplicity of the mathematical representation, as they hugely influence control quality of the model-based algorithms, computational load and real-time capability. The selected model consist of fourteen degrees of freedom (DoF), where six DoF are related to the longitudinal, lateral, vertical, pitch, yaw and roll motion of the vehicle body, whilst another eight DoF belong to vertical motion of unsprung masses and rotational motion of wheels, Figure 3.2. Such representation of the vehicle motion is accurate enough for the relevant control tasks that were confirmed in other research papers [74–76].

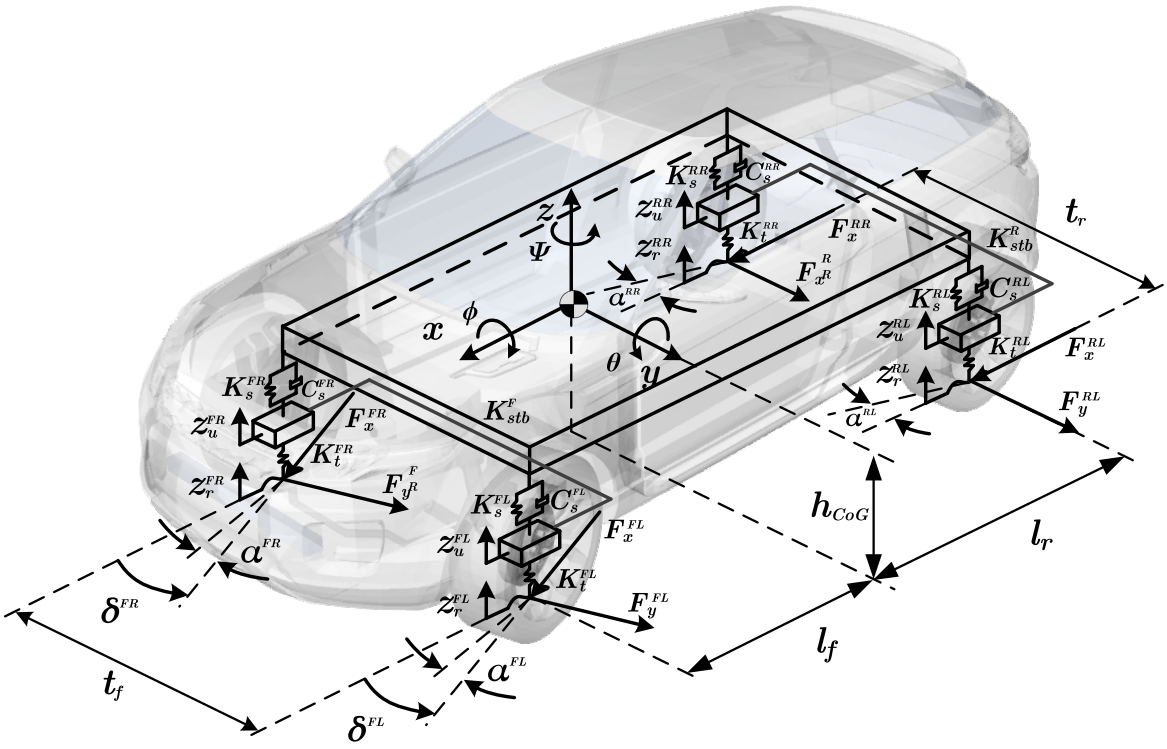

Fig. 3.2 Fourteen DoF vehicle dynamics model

By using Newtonian approach, the longitudinal, lateral and vertical motion of the vehicle can be expressed as

$$m_v \left(\frac{dV_x}{dt} - V_y \psi + \frac{dz}{dt} \frac{d\phi}{dt} \right) = \sum F_x \tag{3.1}$$

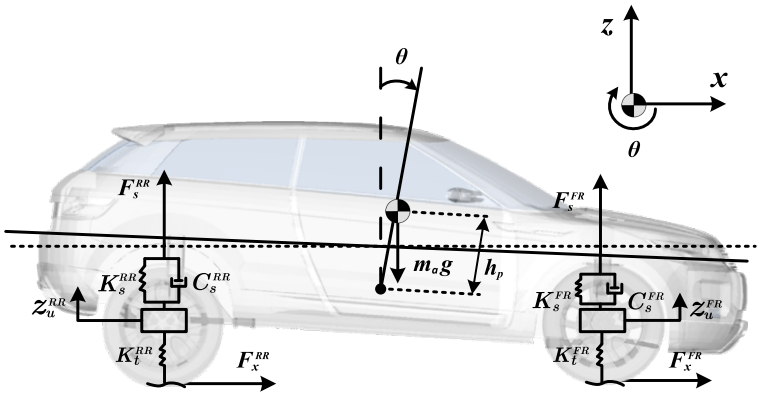

(a) Side view of the vehicle

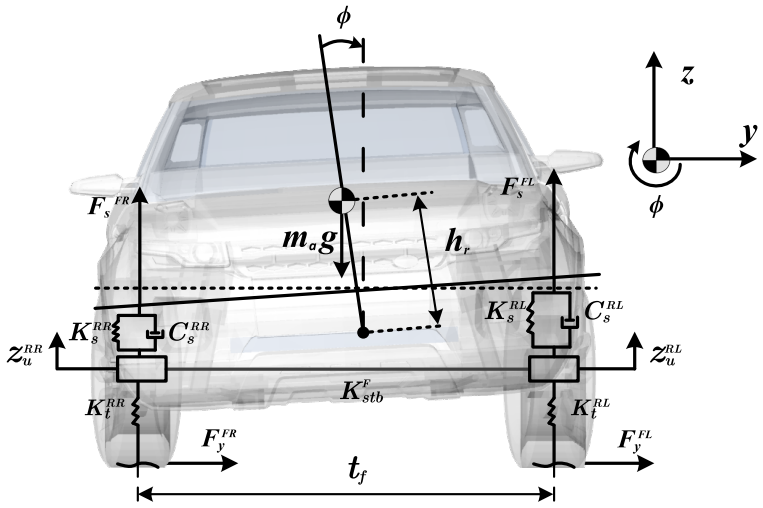

(b) Front view of the vehicle

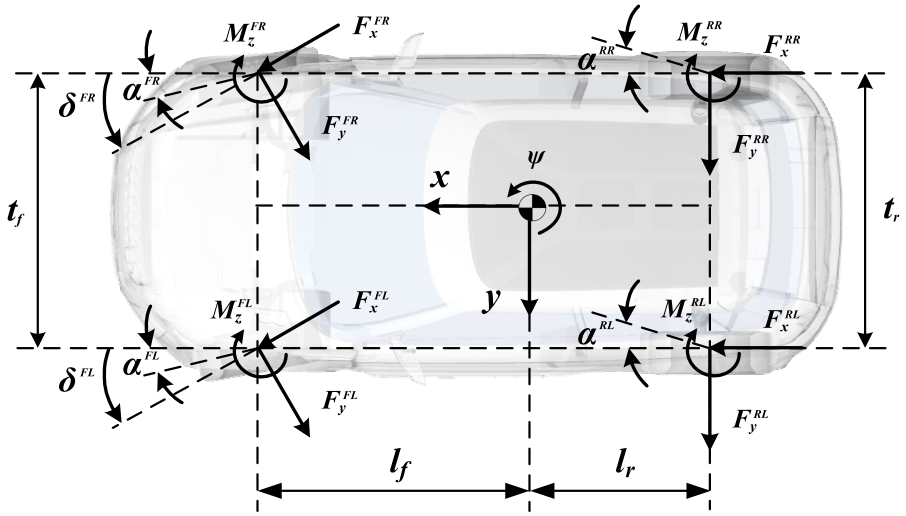

(c) Top view of the vehicle

Fig. 3.3 Vehicle scheme in three planes

$$m_v \left(\frac{dV_y}{dt} + V_x \dot{\psi} - \frac{dz}{dt}\frac{d\phi}{dt} \right) = \sum F_y \tag{3.2}$$

$$m_b \left(\frac{d^2 z}{dt^2} - V_x \frac{d\theta}{dt} + V_y \frac{d\phi}{dt} \right) = \sum F_z \tag{3.3}$$

where m_v is the total vehicle mass, m_b is the mass of the vehicle body.

The rotational roll, pitch and yaw motions of the vehicle (Figures 3.3a, 3.3b and 3.3c respectively) are expressed by the following set of equations:

$$I_{xx}\frac{d^2\phi}{dt^2} = \frac{t_f}{2}\left(F_s^{FL} - F_s^{FR}\right) + \frac{t_r}{2}\left(F_s^{RL} - F_s^{RR}\right) + m_b g h_r sin\phi + m_b a_y h_r cos\phi \tag{3.4}$$

$$I_{yy}\frac{d^2\theta}{dt^2} = -l_f\left(F_s^{FL} + F_s^{FR}\right) + l_r\left(F_s^{RL} + F_s^{RR}\right) + m_b g h_p sin\theta - m_b a_x h_p sin\theta \tag{3.5}$$

$$\begin{aligned} I_{zz}\frac{d^2\psi}{dt^2} &= l_f \sum_{j=R,L}\left(F_x^{Fj} sin\delta_{Fj} + F_y^{Fj} cos\delta_{Fj}\right) - l_r \sum_{j=R,L}\left(F_x^{Rj} sin\delta_{Rj} + F_y^{Rj} cos\delta_{Rj}\right) \\ &+ \sum_{i=F,R} t_{iR}\left(F_x^{iR} cos\delta_{iR} - F_y^{iR} sin\delta_{iR}\right) - \sum_{i=F,R} t_{iL}\left(F_x^{iL} cos\delta_{iL} - F_y^{iL} sin\delta_{iL}\right) - \sum M_z^{ij} \end{aligned} \tag{3.6}$$

where t_f and t_r is the front and rear wheel track, l_f and l_r is the position from the front and rear vehicle axles to the vehicle center of gravity, h_r and h_p is the position of the roll and pitch center, δ_{ij} is the road wheel angle. Indexes $i = F;R$ and $j = R;L$ denote the wheel position in the vehicle motion equations.

The total vehicle mass represents the sum of vehicle body (sprung) m_b and wheel corner (unsprung) m_u masses:

$$m_v = m_b + \sum_{i,j} m_u^{ij} \tag{3.7}$$

where m_u^{ij} is the unsprung mass of each corresponding wheel corner.

In Equations 3.1 and 3.2, total longitudinal and lateral forces are calculated as

$$\sum F_x = \sum_{i,j}\left(F_x^{ij} cos\delta_{ij} - F_y^{ij} sin\delta_{ij}\right) - F_x^{drag} \tag{3.8}$$

$$\sum F_y = \sum_{i,j} \left(F_x^{ij} sin\delta_{ij} + F_y^{ij} cos\delta_{ij} \right) - F_y^{drag} \tag{3.9}$$

where F_x^{drag} and F_y^{drag} are the aerodynamic drag forces in longitudinal and lateral directions respectively.

Remark. In the Equations 3.8, 3.9 and 3.6, wheel steering angles δ_{ri} equal to zero for the front steered vehicle.

The total vertical force F_z is equal to the sum of vertical forces produced by suspension:

$$\sum F_z = \sum_{i,j} F_s^{ij} \tag{3.10}$$

Neglecting suspension kinematics and considering equivalent simplified representation of the vehicle suspension with one DoF, suspension forces at the strut consider influence of the spring, damper and the stabilizer as follows

$$\sum F_s^{ij} = \underbrace{K_s^{ij} \left(z_u^{ij} - z_b^{ij} \right)}_{\text{spring}} + \underbrace{C_d^{ij} \left(\dot{z}_u^{ij} - \dot{z}_b^{ij} \right)}_{\text{damper}} + \underbrace{K_{stb}^{i} \left(z_b^{iL} - z_u^{iL} + z_b^{iR} - z_u^{iR} \right)}_{\text{anti-roll bar}} \tag{3.11}$$

where C_d is the damping of the shock absorber, K_{stb} is the stiffness of the anti-roll bar, K_s^{ij} is the stiffness of the suspension spring.

Considering relatively small values of the pitch θ and roll ϕ angles, the following approximation can be applied to derive vehicle body vertical motion at four positions:

$$\begin{cases} z_b^{FL} = z_b + \frac{t_f}{2}\phi - l_f\theta \\ z_b^{FR} = z_b - \frac{t_f}{2}\phi - l_f\theta \\ z_b^{RL} = z_b + \frac{t_r}{2}\phi + l_r\theta \\ z_b^{RR} = z_b - \frac{t_r}{2}\phi + l_r\theta \end{cases} \tag{3.12}$$

The vertical acceleration of the vehicle body is calculated considering suspension forces:

$$m_b \ddot{z}_b = \sum_{i,j} F_s^{ij} \tag{3.13}$$

The vertical motion of the unsprung masses:

$$m_u^{ij} \ddot{z}_u^{ij} = K_t^{ij} \left(z_r^{ij} - z_u^{ij} \right) - F_s^{ij} \pm F_z^{long} \pm F_z^{lat,ij} \tag{3.14}$$

where K_t is the tire stiffness.

During longitudinal and lateral vehicle motion, vertical tire forces are affected by the tire load distribution due to acceleration components. Neglecting suspension kinematics and compliance, nonlinear representation of the vertical tire forces with coupled pitch and roll dynamics are formulated as [77]

$$\begin{cases} F_z^{FL} = \frac{1}{2} m_v \left(\frac{l_r}{L} g - \frac{h_{CoG}}{L} a_x \right) - m_v \left(\frac{l_r}{L} g - \frac{h_{CoG}}{L} a_x \right) \frac{h_{CoG}}{t_f g} a_y \\ F_z^{FR} = \frac{1}{2} m_v \left(\frac{l_r}{L} g - \frac{h_{CoG}}{L} a_x \right) + m_v \left(\frac{l_r}{L} g - \frac{h_{CoG}}{L} a_x \right) \frac{h_{CoG}}{t_f g} a_y \\ F_z^{RL} = \frac{1}{2} m_v \left(\frac{l_f}{L} g - \frac{h_{CoG}}{L} a_x \right) - m_v \left(\frac{l_f}{L} g - \frac{h_{CoG}}{L} a_x \right) \frac{h_{CoG}}{t_r g} a_y \\ F_z^{RR} = \frac{1}{2} m_v \left(\frac{l_f}{L} g - \frac{h_{CoG}}{L} a_x \right) - m_v \left(\frac{l_f}{L} g - \frac{h_{CoG}}{L} a_x \right) \frac{h_{CoG}}{t_r g} a_y \end{cases} \tag{3.15}$$

To validate correctness and accuracy of the proposed mathematical formulations, road test results and simulations with commercial vehicle simulation software IPG CarMaker is presented in Section 3.4. Next section presents a detailed description of the used vehicle chassis and powertrain systems, proposes mathematical models for the simulation and provides the corresponding experimental validation.

3.3 Vehicle chassis and powertrain systems

3.3.1 Decoupled electro-hydraulic brake system

The selected DEHB uses Slip Control Boost (SCB) technology developed and provided by ZF TRW Automotive [78]. This system was developed to fulfill technical demands to the brake system on EVs and HEVs providing brake blending functions, pedal force feedback and fail-safe operation.

On the scheme in Figure 3.4, pedal travel sensors of the unit and the pressure sensor on the base-brake valve allow estimating the braking demand requested by a driver. This information is post-processed in the vehicle control unit (VCU) and the corresponding brake pressure demands are calculated. These values are further transmitted to the electro-hydraulic control unit (EHCU), where feedback pressure control is realized internally. It is based on the pressure measurements in the hydraulic circuits of the EHCU and indirect estimation of four brake caliper pressures $\hat{P}_{cal}^{ij}$. Availability of the pressure $\hat{P}_{cal}^{ij}$ allows more precise estimation of vehicle states, as reported in [79]. The force feedback to the brake pedal is performed through the pedal simulator generating appropriate pressure in the primary circuit

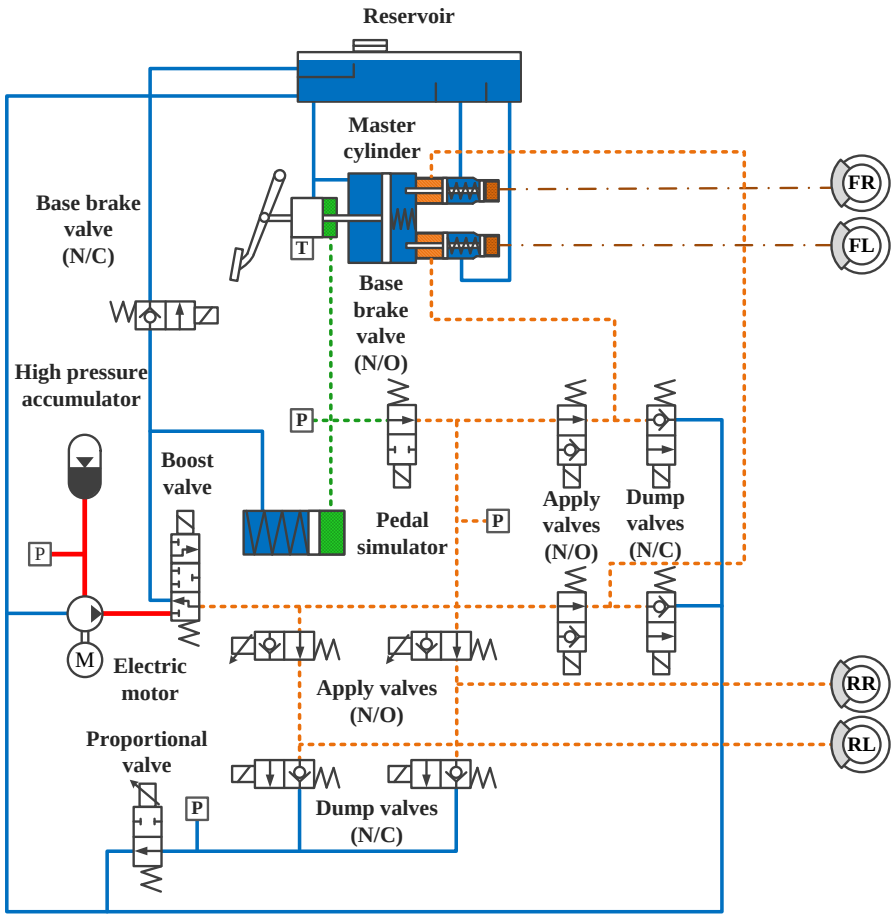

Fig. 3.4 Schematic representation of the decoupled EHB system

of the master cylinder. As a benefit, the presented DEHB design shows lower variation of the pedal force compared to conventional systems. Besides that, the system can maintain the desired brake pedal feel independently from the reference brake pressure that is important point for brake blending and automated braking functions. Such system architecture allows omitting the use of brake booster that is beneficial in terms of system's downsizing.

The base brake valves are activated during moderate braking. The boost valve proportionally controls the pressure from the high pressure accumulator (HPA). The brake pressure on wheel calipers is continuously modulated in accordance with the internal control logic of the EHCU. During the WSC mode, four apply valves are activated in the case of the excessive wheel slip in order to isolate the boost valve from the wheel calipers. Then both apply and dump valves are individually controlled and modulate the pressure for each wheel brake to reach desired wheel slip.

Table 3.1 Slip Control Boost Brake System

		Wheel position			
Test	Evaluation metric	FL	FR	RL	RR
Step response	Rise time (ms)	100	140	110	110
	Pressure RMSD (bar)	0.5	0.8	0.4	0.4
Slow ramp increase	Pressure RMSD (bar)	2.4	2.5	1.9	1.8
	Gradient STD (bar/s)	19.9	19.9	25.9	23.4
Slow ramp decrease	Pressure RMSD (bar)	1.9	1.9	1.1	1.1
	Gradient STD (bar/s)	19.5	19.8	25.9	25.9

Pressure in HPA is observed by the sensor to keep its level at 180 bar. Compared to the conventional brake systems, this allows quicker buildup of the caliper pressure providing 85-200 ms shorter rise time during the step pressure request. Besides that, utilization of the proportional valves instead of traditional relay valves allows precise pressure tracking during progressive pressure buildup or dump. Corresponding evaluation metrics of the introduced DEHB system are summarized in Table 3.1.

The model of the brake system dynamics should meet a compromise between fidelity and complexity representing main physical phenomena. For this purpose, authors in [80] propose a simple approach, where dynamics of the system is described by a second order transfer function (SOTF). In general, such approach describes the dynamics as a linear system and might be useful for designing linear control systems:

$$\frac{p_i}{p_i^*} = \frac{K_G \omega_n^2}{s^2 + 2\zeta\omega_n + \omega_n^2} e^{-\tau s} \tag{3.16}$$

However, such model formulation suffers from inaccuracies due to the following points:

- caliper pressure depends on the pressure in main hydraulic section and in accumulator, as consequence;
- dynamics of the hydraulic system has a hybrid nature, i.e. dynamics of pressure build-up and dump are asymmetric.

These items mean that describing brake system dynamics as SOTF requires additional scheduling of its parameters depending at least on absolute value of the caliper pressure demand as well as the separation between build-up and dump phases. Applicability of such

brake system model representation to brake system control task was confirmed by the author in research paper [33].

Physical model of the brake system requires knowledge of high amount of system parameters. Therefore, it is preferable to use simplified representations of the system dynamics where some of the parameters can be identified or selected empirically. Referring to the basics of hydraulics, the volume change in corresponding EHCU hydraulic sections are described as follows:

$$\dot{V}_{acc} = Q_{pump} - Q_m - Q_{sim} \tag{3.17}$$

$$\dot{V}_m = Q_{acc} - Q_m + Q_{sim} \tag{3.18}$$

$$\dot{V}_{ij} = Q_m - Q_{ij} \tag{3.19}$$

where Q_{pump}, Q_m, Q_{sim} and Q_{ij} are volumetric flow rate of the pump, main pressure circuit, pedal simulator and brake calipers respectively. Volumetric flow from the hydraulic pump can be experimentally determined by assessing pressure measurements at pressure accumulator and using relation between accumulator pressure and volume, which is later described by Equation 3.22.

Volumetric flow for the main pressure circuit and calipers is calculated as follows:

$$Q_m = C_f^m A_o^m \sqrt{\frac{2|p_{acc} - p_m|}{\rho_{bf}}} \operatorname{sign}(p_{acc} - p_m) \tag{3.20}$$

$$Q_{ij} = C_f^{ij} A_o^{ij} \sqrt{\frac{2|p_m - p_{ij}|}{\rho_{bf}}} \operatorname{sign}(p_m - p_{ij}) \tag{3.21}$$

where A_o is the orifice area, C_f is the flow coefficient.

Pressure value in accumulator is calculated considering adiabatic process neglecting thermal processes:

$$p_{acc} = p_{acc,0} \left(\frac{V_{gas,0}}{V_{acc}} \right)^{\kappa_{acc}} \tag{3.22}$$

where κ_{acc} determines the nonlinearity between pressure p_{acc} and V_{acc}.

Pressure in the main circuit and brake calipers considers calculations proposed in [81]:

$$p_m = p_{m,0} \left(\frac{V_{m,0}}{V_m} \right)^{\kappa_m} \tag{3.23}$$

$$p_{ij} = a^{ij}_{cal,1} V^3_{ij} + a^{ij}_{cal,2} V^2_{ij} + a^{ij}_{cal,3} V^3_{ij} \tag{3.24}$$

Coefficients $a_{cal,1}$, $a_{cal,2}$ and $a_{cal,3}$ determine the relationship between caliper pressure P_{ij} and corresponding volume V_{ij}. Their values can be identified by using experimental data.

Remark. For the simulation purposes and validation, presented system model neglects the interaction of the main pressure section with the pedal simulator assuming compete decoupling of the brake pedal and EHCU.

For the evaluation of the of model accuracy, brake pressure step response was evaluated for the linear and nonlinear models and for real system installed on the hardware-in-the-loop test rig (see Section 5.1). Figure 3.5 shows that nonlinear model representation accurately reproduces system behavior on the pressure build-up, dump and hold phases. During pressure increase and hold phases, caliper pressure dynamics strongly depends on the pressure in the main EHCU section which is considered in the nonlinear model representation. This effect is not captured in the linear model which is characterized by a high overshoot at the pressure build-up phase. Further deviation of the linear model at the dump phase is conditioned by a symmetric brake pressure dynamics representation.

For the numerical assessment of the model accuracy, RMSD of the brake pressure is summarized in Table 3.2. This shows that even in presence of higher deviations with linear model, values of brake pressure RMSD are not higher than 8 %. Nonlinear model in the same time has a maximal deviation of 3 % compared to the measurements.

Table 3.2 Brake system model validation

State RMSD	Linear model	Nonlinear model
Brake pressure FL, (bar)	2.6	1.5
Brake pressure FR, (bar)	3.8	0.8
Brake pressure RL, (bar)	3.0	1.2
Brake pressure RR, (bar)	3.8	1.0

Brake pressure, created by EHCU in calipers, actuates the cylinder, which produces friction force between brake pad and brake disc, Figure 3.6. The clamp force in relation to the caliper pressure is further calculated as

$$F_{cl} = \begin{cases} (p_i - p_o)\,\eta_c \frac{\pi d^2_{cyl}}{4} & p_i > p_o \\ 0 & p_i \leq p_o \end{cases} \tag{3.25}$$

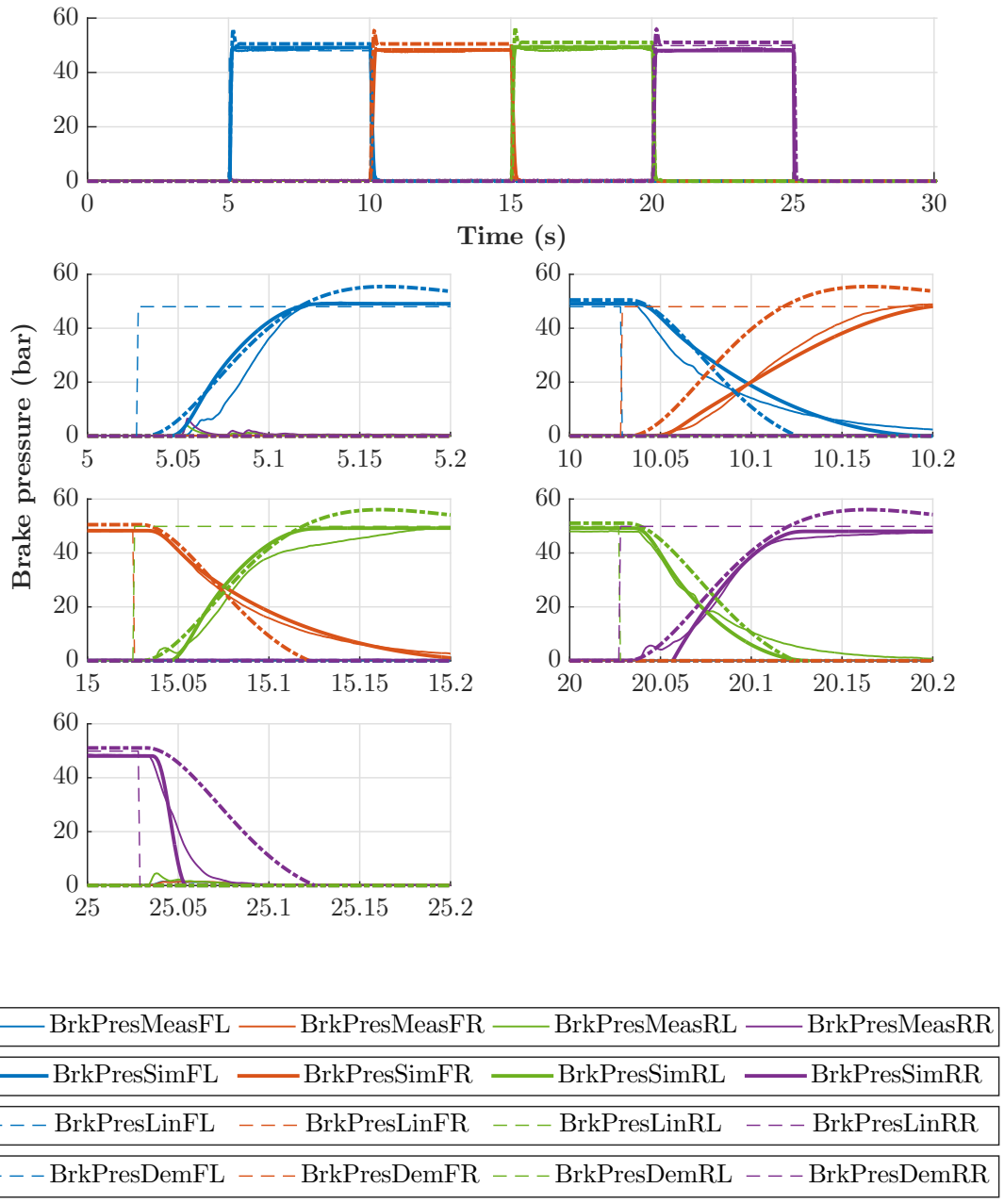

Fig. 3.5 Validation of the brake system model

where d_{cyl} is the diameter of brake piston, p_o is the pushout pressure, η_c is the wheel cylinder efficiency. Geometrical parameters of the brakes were obtained by measurements with the disassembled brake system.

Braking torque applied to the wheel is then calculated considering clamp force F_{cl}:

$$T_b = n_{bp}\mu_{br}F_{cl}r_d \tag{3.26}$$

where n_{bp} is the number of brake pads in contact with the brake disc, μ_{br} is the coefficient of friction between brake pad and rotor, r_d is the effective brake disc radius. In simulation studies, value of the coefficient of friction between brake pad and disc is assumed to be constant. In real driving conditions, this strongly depends on various brake system states such as rotor speed, temperature, humidity etc. Interested can refer to the author's research papers where this topic was investigated in relation to the brake system control [82, 83].

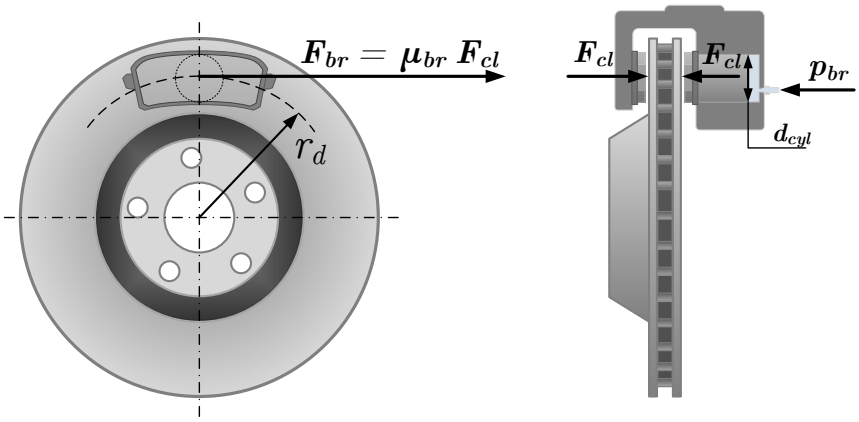

Fig. 3.6 Brakes scheme

3.3.2 Electric powertrain

In the SUV demonstrator with four individual electric motors, on-board architecture of the powertrain system was used. Such configuration implies connection of the electric motors with wheels trough gearbox and half-shafts, as shown in Figure 3.7. As an advantage in terms of the system design and packaging, on-board architecture allows keeping wheel hubs without significant modifications. However, half-shafts are present in such configuration and their dynamics can produce a negative influence on the vehicle drivability and braking comfort [84]. Speaking about braking mode, half-shaft oscillations can produce negative influence on the wheel slip control functions. Therefore, oscillations coming from the powertain

components should be suppressed by implementing additional control logic. In this section, mathematical representation of the drivetrain with on-board motors (OBM) is provided for SIL/MIL/HIL WSC performance assessment.

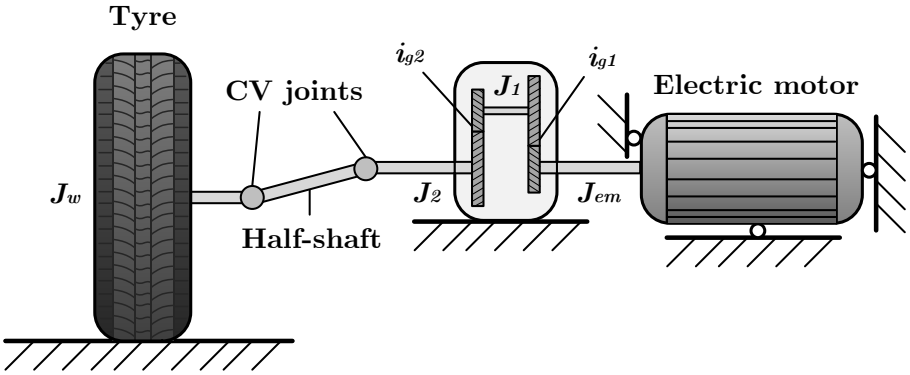

Fig. 3.7 Schematic representation of the powertain with on-board motor

Delays in the motor torque response T_{em} to the control request T_{em}^* is expressed as:

$$\tau_{em}\dot{T}_{em} + T_{em} = T_{em}^* \tag{3.27}$$

where T_{em} and T_{em}^{ref} are the actual and reference motor torque respectively, τ_{em} is the time response of the electric motor.

Neglecting rolling resistance and the aerodynamic drag force, dynamics of the powertrain from the motor shaft to the drivetrain output shaft can be expressed as:

$$T_{em} - T_{hs}\frac{i_g}{\eta_g} = \left((J_m + J_1) + \frac{(i_{g,1}i_{g,2})^2}{\eta_{g,1}\eta_{g,2}}\left(J_2 + \frac{1}{2}\frac{J_{hs}}{\eta_{cvj,1}}\right)\right)\ddot{\theta}_{em} \tag{3.28}$$

where T_{em} and T_{em}^{ref} are the actual and reference motor torque respectively, η_g and η_{cvj} is the gearbox and CV-joint efficiency respectively, τ_{em} is the time response of the electric motor.

The half-shaft torsional dynamics is represented as

$$T_{hs} = \beta_{hs}(i_{g,1}i_{g,2}\dot{\theta}_{em} - \dot{\theta}_w) + K_{hs}(i_{g,1}i_{g,2}\theta_{em} - \theta_w) \tag{3.29}$$

where θ_w is the wheel position, β_{hs} is the viscous friction in the shaft, K_{hs} is the shaft stiffness.

The torque delivered to the wheel through the powertrain is determined by

$$T_{hs} - \frac{T_w}{\eta_{cvj,2}} = \frac{J_{hs}}{2}\ddot{\theta}_w \tag{3.30}$$

Using aforementioned state equations and preliminary experimental data, obtained for the vehicle with for individual OBMs, validation of the powertrain mathematical model was performed. This includes two tip-in tests, where the vehicle drives in steady-state mode with constant velocity of 30 and 60 km/h and the desired torque demand is suddenly applied [85]. In this particular case, measurements of the wheel torque were performed by measuring hub at front right wheel for comparison with simulation results. Despite these tests were performed in traction mode, similar system behavior is typical also for the braking mode allowing objective assessment of the model fidelity.

Figure 3.8 compares longitudinal vehicle acceleration during the tip-in test and front right wheel torque for experimental and simulation results. As it can be seen, proposed simulation approach reproduces well wheel torque behavior having slight deviations in amplitude and neglectable phase shifts. Some higher deviations in vehicle acceleration are occurring due to the inaccuracies in the tire model for the traction mode, which was not explicitly investigated in the framework of the presented study.

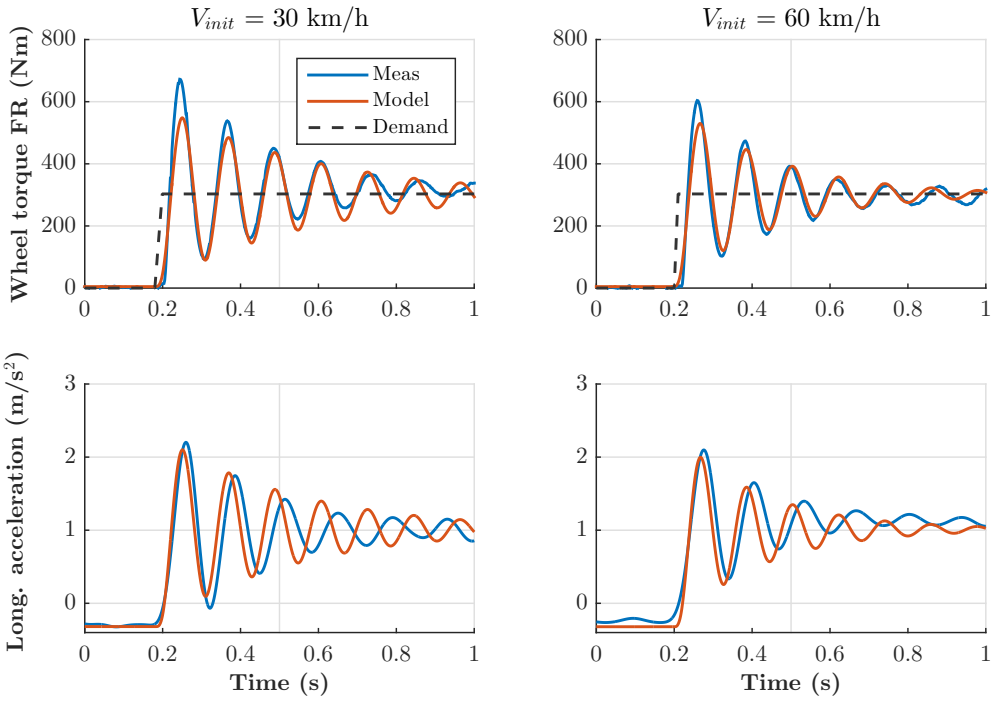

Fig. 3.8 Validation of the powertrain system

Quantitative assessment of the obtained results, summarized in Table 3.3, allows concluding that the represented model provides enough accurate description of the OBM powertrain since the deviation of the wheel torque does not exceed 10 % of the total torque demand at the front right wheel.

Table 3.3 Powertrain model validation

State RMSD	V_{init} = 30 km/h	V_{init} = 60 km/h
Vehicle acceleration, (m/s^2)	0.27	0.23
Wheel torque FR, (Nm)	32.6	26.4

3.3.3 Tire dynamics

Vehicle safety systems, such as ABS and ESP, are based on the WSC functions. Having dynamic torque application, control of the wheel slip is strongly dependent on the dynamics of tire. Therefore, realistic representation of the tire model shortens the difference between SIL/HIL and road tests allowing reduction of the controller tuning time.

Wheel motion for the case with application of braking torque T_b is described as

$$J_w \dot{\omega}_w = r_w F_x - T_b - F_{rr}, \tag{3.31}$$

where V_x is the wheel longitudinal velocity, ω_w is the angular wheel speed, m_s^{ij} is the mass of quarter vehicle, J_w is the wheel inertia, r_w is the effective wheel radius, T_b is the braking torque, F_x is the tire longitudinal force. Based on knowledge of input braking torque T_b^{ij} and calculation of longitudinal tire force F_x^{ij}, this equation provides information about wheel rotational speed ω_w^{ij} .

During a free roll of the wheel, rolling resistance forces are applied to the tire. According to the standard [86], tire rolling resistance force is determined as follows:

$$F_{rr} = p_t^{a_{r1}} F_z^{a_{r2}} \left(a_{r3} + a_{r4} V_{x,w} + a_{r5} V_{x,w}^2 \right), \tag{3.32}$$

where a_{r1} - a_{r5} are scaling parameters which determine the relationship between rolling resistance force and tire pressure p_t, vertical load and wheel longitudinal velocity $V_{x,w}$.

Translational wheel motion over the longitudinal and lateral axis in the coordinate system of the wheel is derived as

$$\begin{cases} V_{x,w}^{FL} = V_x + \dot{\psi}\frac{t_f}{2} \\ V_{x,w}^{FR} = V_x - \dot{\psi}\frac{t_f}{2} \\ V_{x,w}^{RL} = V_x + \dot{\psi}\frac{t_r}{2} \\ V_{x,w}^{RR} = V_x - \dot{\psi}\frac{t_r}{2} \end{cases} \tag{3.33}$$

$$\begin{cases} V_{y,w}^{FL} = V_y + \dot{\psi}l_f \\ V_{y,w}^{FR} = V_y + \dot{\psi}l_f \\ V_{y,w}^{RL} = V_y - \dot{\psi}l_r \\ V_{y,w}^{RR} = V_y - \dot{\psi}l_r \end{cases} \tag{3.34}$$

Translational velocities of the wheel center, obtained in Equations 3.33 and 3.34, are used for the calculation of the main kinematic parameters - wheel slip and wheel slip angle:

$$\lambda_{ij} = \frac{V_{w,x} - \omega r_w cos\alpha_w}{V_x} \tag{3.35}$$

$$\alpha_{ij} = \delta_{ij} - \arctan\left(\frac{V_{w,y}}{V_{w,x}}\right) \tag{3.36}$$

where $V_{w,x}$ is the speed of the center of the wheel, α is the wheel slip angle.

Considering relatively small values of the wheel slip angle α_w, Equation 3.37 can be simplified to

$$\lambda = \frac{V_{w,x} - \omega r_w}{V_{w,x}} \tag{3.37}$$

These two kinematic parameters are further used to calculate longitudinal and lateral wheel forces. Among various tire models, Magic Formula (MF) found a wide application in vehicle simulation environment used in industry as well as in academic research papers. This provides sufficient representation of the tire force generation in steady-state mode and includes can handle the cases where combined wheel slip occurs. In the framework of this research, MF tire was used for description of tire quasi-static behavior, which was parametrized by the Automotive Engineering Group at Technische Universität Ilmenau using local and external testing facilities [87, 88].

In reality, lateral and longitudinal tire forces are not developed instantly after the torque application. The delay of the tire force generation is linked to the distance traveled by the tire during torque application [89]. The delay in tire force generation has a first order dynamics which was confirmed experimentally in [90]. The distance traveled by the tire and required

for establishing tire force is called relaxation length. Among existing modeling approaches of tire longitudinal and lateral dynamics, application of the first-order transfer function to the generated tire force was used. According to theoretical and experimental analysis in [90], this approach produces results comparable with the testing data, but cannot handle low-speed modes. However, ABS is usually deactivated at relatively low velocities due to the nature of wheel dynamics and low-speed modes are out of interest for the ABS design. Therefore, the longitudinal and lateral tire dynamics having first order dynamics can be expressed in the following form [91]:

$$\dot{F}_x = \frac{V_x, w}{\sigma_x}\left(-F_x + F_x^*\right) \tag{3.38}$$

$$\dot{F}_y = \frac{V_y, w}{\sigma_y}\left(-F_y + F_y^*\right) \tag{3.39}$$

where F^* is the steady-state tire force, σ is the relaxation length.

In general representation, relaxation length is assumed to have a constant value. However, it was experimentally confirmed in [92] that relaxation length has no evident conjunction with the actuation frequency, but strongly depends on wheel slip, vertical tire load and its variation. To consider nonlinear relationship of the relaxation length on these system states, following extension of the transient tire model was introduced in [92]:

$$\sigma_x\left(F_z, \lambda\right) = \left[\sigma_{x,F_z} - \left(a_{\sigma 1} + a_{\sigma 2} dF_z\right)\right] \exp[-\left(a_{\sigma 3} + a_{\sigma 4} dF_z\right)|\lambda|] + \left(a_{\sigma 1} + a_{\sigma 2} dF_z\right) \tag{3.40}$$

The component σ_{x,F_z} takes into account the influence of the vertical tire load on the relaxation length:

$$\sigma_{x,F_z} = F_z\left(a_{\sigma 5} + a_{\sigma 6} dF_z\right) \exp(-a_{\sigma 7} dF_z) \frac{r_w}{F_{z,n}} \tag{3.41}$$

where $F_{z,n}$ is the nominal tire vertical force.

Coefficients $a_{\sigma 1}$ - $a_{\sigma 7}$ can be obtained by fitting corresponding experimental data derived from the tire test rig, as it was done for example in [90, 92]. In this work a method on the identification of polynomial coefficients is based on offline optimization involving available road tests. The cost function for optimization routines is formulated as follows:

$$J_{\sigma_x} = w_1 \frac{|F_{x,exp} - F_{x,sim}|}{\max\left(|F_{x,exp}|\right)} + w_2 \frac{|\omega_{w,exp} - \omega_{w,sim}|}{\max\left(|\omega_{w,exp}|\right)} \tag{3.42}$$

From the cost function, one can see that optimization procedure is aimed at the minimization of the deviation between simulated and experimental values of tire force and wheel velocity. Wheel torque and force measurements during preliminary testing of WSC were used as the experimental data. To avoid overlapping or inaccuracies in the complex vehicle model, a single corner wheel dynamics model was utilized on the side of simulation. Information about measured tire vertical force, vehicle velocity and brake pressure was sent to the simulation model to perform calculation of the longitudinal tire force. To assess benefits of using this approach, three modeling methods were compared between each other:

- Steady state tire model without consideration of the first-order tire dynamics,
- Tire model with first-order transient tire force dynamics and constant value of tire relaxation length,
- Tire model with first-order transient tire force dynamics and nonlinear model of tire relaxation length.

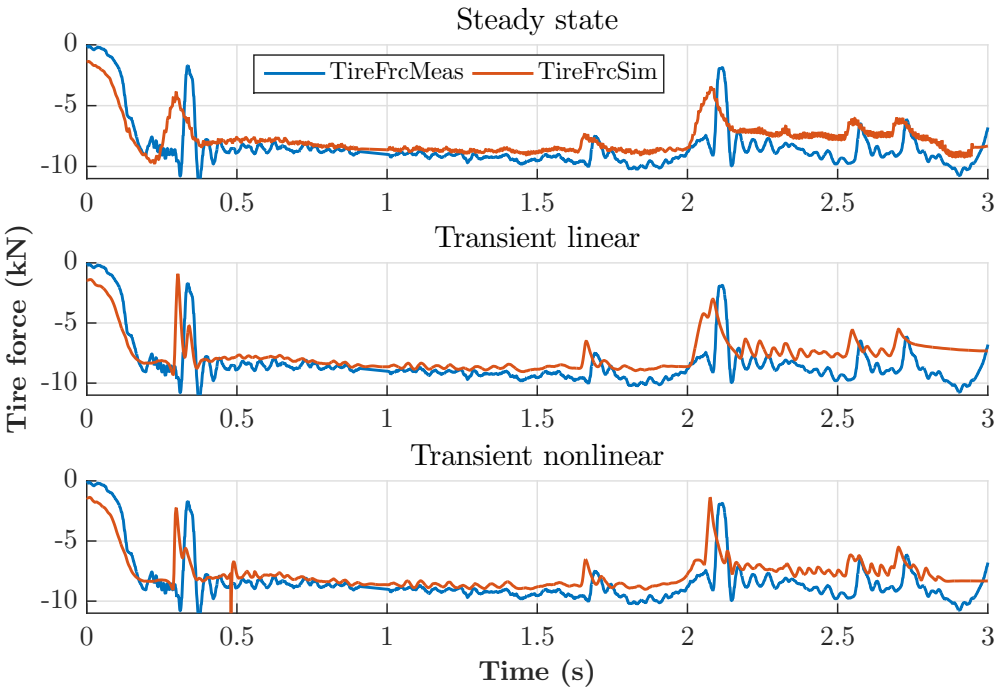

Fig. 3.9 Tire force during the braking with WSC

As it can be seen in Figure 3.9, steady state tire model does not capture delays in tire force generation during dynamic brake torque application in time periods between 0.3-0.5 s and 2.0-2.3 s. This reflect in relative high deviations of the wheel speed, as a consequence,

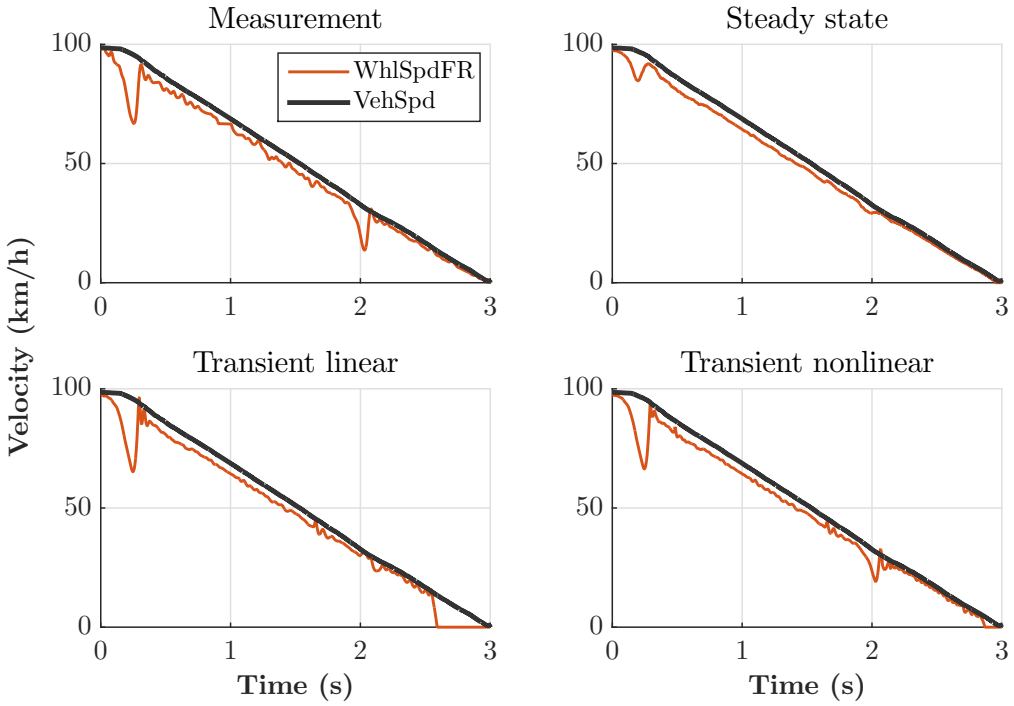

Fig. 3.10 Wheel speed during the braking with WSC

which can be clearly seen on the velocity profile in Figure 3.10. Better results were obtained for the tire model with the considered tire dynamics and a constant relaxation length. This approach reduces phase deviations in tire longitudinal force and improves the overall picture of velocity profile, as it can be seen in Figures 3.9 and 3.10, respectively. However, RSMD of the tire force is higher compared to the steady state model even in the presence of reduction of velocity deviation. This can be seen in Table 3.6 where the numerical assessment of model accuracy was summarized. The best results were obtained using the tire model with nonlinear relaxation length dependency on wheel slip and vertical force. This model has the lowest RMSD in case of longitudinal tire force and wheel speed, which is well reflected qualitatively in Figures 3.9 and 3.10 and quantitatively in Table 3.6. As soon as this approach provides wheel speed deviation less than WSC-relevant vehicle velocity (5 km/h), this approach is further utilized for the simulation purposes.

Table 3.4 Tire model validation

State RMSD	Steady state	Transient linear	Transient nonlinear
Longitudinal tire force, (kN)	1.47	1.85	1.46
Wheel speed, (km/h)	1.17	1.03	0.52

3.4 Validation of the vehicle model

Validation of the proposed vehicle dynamics model was done using testing data acquired during tests performed with the real vehicle demonstrator and simulations produced in the commercial simulation software CarMaker. For this purpose, corresponding control demand from experimental data (brake pressure, powertain torque, steering wheel angle and others) were used in both simulation environments. Evaluation of the control accuracy was done based on the comparison of the relevant vehicle states.

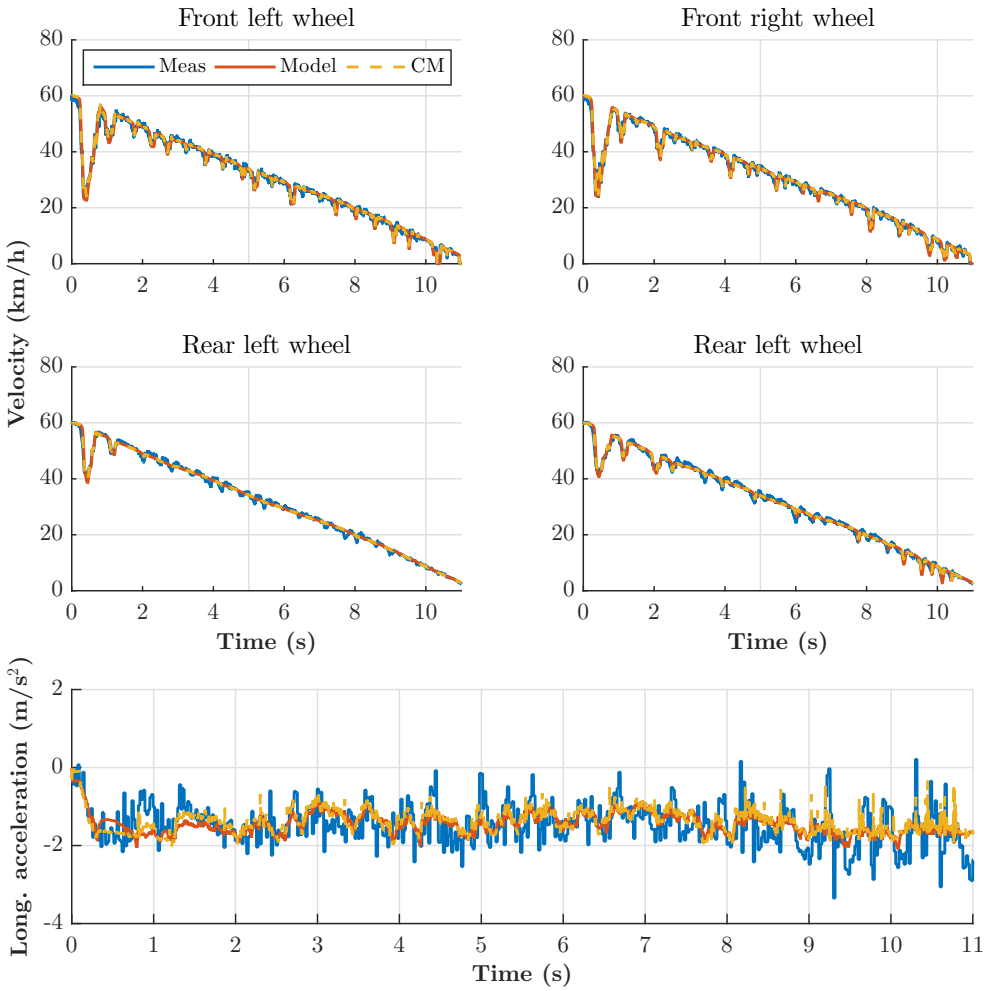

Fig. 3.11 Wheel speed and vehicle acceleration profiles during ABS braking in low road friction conditions

For the validation of longitudinal vehicle dynamics, ABS-braking tests were considered. Tests with the vehicle demonstrator were performed by using standard HCU with rule-based

ABS control logic utilized in the serial production vehicles. This was done to assess model accuracy during periodic brake torque application when the wheel slip is held in the nonlinear area of the force-wheel slip diagram. Corresponding ABS braking tests were performed both in the low and in the high road friction conditions at Lommel proving ground. Wheel speed, wheel slip, vehicle velocity, vehicle longitudinal acceleration were selected as the relevant states for the validation of the developed vehicle model.

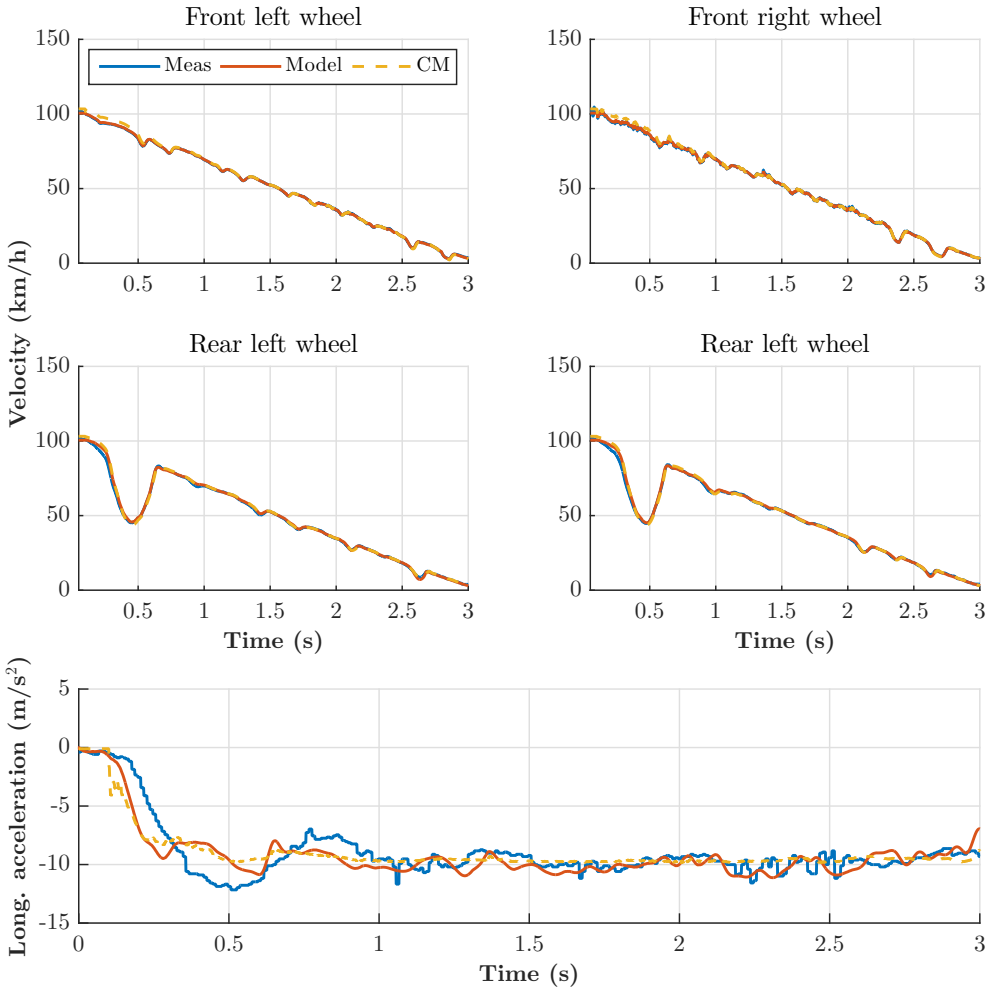

Fig. 3.12 Wheel speed and vehicle acceleration profiles during ABS braking in high road friction conditions

Figures 3.11 and 3.12 represent validation results obtained in experiment, with developed vehicle dynamics model and commercial vehicle software IPG CarMaker. As it can be seen, wheel speed profile of the front wheels is very close to the experimental results in high as

well as in low road friction conditions. Higher deviations of the rear wheel speed profiles happen due to lower amplitudes of the brake torque demand on the rear axle. This can happen due to possible inaccuracies in brakes friction model, as soon as lining coefficient of friction was considered to be constant in simulation. It is also important to admit that there is also not much difference between developed and commercial vehicle simulation software, as both of them use the same tire and brake system model.

Table 3.5 Validation of the vehicle model during ABS braking

State RMSD	Low road friction		High road friction	
	Simulation model	IPG CarMaker	Simulation model	IPG CarMaker
Vehicle deceleration, (m/s^2)	0.23	0.29	0.49	0.59
Vehicle velocity, (km/h)	1.0	1.2	1.0	1.3
Wheel speed FL, (km/h)	1.3	0.9	0.4	1.2
Wheel speed FR,(km/h)	2.5	2.4	2.7	3.2
Wheel speed RL, (km/h)	3.7	3.7	3.5	3.6
Wheel speed RR, (km/h)	3.8	3.7	3.3	3.5
Wheel slip FL, (km/h)	0.08	0.08	0.03	0.04
Wheel slip FR, (km/h)	0.08	0.08	0.02	0.03
Wheel slip RL, (km/h)	0.04	0.07	0.04	0.05
Wheel slip RR, (km/h)	0.07	0.07	0.03	0.04

Numerical assessment of RMSD for the considered vehicle states is summarized in Table 3.6. As it can be seen, RMSD wheel slip on the front wheels does not overshoot 8 % of deviation from experiment in high road friction conditions, and 4 % in low friction conditions. For the rear wheels, the value of wheel slip RMSD is not higher than 7 % and 5 % for the high and low road friction conditions. Such results allow concluding that the developed models are accurate enough considering measurement noise and inhomohenous road friction conditions, which usually occur during experimental tests.

For the validation of lateral vehicle dynamics, steady state and transient vehicle maneuvers were analyzed. Testing procedure, described in the standard [93], allows estimating vehicle steering characteristics during steady circle vehicle motion. The vehicle moves in a circle with the radius of 30 meters, while the vehicle velocity is progressively increased to achieve maximally possible lateral acceleration for the given road friction conditions. Besides comparison of such vehicle states, as yaw rate, lateral acceleration and sideslip angle, this testing procedure allows determining the vehicle steer characteristics or so-known understeer gradient.

On the obtained validation results in Figure 3.13, it can be seen that in the steady state driving mode relevant vehicle states have neglectable deviation from the experimental results. Slight difference between simulation and experiment occurs on the understeer gradient close

to the handling limits. This could occur due to inaccuracies in tire model parametrization for combined slip cases. Despite this fact, deviation of the lateral acceleration is not higher than 5 % from maximal values, as it is indicated in Table 3.6.

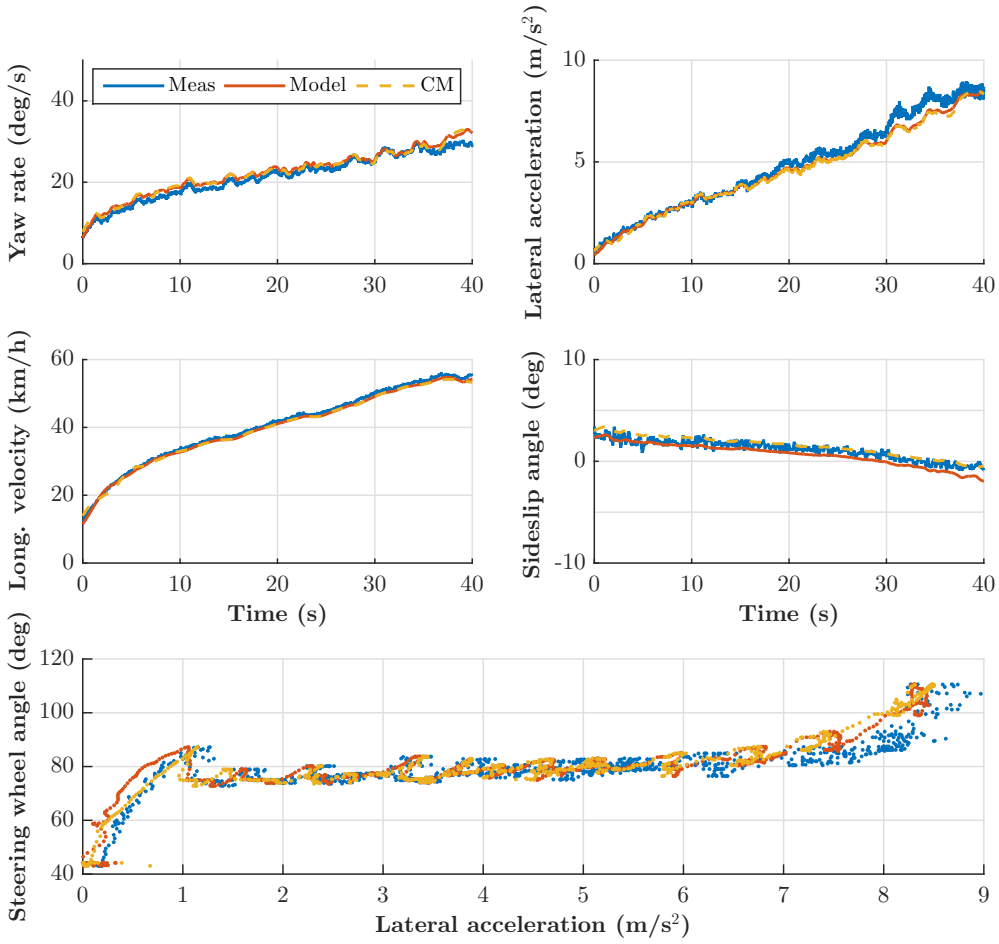

Fig. 3.13 Steady circle test

Standard testing procedure from [94] describes open-loop vehicle test for evaluating vehicle lateral transient behavior. In the standard procedure, steering wheel angle is selected in such way that vehicle reaches 4 m/s^2 or 6 m/s^2 at steady state phase. In the performed test, vehicle was forced to drive at maximally possible lateral vehicle acceleration driving at handling limits after reaching steady conditions. This allows analyzing wider range of the lateral tire characteristics considering not only linear but also non-linear region of the F_y - α. The steering angle rate should be fixed at the rate of 200 deg/s. Figure 3.14 presents main vehicle states during the step response test. It can be seen that lateral acceleration and yaw rate have neglectable deviation in absolute value from the experimental results.

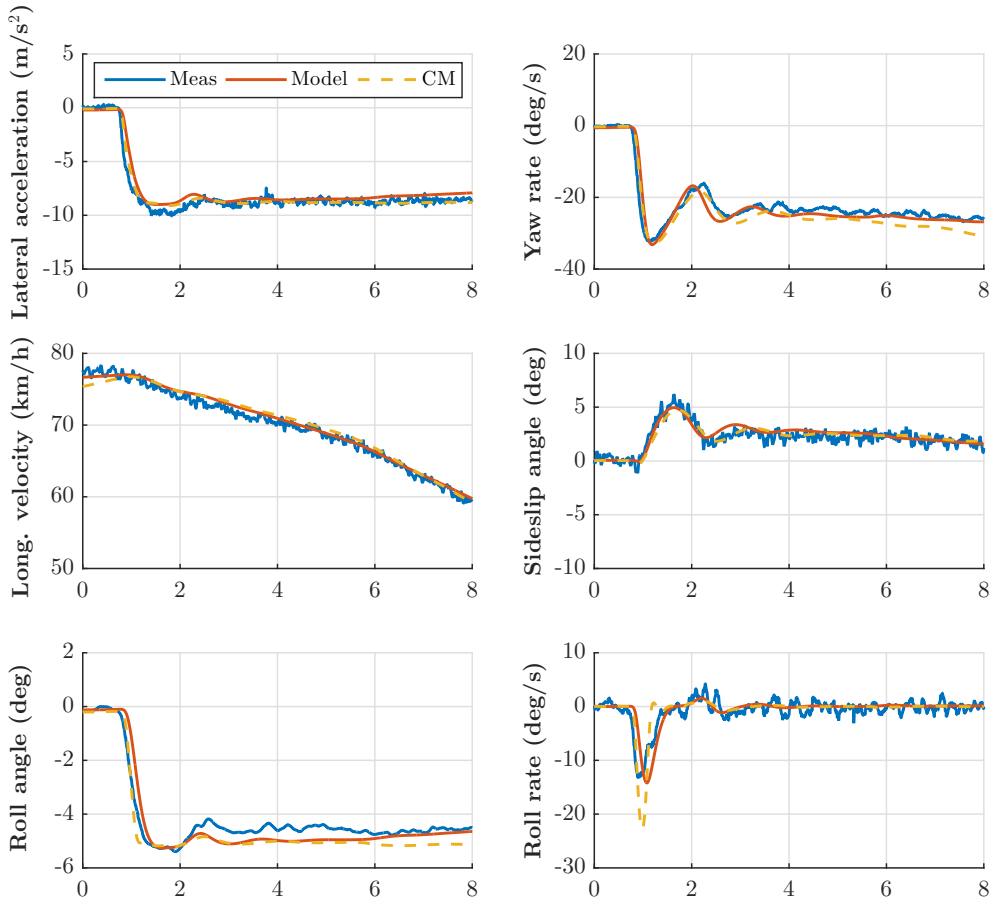

Fig. 3.14 Vehicle step response

In terms of the yaw rate behavior, developed vehicle model has some higher phase shift in relation to experiment than commercial vehicle software. This occurs due to simpler suspension modelling approach, while commercial vehicle dynamics software has suspension model with higher fidelity considering kinematics and compliance. In terms of roll vehicle behavior, both vehicle models have higher deviations from the experimental data. Accuracy of the measurement device should be considered here: roll angle and roll rate were measured by two GPS sensors mounted on the top of the vehicle. Such measurement system usually provides systematic error. Therefore, despite some deviation from the experiment, on the qualitative level, roll vehicle behavior can be considered as valid. Numerical assessment of the deviations are presented in Table 3.6 and allows summarizing validity of the vehicle model and system parametrization.

Table 3.6 Validation of the vehicle model during lateral vehicle motion

State RMSD	Steady cornering		Step response	
	Simulation model	IPG CarMaker	Simulation model	IPG CarMaker
Lateral acceleration, (m/s^2)	0.35	0.40	0.74	0.35
Yaw rate, (deg/s)	1.3	1.3	2.3	2.3
Vehicle long. velocity, (km/h)	0.7	1.0	0.6	0.7
Sideslip angle, (deg)	0.8	0.7	0.5	0.5
Roll angle, (deg)	0.5	0.3	1.2	1.4
Roll rate, (deg/s)	0.7	0.7	1.8	1.9

3.5 Chapter summary

In this chapter, mathematical description of the vehicle motion was derived. Various approaches in modeling of vehicle subsystems were analyzed and validated with test results obtained with physical systems and vehicle. From performed simulation studies, following conclusions can be drawn:

- Nonlinear brake system model provides more accurate results than linear one. Despite that, linear model can be used for further system analysis, while nonlinear is considered for the simulation studies.
- Transient tire model reproduces tire force behavior as in experiment. Higher RMSD values can be explained by the difference in road coefficient of friction, which was considered to be constant in simulation.
- Simulation of OBM powertain present possible issues in WSC and need in inclusion of torsional dynamics compensator in brake blending algorithm.
- Developed vehicle model as well modeling approaches applied to the vehicle chassis systems correlate well with experimental results obtained during hardware-in-the-loop and road tests with the vehicle demonstrator.
- Developed vehicle model as well as commercial software can be used for simulation studies. As an advantage, commercial software includes kinematics and compliance of suspension system and provides more realistic tire vertical forces distribution, while simpler suspension model was utilized in developed model.
- Mathematical description of vehicle motion was validated and can be further used for designing state and parameter observer.

Chapter 4

Development and analysis of control algorithms

4.1 Control objectives and assessment criteria

As it comes from the definitions of the brake and ABS system, presented in section 1.2, developed control system should fulfill following requirements providing:

- Service braking of the vehicle with providing expected braking performance independently from the utilized actuators;
- Wheel slip control in emergency braking cases to achieve maximally possible vehicle deceleration as demanded by driver;
- Reference wheel slip adaptation to produce WSC operation close to maximal braking force;
- Wheel slip control without deterioration of the longitudinal ride quality;
- State and parameter observer to provide required information to the control system.

To make a conclusion about fulfillment of aforementioned requirements, a set of relevant numerical criteria should be used for the evaluation. Assessment of the developed braking control functions includes standardized recommendation as well as evaluation metrics for characterizing control quality. Mean acceleration and braking distance are the classical evaluation metrics known from standard testing procedures, e.g. see [95]. This standard describes testing procedure for the vehicle equipped with anti-lock braking system and

provides recommendations for evaluation of braking performance. However, known standardized methodologies does not include assessment of the control performance, which directly influences system robustness and ride quality during the braking. For this purpose, additional evaluation metrics are proposed in this section. ABS index of performance (ABSIP) was initially proposed in [96]. This criterion assesses relation between the mean acceleration of the vehicle with activated ABS against the case where ABS is deactivated:

$$ABSIP = \frac{\overline{a_{ABS}}}{\overline{a_{woABS}}} \tag{4.1}$$

where $\overline{a_{ABS}}$ and $\overline{a_{woABS}}$ is the mean vehicle deceleration with activated and deactivated ABS control, respectively.

However, according to the existing regulations in European Union, all new manufactured vehicles must be equipped with ABS. Therefore, it is more preferable to compare braking performance of the developed WSC and classical rule-based ABS approaches. Proposed WSC index of performance (WSCIP) presents such assessment:

$$WSCIP = \frac{\overline{a_{WSC,1}}}{\overline{a_{WSC,2}}} \tag{4.2}$$

where $\overline{a_{WSC}}$ is the mean deceleration during the braking with activated WSC.

Developed WSC should guarantee precise tracking of the given (or estimated) wheel slip setpoint. For this purpose, root mean square deviation (RMSD) of the error between measured and reference wheel slip evaluates control quality of the WSC:

$$RMSD_{\lambda_{ij}} = \sqrt{\frac{1}{n}\sum_{k=1}^{n}\left(\lambda_{ij} - \lambda_{ij}\right)^2} \tag{4.3}$$

One of the main issues related to the WSC relates to the first peak of the measured wheel slip at the beginning of braking. For this purpose, maximal value of the wheel slip at the initial stage of braking is added to evaluate system adaptability:

$$FP_{\lambda_{ij}} = max\left(\left|\lambda_{ij}\left(\tau\right)\right|\right), \tau = [t_1 \ldots t_2], \tag{4.4}$$

where time t_1 and t_2 correspond to the initial phase of braking.

In the most of technical sources, only braking performance of ABS is assessed [95, 96]. However, driver experiences oscillations in longitudinal direction owing to the tire forces fluctuations in ABS mode. To evaluate influence of oscillations in longitudinal acceleration on ride quality during the braking, standard deviation (STD) of vehicle jerk can be used for numerical assessment of ride quality:

$$STD_{j_x} = \sqrt{\frac{1}{n}\sum_{k=1}^{n}(j_x)^2} \tag{4.5}$$

where j_x is the longitudinal vehicle jerk.

This metric can be easily obtained in simulation or in hardware-in-the-loop tests. However, it is not always possible to obtain first derivative of the longitudinal vehicle deceleration without significant noise. In such cases, standard deviation of the vehicle deceleration can be used similar to Equation 4.6:

$$STD_{a_x} = \sqrt{\frac{1}{n}\sum_{k=1}^{n}(a_x)^2} \tag{4.6}$$

This evaluation criteria are further applied to the obtained experimental results. Giving a short overview of performed theoretical and practical analysis of developed controls, simulation studies and experimental investigations were thematically separated. Number of tests and procedures depended on the available vehicle demonstrators and testing facilities. Table 4.1 gives overall view on the performed testing activities. Detailed description of the control algorithms, mentioned in Table 4.1, is provided in next subsections.

Table 4.1 Testing techniques applied to the developed control algorithms

Control	Brake system type		
	Simulation	Hardware-in-the-loop	Vehicle tests
WSC PI and brake blending	-	OBM DEHB	OBM DEHB
WSC PI	OBM DEHB, DEHB	DEHB	OBM DEHB, DEHB
WSC PI RA	DEHB	-	DEHB
WSC SMPI RA	DEHB	-	DEHB
WSC ISM RA	DEHB	-	DEHB
WSC SMPI	DEHB	DEHB	DEHB
WSC ISM	DEHB, IWM	DEHB	DEHB, IWM
WSC FOSM	IWM	-	IWM
WSC VSPI	IWM	-	IWM
WSC CTA	IWM	-	IWM
State estimation	-	-	OBM DEHB, DEHB

4.2 Control architecture

The brake system controller was designed to produce interfaces to main vehicle dynamics control systems and chassis components. Figure 4.1 presents principle control components

interfering with vehicle hardware components. Information obtained from the vehicle sensors includes driver intention, state of the vehicle and eventual information about the road situation obtained by ADAS-relevant sensors. Driver intention is interpreted from the measurements of the brake pedal position, while vehicle states are obtained by conventional sensors (e.g. wheel speed sensors, gyroscope, accelerometer). ADAS-relevant sensors (e.g. camera) can be used for initial estimation of the reference wheel slip or road coefficient of friction, where interested can refer to the research supervised by the author [97].

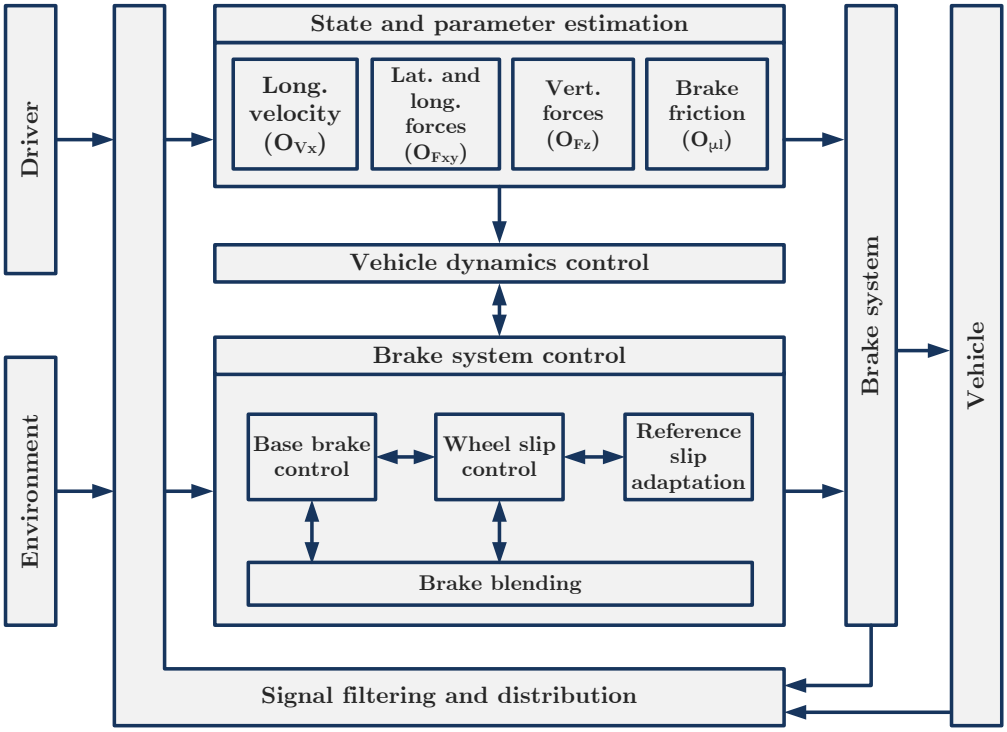

Fig. 4.1 Architecture of brake system control

Measurements are further post-processed, filtered and composed in the signal bus, which is later transmitted to the control system. This includes state estimator responsible for providing the observation of non-measurable system states and parameters. In this research, a global state observer was developed, main functional modules of which include estimation of tire forces, vehicle longitudinal velocity, sideslip angle, pitch and roll angles. These states are transferred to the vehicle dynamics controller serving as the supervisory control part of the vehicle. This interacts with the following core functional modules of the brake system:

- Base brake controller responsible for the main braking functions, such as service braking and brake force distribution;

- Wheel slip controller performing functions of the continuous anti-lock brake system during the hard braking events or, eventually, during vehicle stability control;
- Reference wheel slip estimation providing estimation and adaptation of the optimal wheel slip to WSC system;
- Depending on the vehicle configuration, brake blending algorithms responsible for the brake torque demand distribution in combined (hybrid) brake system consisting of electric motors and friction brake system.

Obtained control signals are forwarded to the corresponding brake system actuators, providing desired vehicle motion. Next subsections present detailed description of the main signal processing procedures, state estimation, base brake control, brake blending and wheel slip control functions.

4.3 Vehicle state and parameter estimation

Idea of indirect system state measurement comes from the paper [98]. This approach proposed reconstruction of the unmeasurable system states and parameters. This problem is also very actual for the WSC, where wheel slip (main control variable) cannot be directly measured. Nowadays, various estimation approaches are existing and widely used in mechatronic system control. From the known methods, Kalman filter provides an attractive estimation tool, which can be applied to linear as well to nonlinear systems.

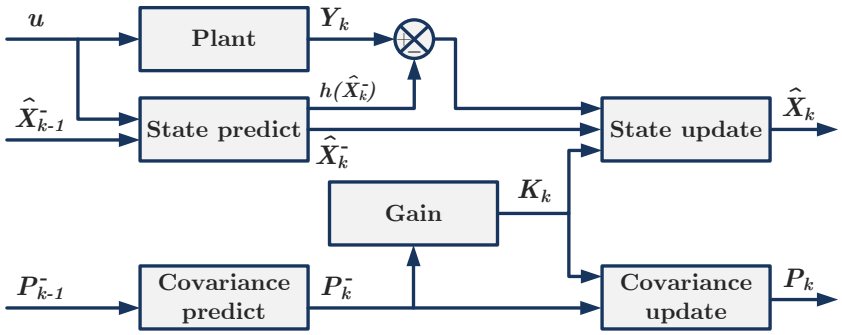

Fig. 4.2 Kalman filter

Compared to the Luenberger observer, Kalman filter is designed for time varying or stochastic processes. This can handle state and measurement noise, which are assumed to be

white noise in classical Kalman filter formulation. Estimation procedure of this type of state observer are schematically presented in Figure 4.2. Fundamentally all physical phenomena happen in continuous time and can be mathematically described by the set of equations as continuous processes. In practice, measurements are performed in discrete time. Therefore, continuous formulations of state equations have to be expressed as state space time-invariant discrete system for designing state observer.

Another important point in state estimation is evaluation of system observability. Its definition was introduced by Kalman in [99]. The system is said to be observable at time t_0 with the state $x(t_0)$ if it is possible to determine this state by using measurements of the system output over a finite time interval $0 \geq t \geq t_2$ [100]. In other words, addressing observability problem allows to conclude if it is possible or not to reconstruct unknown system states from the available measurements. This problem exists for linear and nonliear systems and has different mathematical solutions. The case of linear system can be straightforward evaluated from the state space system formulation as described in [99], while nonlinear systems require more sophisticated mathematical approaches as shown in [77].

Next subsections introduce mathematical description of developed state and parameter estimator, shown in Figure 4.1. By using modular system architecture and linear representation of vehicle and system dynamics, it was possible to obtain necessary longitudinal, lateral and vertical tire states without inclusion of parametrized non-linear tire model and high computation load while using e.g. unscented Kalman filter [101].

4.3.1 Longitudinal vehicle velocity observer

In the most of ABS algorithms, estimation of the longitudinal vehicle velocity is based on the wheel speed information which are forced to operate in a cycling mode. When the wheel speed lies close to the vehicle velocity ($t = [t_1\ t_2]$) and wheel is considered to be unlocked, the value of the vehicle velocity is determined by the wheel velocity, Figure 4.3. During time frame ($t = [t_2\ t_3]$), acceleration of the vehicle is calculated and assumed to be constant during time period where all four wheels are tending to lock. During $t = [t_1\ t_2]$, calculated acceleration is integrated and vehicle velocity is derived. This procedure repeats until ABS is deactivated or the vehicle stops.

In continuous WSC, where all four wheels are intended to be kept at reference value, such strategy of vehicle velocity estimation is not applicable. Therefore, to provide accurate estimation of the vehicle velocity in continuous WSC, installation of longitudinal vehicle acceleration sensor is required. This signal should be filtered and shifts in acceleration measurements, occurring due to sensor installation, must be eliminated [102]. Bias estimation is based on measurements of vehicle and wheels accelerations. Additional set of rules is

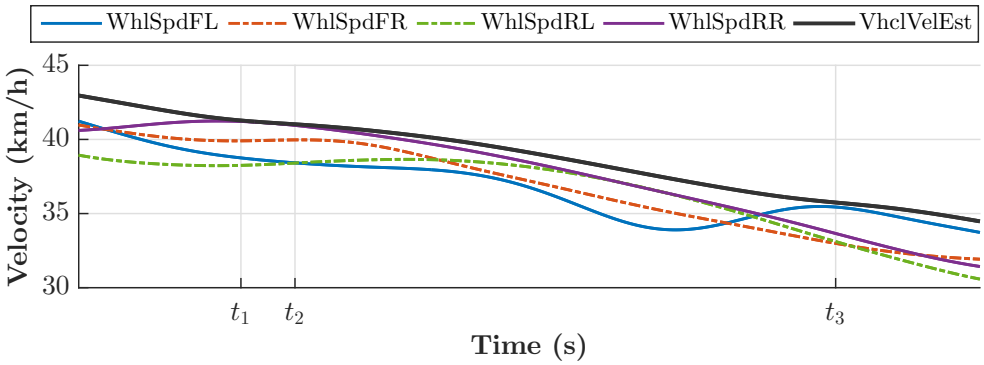

Fig. 4.3 Vehicle velocity estimation in conventional ABS

applied to avoid improper estimation of measurement bias under certain driving conditions. Figure 4.4 demonstrates bias estimation and its influence on the estimation of the vehicle velocity. For this purpose, vehicle velocity is derived by integrating acquired longitudinal acceleration signal. As it can be seen, vehicle velocity obtained from the corrected acceleration is almost the same as reference measurements obtained with optical sensor. By using measured acceleration without correction, produced results represent significant deviation from the reference velocity measurements.

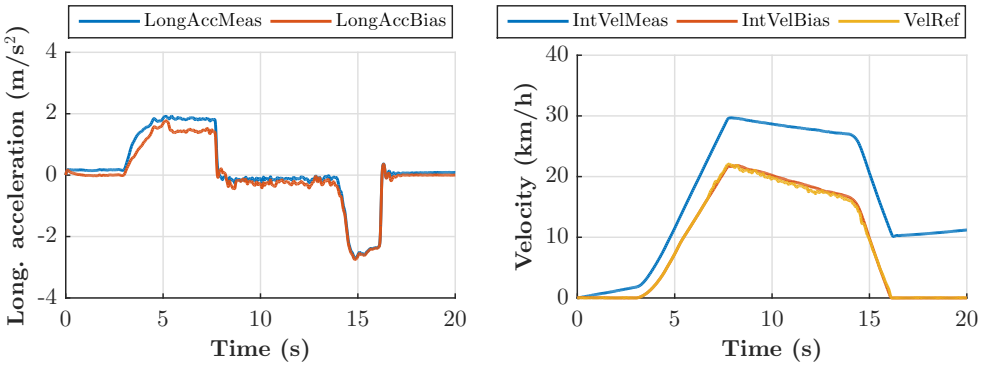

Fig. 4.4 Bias estimation of longitudinal acceleration sensor

Wheel speeds needed to be translated to the vehicle center of gravity of the vehicle for the motion in curve cases [102]. Considering relatively small values of the sideslip angle they can be represented as [103]:

$$
\begin{aligned}
V_{w,cog}^{FL} &= \omega_w^{FL} r_w^{FL} cos\delta_w^{FL} + \dot{\psi}\frac{t_f}{2} \\
V_{w,cog}^{FR} &= \omega_w^{FR} r_w^{FL} cos\delta_w^{FR} - \dot{\psi}\frac{t_f}{2} \\
V_{w,cog}^{RL} &= \omega_w^{RL} r_w^{RL} + \dot{\psi}\frac{t_r}{2} \\
V_{w,cog}^{RR} &= \omega_w^{RR} r_w^{RR} - \dot{\psi}\frac{t_r}{2}
\end{aligned}
\tag{4.7}
$$

Figure 4.5 presents wheel speed profiles during the slalom tests. As it can be seen, there is a considerable deviation of the wheel speeds from the vehicle velocity, measured by GPS sensor, if transformation is not applied. By considering yaw motion of the vehicle, as presented in Equation 4.7, wheel speed sensors have closely the same values as measured vehicle velocity. Therefore, such transformation allows accurate estimation of the longitudinal vehicle velocity also during lateral vehicle motion.

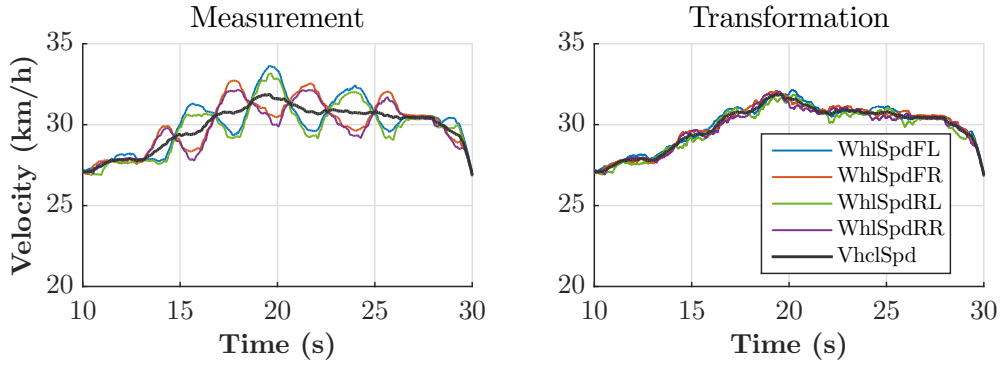

Fig. 4.5 Wheel velocities during slalom maneuver

Considering aforementioned measurements, governing equation for the vehicle velocity estimator O_{V_x} is formulated as

$$
\dot{V}_x = a_x^{meas} + g\sin\chi_{road} + V_y\dot{\psi} \tag{4.8}
$$

where a_x^{meas} is the measured longitudinal acceleration of the vehicle, χ_{road} is the road grade.

Representing equations in a discrete state space form, state vector is obtained according to

$$
\underbrace{\begin{bmatrix} a_x \\ V_x \end{bmatrix}}_{x_{k+1}} = \underbrace{\begin{bmatrix} 1 & 0 \\ T_s & 1 \end{bmatrix}}_{A} \underbrace{\begin{bmatrix} a_x \\ V_x \end{bmatrix}}_{x_k} + \underbrace{\begin{bmatrix} 1 \\ T_s \end{bmatrix}}_{B} \underbrace{\dot{\psi}\hat{V}_y}_{u_k} \tag{4.9}
$$

where T_s is the sampling time.

The measurement vector includes information from vehicle acceleration and wheel speed sensors:

$$\underbrace{\begin{bmatrix} a_x \\ V_{w,cog}^{FL} \\ V_{w,cog}^{FR} \\ V_{w,cog}^{RL} \\ V_{w,cog}^{RR} \end{bmatrix}}_{y_k} = \underbrace{\begin{bmatrix} 1 & 0 \\ 0 & 1 \\ 0 & 1 \\ 0 & 1 \\ 0 & 1 \end{bmatrix}}_{C} \underbrace{\begin{bmatrix} a_x \\ V_x \end{bmatrix}}_{x_k} \tag{4.10}$$

In the proposed estimator, covariance matrices are adapted according to the wheel lock status. Determination of the wheel lock status is sophisticated procedure, as this logic cannot use wheel slip as an criterion causing algebraic loop [104]. In this research, it is proposed to use wheel acceleration to determine wheel status providing reliable and robust solution. For this purpose, the acceleration of each wheel is compared to the filtered longitudinal vehicle acceleration. High deviations between wheel and vehicle accelerations indicate wheel lock. This approach is represented by the following set of empirical rules:

$$\begin{cases} \nu_{cor}^{k} = sat_0^{\nu_{max}}(\nu_{cor}^{k-1} + \nu_{inc} T_s), & \text{if } \dot{\omega}_w r_w > a_x \pm a_x^{th} \\ \nu_{cor}^{k} = sat_0^{\nu_{max}}(\nu_{cor}^{k-1} - \nu_{dec} T_s), & \text{otherwise} \end{cases} \tag{4.11}$$

where ν_{cor} is the correction factor, ν_{max}, ν_{inc} and ν_{dec} are positively defined and calibrated maximal, increment and decrement values of the correction factor, a_x^{th} is the deceleration threshold.

The wheel acceleration signal in the case of its direct derivation from the wheel speed produces a very noisy signal. Therefore, appropriate filtering procedure should be applied to derive wheel acceleration. To avoid phase shifts in the wheel acceleration signal, a linear Kalman filter is used with following state space formulation:

$$\begin{bmatrix} \omega_{w,k}^{ij} \\ \dot{\omega}_{w,k}^{ij} \end{bmatrix} = \begin{bmatrix} 1 & T_s \\ 0 & 1 \end{bmatrix} \begin{bmatrix} \omega_{w,k-1}^{ij} \\ \dot{\omega}_{w,k-1}^{ij} \end{bmatrix} \tag{4.12}$$

This approach requires proper tuning of the adjustment factors in Equation 4.11, but offers robust method on estimation of the longitudinal velocity and provides accurate estimation of the wheel slip. Next section describes estimation of longitudinal tire forces, which are necessary for further determination of the reference wheel slip value. To cover use cases with combined slip, estimation of lateral tire forces and sideslip angle are introduced.

4.3.2 Longitudinal and lateral tire forces observer

By using bicycle vehicle model it is possible to obtain lateral vehicle velocity and lumped lateral forces on the front and on the rear axles.This model shows a good correlation with the real vehicle behavior in the situations where traction or braking are not applied during vehicle cornering maneuvers. However, such approach will not provide accurate tire forces estimation for combined slip cases during cornering. To resolve this issue, double track planar vehicle model can be utilized. Instead of individual, lumped tire forces should be considered in state equations to obtain observable system representation. Referring to equations of longitudinal, lateral and yaw vehicle motion, as well as wheel dynamics, following system description was obtained:

$$\begin{cases} m_v a_x = F_x^{FL} cos\delta_{FL} + F_x^{FR} cos\delta_{FR} + F_x^{RL} + F_x^{RR} + F_y^R sin\delta_F \\ J_w^{ij} \dot{\omega}_{ij} = F_x^{ij} r_w - T_b^{ij} \\ m_v a_y = F_x^{FL} sin\delta_{FL} + F_x^{FR} sin\delta_{FR} + F_y^F cos\delta_F + F_y^R \\ I_{zz} \ddot{\psi} = l_f \left(F_x^{FL} sin\delta_{FL} + F_x^{FR} sin\delta_{FR} + F_y^F cos\delta_F \right) - l_r F_y^R \\ - \dfrac{t_f}{2} \left(F_x^{FL} cos\delta_{FL} + F_x^{FR} cos\delta_{FR} + F_y^F sin\delta_F \right) \\ - \dfrac{t_r}{2} \left(F_x^{RL} + F_x^{RR} \right) \end{cases} \tag{4.13}$$

Considering such system description, additional online calculations of the steady-state tire forces are usually required. It means that such approach requires tire model parametrizatione. To produce estimation without knowledge about tire characteristics, longitudinal and lumped lateral tire forces can be considered as the random-walk process (see Appendix A). As a result, following discrete system representation was obtained:

$$\begin{cases} F_{x,k+1}^{ij} = F_{x,k}^{ij} \\ \omega_{w,k+1} = \omega_{w,k} + T_s \left[\dfrac{F_x^{ij}}{J_w} \right] \\ F_{y,k+1}^{i} = F_{y,k}^{i} \\ V_{y,k+1} = V_{y,k} + T_s \left[\dfrac{F_x^{FL} sin\delta_{FL} + F_x^{FR} sin\delta_{FR} + F_y^F cos\delta_F + F_y^R}{m_v} - V_x \dot{\psi} \right] \\ \dot{\psi}_{k+1} = \dot{\psi}_k + T_s \left[\dfrac{l_f}{I_{zz}} \left(F_x^{FL} sin\delta_{FL} + F_x^{FR} sin\delta_{FR} + F_y^F cos\delta_F \right) - \dfrac{l_r}{I_{zz}} F_y^R \right. \\ \left. + \dfrac{t_f}{2I_{zz}} \left(F_y^F sin\delta_F + F_x^{FR} cos\delta_{FR} - F_x^{FL} cos\delta_{FL} \right) + \dfrac{t_r}{2I_{zz}} \left(F_x^{RR} - F_x^{RL} \right) \right] \end{cases} \tag{4.14}$$

Besides lateral and longitudinal tire forces, it is possible to obtain lateral vehicle velocity, which is later can be used for calculation of sideslip angle. Therefore, state vector includes following states:

$$X = \begin{bmatrix} F_x^{FL} & F_x^{FR} & F_x^{RL} & F_x^{RR} & F_y^{F} & F_y^{R} & V_y & \dot{\psi} \end{bmatrix}^T \tag{4.15}$$

Output vector consists of measurements obtained from wheel speed sensors, gyroscope and accelerometer, which are usually used in vehicle dynamics control system:

$$Y = \begin{bmatrix} a_x & \omega_w^{ij} & a_y & \dot{\psi} \end{bmatrix}^T \tag{4.16}$$

Control vector includes four input torques. They can be quite precisely obtained from electric motors or estimated by using pressure sensors of DEHB:

$$U = \begin{bmatrix} T_w^{FL} & T_w^{FR} & T_w^{RL} & T_w^{RR} \end{bmatrix}^T \tag{4.17}$$

Proposed state estimation scheme is based on the knowledge of the input values of wheel motor torque or friction brake torque. In the latter case, calculations of the wheel torque are based on the brake pressure estimation and known parametrization of the brakes. Referring to the Equation 3.26, it can be seen that μ_{br} has a crucial influence on the torque generated by the friction brake system. This parameter is never constant and significantly varies under different system states and strongly influenced by environmental conditions [105]. To avoid inaccuracies in input vector, estimation of the brakes coefficient of friction is additionally designed. Using Equations 3.31 and 3.26, following state equation is obtained:

$$\mu_{br} = \frac{-J_{w,eq}\dot{\omega} + r_w F_x - r_w F_{rr}}{n_{bp} F_{cl} r_d}. \tag{4.18}$$

In Equation 4.18, equivalent inertia $J_{w,eq}$ is calculated as

$$J_{w,eq} = J_w + m_{qc} r_w^2 \tag{4.19}$$

where J_w is the inertia of the wheel, m_{qc} is the mass of the quarter car.

Equation 4.18 leads to the fitting problem where the brake coefficient of friction μ_{br} is fitted to the measured data in the right-hand side of this equation. To solve this task in real-time, linear recursive least squares (RLS) approach was used.

Lumped lateral tire forces are further separated to individual wheel forces by estimating vertical tire load distribution between left and right wheels:

$$F_y^{ij} = F_y^i \frac{F_z^{ij}}{F_z^{iL} + F_z^{iR}} \tag{4.20}$$

Equation 4.20 presents linear relationship between lateral and vertical tire forces distribution. In practice, such assumption about linear relation usually follows to inaccuracies in individual lateral forces estimation. Therefore, following nonlinear relationship is used for estimation of individual lateral forces:

$$F_y^{ij} = F_y^i f\left(\frac{F_z^{ij}}{F_z^{iL} + F_z^{iR}}\right) \tag{4.21}$$

where nonlinear function f is presented by look-up tables. Its shape is based on experimental measurements and presented in Figure F.5.

As it was mentioned previously, with knowledge of lateral and longitudinal vehicle velocity, it is possible to directly derive sideslip angle:

$$\begin{cases} \beta = 0, & \text{if } V_x \leq 5 \text{ km/h} \\ \beta = \arctan(\frac{\hat{V}_y}{\hat{V}_x}), & \text{otherwise} \end{cases} \tag{4.22}$$

Estimation of the vertical tire forces, required for lateral forces observer $O_{F_{xy}}$ is explained in the next subsection.

4.3.3 Vertical tire forces observer

To provide accurate estimation of vertical tire forces, pitch and roll dynamics should be considered in state space system representation. These states can be obtained by open-loop calculations based on the suspension travel sensors. Referring to geometrical relationship between pitch and roll angles and suspension travel (Figure 3.2), following estimation can be applied [77]:

$$\theta = \frac{\Delta_{FL} - \Delta_{RL} + \Delta_{FR} - \Delta_{RR}}{2L} - \frac{m_v a_x h_{cog}}{K_p} \tag{4.23}$$

$$\phi = \frac{\Delta_{FL} - \Delta_{FR}}{2t_f} + \frac{\Delta_{RL} - \Delta_{RR}}{2t_r} - \frac{m_v a_y h_{cog}}{K_r} \tag{4.24}$$

where K_p and K_r are pitch and roll stiffness, respectively.

Neglecting nonlinear terms, Equation 4.26 and 3.4 can be used to obtain pitch and roll rates

$$\ddot{\phi} = -\frac{t_f}{2I_{xx}}\left(F_z^{FR} + F_z^{RR}\right) + \frac{t_r}{2I_{xx}}\left(F_z^{FL} + F_z^{RL}\right) \tag{4.25}$$

$$\ddot{\theta} = -\frac{l_f}{I_{yy}}\left(F_z^{FL} + F_z^{FR}\right) + \frac{l_r}{I_{yy}}\left(F_z^{RL} + F_z^{RR}\right) \tag{4.26}$$

Following linear representation of the vertical tire forces is presented by neglecting coupling effect between pitch and roll motion [77]:

$$\begin{cases} F_z^{FL} = m_v g\dfrac{l_r}{2L} - m_v\dfrac{h_c}{2L}a_x - m_v\dfrac{h_c l_r}{t_f L}a_y \\ F_z^{FR} = m_v g\dfrac{l_r}{2L} - m_v\dfrac{h_c}{2L}a_x + m_v\dfrac{h_c l_r}{t_f L}a_y \\ F_z^{RL} = m_v g\dfrac{l_f}{2L} + m_v\dfrac{h_c}{2L}a_x - m_v\dfrac{h_c l_f}{t_r L}a_y \\ F_z^{RR} = m_v g\dfrac{l_f}{2L} + m_v\dfrac{h_c}{2L}a_x + m_v\dfrac{h_c l_f}{t_r L}a_y \end{cases} \tag{4.27}$$

Differentiating 4.27 yields:

$$\begin{cases} \dot{F}_z^{FL} = -m_v\dfrac{h_c}{2L}\dot{a}_x - m_v\dfrac{h_c l_r}{t_f L}\dot{a}_y \\ \dot{F}_z^{FR} = -m_v\dfrac{h_c}{2L}\dot{a}_x + m_v\dfrac{h_c l_r}{t_f L}\dot{a}_y \\ \dot{F}_z^{RL} = m_v\dfrac{h_c}{2L}\dot{a}_x - m_v\dfrac{h_c l_f}{t_f L}\dot{a}_y \\ \dot{F}_z^{RR} = m_v\dfrac{h_c}{2L}\dot{a}_x + m_v\dfrac{h_c l_f}{t_f L}\dot{a}_y \end{cases} \tag{4.28}$$

Summarizing vehicle pitch and roll dynamics and dynamics of the vertical tire force provides following discrete state space representation of the system:

$$\begin{cases} a_{x,k+1} = a_{x,k} \\ a_{y,k+1} = a_{y,k} \\ \dot{\phi}_{k+1} = \dot{\phi}_k + T_s \left[-\dfrac{t_f}{2I_{xx}} \left(F_z^{FR} + F_z^{RR} \right) + \dfrac{t_r}{2I_{xx}} \left(F_{z,k+1}^{FL} + F_z^{RL} \right) \right] \\ \dot{\theta}_{k+1} = \dot{\theta}_{k+1} + T_s \left[-\dfrac{l_f}{I_{yy}} \left(F_z^{FL} + F_z^{FR} \right) + \dfrac{l_r}{I_{yy}} \left(F_z^{RL} + F_z^{RR} \right) \right] \\ \dot{F}_{z,k+1}^{FL} = \dot{F}_{z,k}^{FL} + T_s \left[-m_v \dfrac{h_c}{2L} \dot{a}_x - m_v \dfrac{h_c l_r}{t_f L} \dot{a}_y \right] \\ \dot{F}_{z,k+1}^{FR} = \dot{F}_{z,k}^{FR} + T_s \left[-m_v \dfrac{h_c}{2L} \dot{a}_x + m_v \dfrac{h_c l_r}{t_f L} \dot{a}_y \right] \\ \dot{F}_{z,k+1}^{RL} = \dot{F}_{z,k}^{RL} + T_s \left[m_v \dfrac{h_c}{2L} \dot{a}_x - m_v \dfrac{h_c l_f}{t_f L} \dot{a}_y \right] \\ \dot{F}_{z,k+1}^{RR} = \dot{F}_{z,k}^{RR} + T_s \left[m_v \dfrac{h_c}{2L} \dot{a}_x + m_v \dfrac{h_c l_f}{t_f L} \dot{a}_y \right] \end{cases} \tag{4.29}$$

In Equation 4.29, longitudinal and lateral vehicle acceleration are considered as the random walk process. Therefore, these states and their derivatives are included to the state vector:

$$X = \begin{bmatrix} F_z^{FL} & F_z^{FR} & F_z^{RL} & F_z^{RR} & a_x & \dot{a}_x & a_y & \dot{a}_y \end{bmatrix}^T \tag{4.30}$$

In output vector, estimated pitch and roll rate, measured longitudinal and lateral accelerations, as well as information about total vehicle weight, are included:

$$Y = \begin{bmatrix} \dot{\theta} & \dot{\phi} & a_x & a_y & m_v g \end{bmatrix}^T \tag{4.31}$$

From the formulation of the vertical tire forces observer, it can be seen that installation of the suspension travel sensors is necessary. Therefore, this method can be used for the vehicles with semi-active or active suspension system, which is usually supplemented with this kind of sensors.

Developed vehicle state and parameter estimator is further utilized to provide necessary information to the brake control system described in the next section.

4.4 Brake system control

4.4.1 Base brake controller

The base brake control is responsible for the service braking functions with possible interaction with ABS or ESP systems [106]. It includes generation of the torque demand according to the brake pedal position and distribution of the torque demand between the wheels. Relation between the brake pedal and overall torque demand T_{bb} is described as follows:

$$T_{bb} = m_v r_w a_x^*(s_{bp}), \tag{4.32}$$

where m_v is the overall vehicle mass, r_w is the effective tire radius, a_x^* is the required longitudinal deceleration, s_{bp} is the brake pedal travel.

The relation between the brake pedal travel s_{brk} and demanded vehicle deceleration a_x^{dem} is represented as nonlinear function. Selection of such characteristics depends on the customers preferences and tuned according to the wish of target users. Valuable contribution to investigation of this topic in relation to the vehicles with decoupled brake system architecture was done by the Automotive Engineering Group at Technische Universität Ilmenau in [107, 108].

The base brake torque is further distributed taking into account regulations [109]. In this research, constant brake torque distribution was used considering specifications of the vehicle brake system and utilizes methodology described in [110].

4.4.2 Brake blending

In presence of two different brake actuators at one wheel, distribution of wheel torque demand should be performed according to the formulated control targets. In this research, priority was given to the regenerative braking to check feasibility of using OBMs in WSC mode and assess their benefits over DEHB and EHB systems.

As it is shown in Figure Figure 4.6, proposed brake blending approach applies calculated motor torque constraints to the torque demand T_{dem} to derive maximally possible demand for the electric motor T_{em}^*. Remained difference between T_{em} and T_{em}^* is used as the demand to the friction brake system. Different capabilities of the OBM and DEHB lead to the need of separating of the torque demand not only by the steady-state limitations of the electric motors, but also according to the operational frequency. For this purpose, torque blending is performed also in WSC mode and considers reactive torque T_{react}. This control block applies

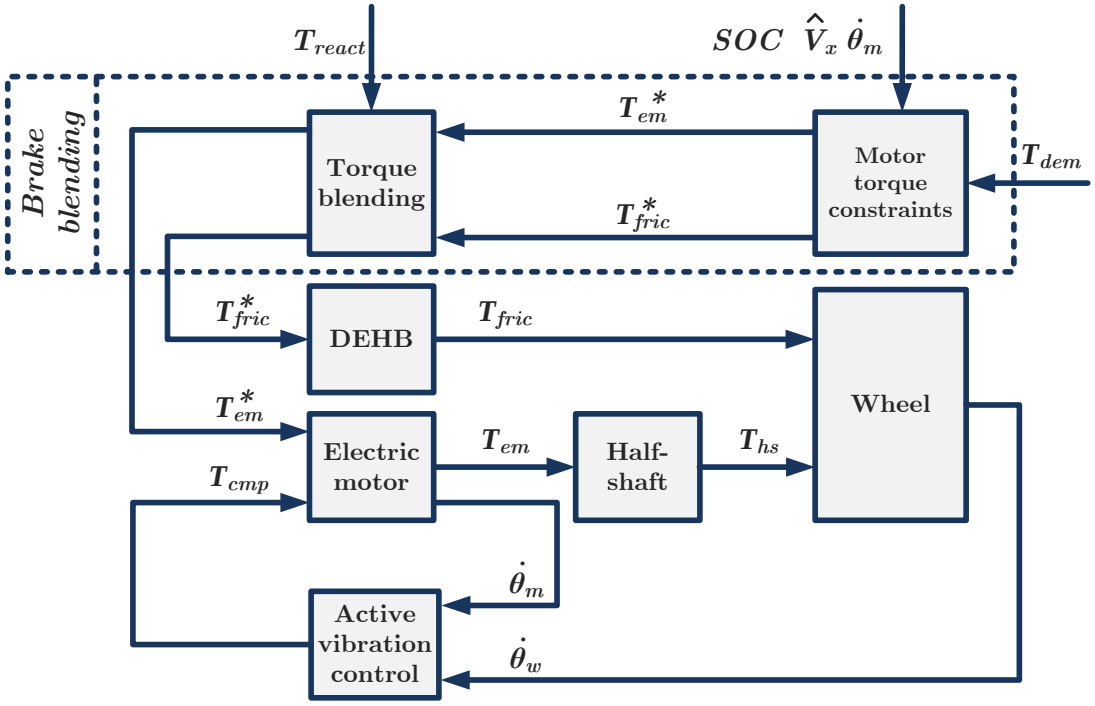

Fig. 4.6 Brake torque blending

high-frequency content of the torque demand to the electric motors, while remained torque demand is sent to the DEHB system.

This is done to use highly-dynamic electric motors also in cases, where they cannot cover T_{dem} completely. Such situation usually arises on road surfaces with high coefficient of friction. As it was presented in Section 3.3.2, powertrain half-shafts can cause oscillations of the traction or braking torque on the wheel. Such negative influence of the half-shafts torsional dynamics can be compensated by applying additional compensation torque T_{cmp}. This can be done by minimizing difference between estimated wheel and motor torques as proposed in [84]. However, this method is directly dependent on quality of wheel torque estimation. More efficient approach is based on controlling error between wheel $\dot{\theta}_w$ and electric motor $\dot{\theta}_m$ angular velocities. As proposed in [111], compensation torque is calculated as:

$$T_{cmp} = K_{AVC}(\theta_{em} - \theta_w), \tag{4.33}$$

where K_{AVC} is the control gain of active vibration control (AVC).

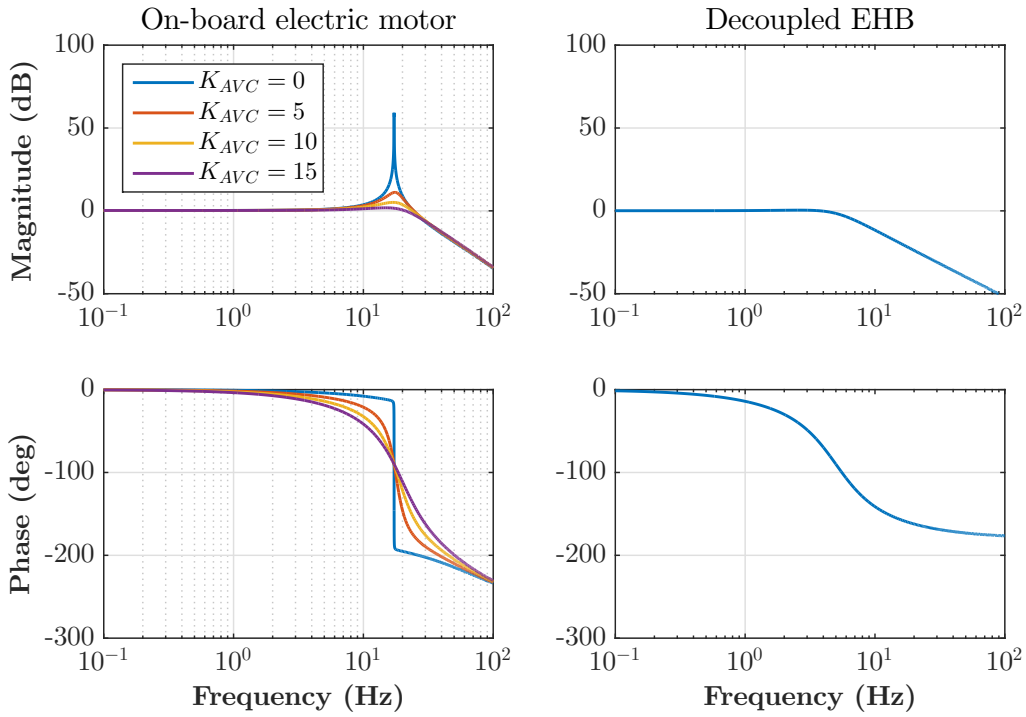

Fig. 4.7 Frequency response of the on-board electric motor and decoupled electro-hydraulic brake system

For adjustment of the AVC gain, linear model of the powertain with OBMs was derived and considered in closed-loop with AVC, see state space representation in Appendix C. As it is shown on frequency response in Figure 4.7, higher values of K_{AVC} reduce magnitude oscillations of the wheel torque. On the other hand, increase of AVC gain can cause high phase shifts. Therefore, trade-off between oscillations reduction and agility should be considered when adjusting K_{AVC}. For the given specifications of the halft-shafts (see Table 6.2), resonance of powertain system lies at 14.5 Hz, while DEHB system has bandwidth of 8 Hz, as it is shown in Figure 4.7. Therefore, proposed blending strategy, can potentially produce more accurate WSC compared to DEHB. To check this hypothesis, simulation studies and experimental validation with vehicle demonstrator are done in Section 4.6.1 and 6.3, respectively.

4.4.3 Wheel slip dynamics

Quarter car model is used to analyze problematic of WSC and presented schematically in Figure 4.8. This model allows deriving mathematical representation of wheel slip dynamics,

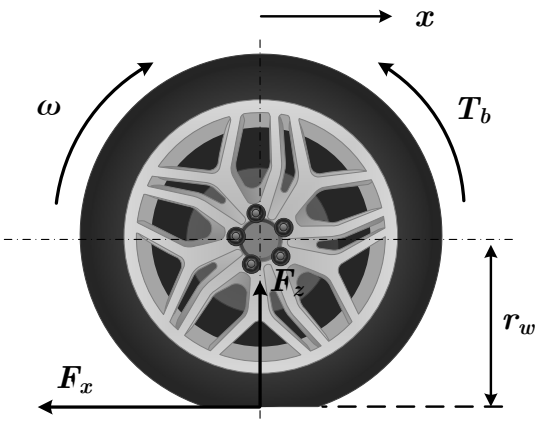

Fig. 4.8 Quarter car of longitudinal vehicle motion

which can be further used for designing WSC. Following assumptions are done in quarter car model [112]:

- Tire vertical load distribution and pitch dynamics are not explicitly presented, as the suspension dynamics are neglected and wheels are considered to be dynamically decoupled.
- The relation between longitudinal tire force and vertical load F_z is linear.
- The tire transient dynamics is neglected.
- The model covers straight-line braking cases in terms of modeling and linear analysis.
- The wheel radius is considered to be constant.

Despite these assumption, such model representation provides sufficient system description for the control design purposes. This statement was analytically confirmed in [112].

Following mathematical description of quarter car model can be obtained using equations of vehicle longitudinal motion and rotational dynamics of the wheel:

$$\begin{cases} J_w \dot{\omega}_w = r_w F_x - T_b \\ m\dot{V}_x = -F_x \end{cases} \tag{4.34}$$

where V_x is the vehicle longitudinal velocity, ω_w is the angular wheel speed, m is the mass of quarter vehicle, J_w is the wheel inertia, r_w is the wheel radius, T_b is the braking torque, F_x is the tire longitudinal force.

Neglecting tire transient dynamics, force F_x is calculated as nonlinear function of the wheel slip λ:

$$F_x = F_z \mu_{road}(\lambda), \tag{4.35}$$

where μ_{road} is the coefficient of friction between tire and road, F_z is the vertical tire force, λ is the longitudinal wheel slip.

In the braking mode the wheel slip describes relative slip velocity $V - \omega_w r_w$ normalized by vehicle velocity V:

$$\lambda = \frac{V - \omega r_w}{V}. \tag{4.36}$$

Considering $V > 0$ and $\omega \geq 0$, from Equations (4.34 - 4.36), wheel slip dynamics can be derived as follows:

$$\dot{\lambda} = -\frac{1}{V_x}(\frac{1}{m}(1-\lambda) + \frac{r_w^2}{J_w})F_z\mu(\lambda) + \frac{r}{J_w V_x}T_b. \tag{4.37}$$

It is evident that with $V \to 0$ dynamics of the system becomes infinitely fast leading to the loss of controlability. Due to this fact, wheel slip control should be switched off at averagely low vehicle velocity.

Applying Taylor expansion to Equation (4.39) linearized model with equilibrium point at λ^* and T_b^*, where λ^* is the reference wheel slip, is obtained:

$$\dot{\lambda} = -\frac{F_z(\frac{1}{m}(1-\lambda^* + \frac{r_w^2}{J_w}))\frac{\partial \mu_{road}}{\partial \lambda}(\lambda^*) + F_z\frac{1}{m}\mu_{road}(\lambda^*)}{V}(\frac{1}{m}(1-\lambda^*) + \frac{r_w^2}{J_w})F_z\mu(\lambda^*)(\lambda - \lambda^*) + \frac{r}{JV}(T_b - T_b^*) + h.o.t. \tag{4.38}$$

Transfer function from braking torque $T_b - T_b^*$ to wheel slip $\lambda - \lambda^*$ is derived accordingly:

$$H(s) = C(sI - A)^{-1}B = \frac{r}{JV}\frac{1}{s + \frac{F_z}{mV}[\frac{\partial \mu}{\partial \lambda}((1-\lambda^*) + \frac{mr_w^2}{J}) - \mu(\lambda^*)]} \tag{4.39}$$

where λ^* and T_b^* correspond to equilibrium point.

Obtained transfer function allows performing linear analysis of the open-loop system. Frequency response between output λ and input T_b states shows sensitivity analysis of the system in relation to the vehicle velocity and tire vertical load, see Figure 4.9. Tire-related parameters were taken from previously validated tire model (see Section 3.3.3); high road friction conditions and wheel slip at the optimal point were considered. As it can be seen,

increasing vehicle velocity produces higher phase shift and reduces system magnitude from relatively low to higher frequencies. This should be considered during the design stage of the WSC to provide predictable system behavior and enhance robustness in relation to the vehicle velocity. This might be done either by application of the robust control approaches [113] or by scheduling of the control control gains as the function of V_x [114]. Influence of the tire vertical load variation occurs in lower actuation frequencies below 1 Hz. Lower phase shift in this case occurs for the higher values of the vertical tire load. This is very similar to the influence of the road coefficient of friction, which produces higher phase shifts at lower values of coefficient of friction and affects system response in low frequencies. Authors in [114] recommend to apply integral action to compensate such model uncertainties. Considering difference in static load distribution, as well as dynamic distribution during the braking, separate tuning of control gains for the front and rear wheels is proposed in this research.

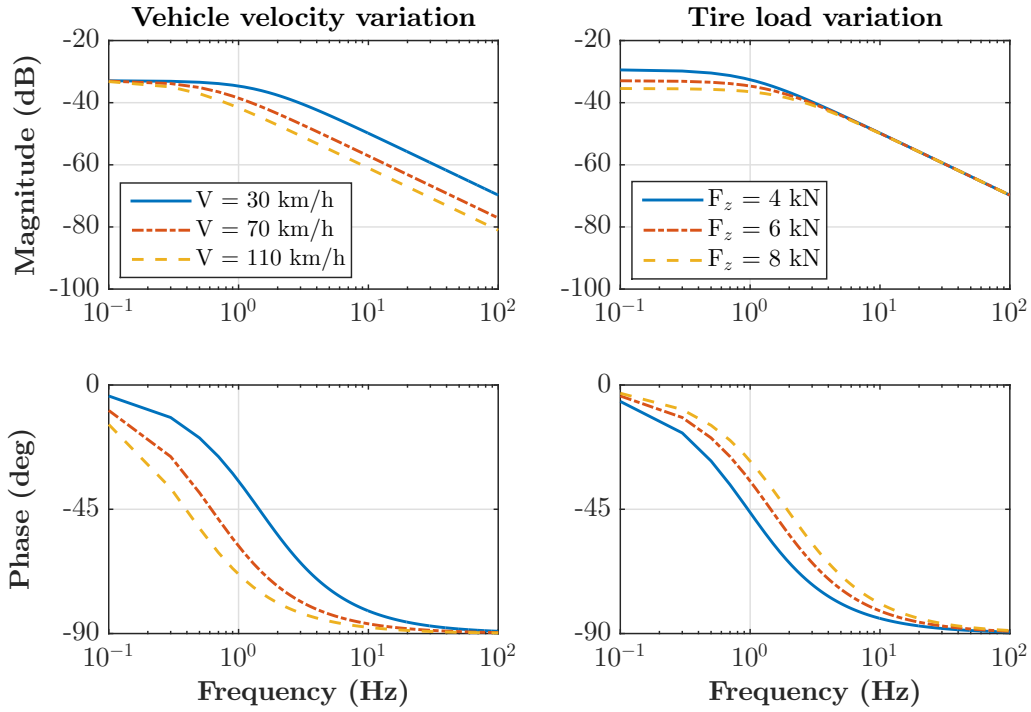

Fig. 4.9 Frequency response of the wheel slip in relation to the vehicle velocity and tire vertical load

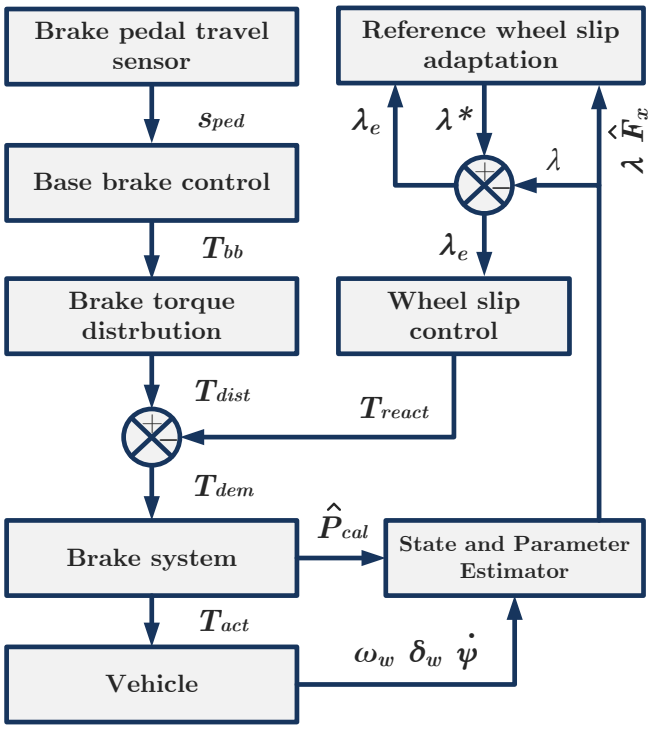

Fig. 4.10 Principle scheme of the developed wheel slip controller for SUV

4.4.4 Wheel slip control for SUV

On the basis of performed analysis of system dynamics overall control scheme of the wheel slip control was proposed and presented in Figure 4.10. It is aimed at the reduction of the error between actual λ and reference λ^* wheel slip. Purpose of the WSC is to control this deviation by calculated reactive torque T_{react}. This torque is subtracted from the torque generated by the base-brake controller and brake forces distribution (see Section 4.4.1):

$$T_{dem}^{ij} = T_{dist}^{ij} - T_{react}^{ij}, \tag{4.40}$$

where T_{dist}^{ij} is the individual wheel torque demand allocated by the base-brake controller.

As it was previously mentioned, designed control law should provide smooth tracking of the wheel slip and system robustness to states and parameter variation. To fulfill these requirements, several control laws are proposed and formulated further.

PI control with anti-windup action. The PI controller is used without D-part to reduce sensitivity of the control signal from measurement noise and avoid oscillatory WSC behavior, as a consequence. From the theoretical point of view, the PI controller improves the steady-error by one order, but on the other hand it makes response to be quite slow. Nevertheless,

properly tuned PI control still can provide quite good response to the variation of the road surface as it was confirmed by author in [115].

The wheel slip control is based on the control error derived as

$$\lambda_e(t) = \begin{cases} \lambda(t) - \lambda^*(t), & \text{if } \lambda < \lambda^* \\ 0, & otherwise \end{cases}, \tag{4.41}$$

where λ and λ^* are the actual and reference values of the wheel slip.

It can be observed that the error is equal to zero if absolute value of the wheel slip is lower than the reference. This allows to solve an issue with fault activation of the wheel slip control, where application of maximal braking force is not requested.

$$u_{pi} = K_p\left(\hat{V}_x\right)\left(\lambda_e + \frac{\int \lambda_e dt}{t_i\left(\hat{V}_x\right)}\right) - u_{pi}\frac{\int \lambda_{e,lin} dt}{t_a\left(\hat{V}_x\right)}, \tag{4.42}$$

where K_p is the proportional gain, t_i is the tuning parameter related to the I-contribution, t_a is the tuning parameter of the anti-windup part. The control gain K_p and tuning parameters t_i and t_a are presented as the function of estimated longitudinal vehicle velocity $\hat{V}_x$ to produce robustness to V_x variation.

In this control formulation, anti-windup part uses negative error $\lambda_{e,lin}$ and responsible for decreasing integral contribution in cases where wheel slip comes to the linear area. This component significantly reduces complexity of the WSC activation and deactivation rules compared to known approaches like in [112]. Despite aforementioned advantages of proposed PI control with anti-windup action, this method remains sensitive to road conditions variations. This can cause undesired oscillations of wheel slip and degradation of braking force, as a consequence. Therefore, sliding mode PI control (SMPI) is further proposed to resolve this issue.

Sliding mode PI. Advantage of proposed SMPI control with double integral PI sliding surface over PI control is that the switching control guarantees system robustness to model uncertanties. Total control effort of the SMPI consists of two parts:

$$u_{sm} = u_c + u_d, \tag{4.43}$$

where u_c and u_d are the continuous and discontinuous parts.

Continuous part is considered as the PI control from (4.42). For the situations where $\lambda > \lambda^*$, continuous part is determined by

$$u_c = \frac{1}{B} K_P \left(\lambda_e + \frac{1}{t_I}\int \lambda_e dt\right) \tag{4.44}$$

Input matrix $B(x)$ is defined as

$$B = \frac{1}{V_x}\frac{r_w}{J_w}. \tag{4.45}$$

Discontinuous control part in SMPI is formulated as

$$u_d = \frac{1}{B}K_{sw}sign(s), \tag{4.46}$$

where K_{sw} is the control gain, s is the sliding surface.

Considering control law of continuous control part, double integral sliding surface is used:

$$s = \lambda_e + K_1\int \lambda_e dt + K_2\int\left(\int \lambda_e(\tau)dt\right)dt, \tag{4.47}$$

where K_1 and K_2 are the positive constants.

Equation 4.39 can be reduced to

$$\dot{\lambda} = -\frac{1}{V_x}\frac{r_w^2}{J_w}F_z\mu_{road}(\lambda) + \frac{r_w}{J_wV_x}T_b, \quad \text{as } \frac{1}{m}(1-\lambda) \ll \frac{r_w^2}{J_w}. \tag{4.48}$$

Using this assumption and input matrix B from Equation 4.45, following is obtained:

$$\dot{\lambda} = -Br_wF_z\mu_{road}(\lambda) + BT_b + BT_{b,unc}, \tag{4.49}$$

where $T_{b,unc}$ is the braking torque describing brake system uncertainties.

As it can be seen in Equation 4.48, tire-road friction coefficient should be observed. From the practical point of view, rapid and reliable estimation of the friction coefficient is difficult and unreliable that can produce negative influence on the overall control performance. Therefore, to avoid negative influence of the estimation error, following components are considered as the uncertainty:

$$h(x) = -Br_wF_z\mu(\lambda) + BT_{b,unc}, \tag{4.50}$$

where $|h(x)| < h_{max}$.

Defining $K_1 = K_p$ and $K_2 = \frac{Kp}{t_i}$ and assuming slow variation of λ^*, i.e. $\dot{\lambda}^* = 0$, following can be obtained

$$\dot{s} = \dot{\lambda}_e + K_p\lambda_e + \int\frac{K_p}{t_i} = h(x) - K_{sw}sign(s). \tag{4.51}$$

Defining Lyapunov candidate as [116]

$$V = \frac{1}{2}s^2, \tag{4.52}$$

the system is assymptotically stable if

$$\dot{V} = \frac{1}{2}s\dot{s} = s(h(x) - K_{sw}sign(s_0)) < 0. \tag{4.53}$$

Therefore, the system is assymptotically stable for

$$K_{sw} > |h_{max}|. \tag{4.54}$$

Selection of the control gain K_{sw} in (4.54) is based on the simulation with the validated vehicle model and assessment of $|h_{max}|$ values. Despite SMPI provides a robust solution for the WSC, this approach can suffer from the chattering, which is typical for this class of controls. To solve this issue, ISM control is further proposed.

Integral Sliding Mode control. For ISM control, the motion equation of the system in sliding mode is of the same order as the original system [117]. ISM provides compensation and estimation of the perturbations with less chattering compared to the SMPI. In the common form the wheel slip dynamics can be expressed as the system operating under uncertainties as

$$\dot{x} = f(x) + B(x)u + h(x), \text{where} |h(x)| < h_{max}. \tag{4.55}$$

ISM control effort consists of two contributions:

$$u_{ism} = u_c + u_d. \tag{4.56}$$

The PI controller is used as the continuous part. According to the typical sliding mode, the discontinuous part has following representation:

$$u_d = -K_{ism}sign(s), \tag{4.57}$$

where K_{ism} is the control gain of the discontinuous part.

To reduce chattering and provide smooth control action, the discontinuous control is filtered. A first order linear filter should be tuned so that it does not distort the slow component of the switched action [116]:

$$u_d = \dot{u}_d^{filt}\tau_{sw} + u_d^{filt}. \tag{4.58}$$

Time constant τ_{sw} should be selected so small that the linear filter does not deteriorate the slow component of the switching action.

The sliding surface consists of the two parts and defined as

$$s = s_0 + z_{ism}, \tag{4.59}$$

where z_{ism} is the integral term, $s_0 = \lambda - \lambda^*$ is the sliding variable as in conventional sliding mode.

Subtracting derivative of the reference wheel slip from the left and right sides of (4.48) yields:

$$\Delta\dot{\lambda} = \dot{\lambda} - \dot{\lambda}^* = -\dot{\lambda}^* - B(x)r_w F_z \mu(\lambda) + B(x)u + B(x)T_{w,unc}, \tag{4.60}$$

where the reference wheel slip λ^* is considered as the known variable and $f(x) = \lambda^*$, the additional wheel torque $T_{w,unc}$ describes uncertainties. The uncertainty is defined as in the case of SMPI control in (4.50).

Using previous equations, the auxiliary variable z_{ism} equals to

$$\dot{z}_{ism} = -\frac{\partial s_0}{\partial(\lambda - \lambda^*)}(-\dot{\lambda}^* + B(x)(u_{ism} - u_d)) = \dot{\lambda}^* - B(x)(u - u_d). \tag{4.61}$$

The time derivative of the Lyapunov function should be negative to guarantee asymptotically stable system. Since

$$\begin{aligned} \dot{s} = s_0 + z_{ism} = \dot{\lambda} - \dot{\lambda}^* + \dot{\lambda}^* - B(x)(u - u_d) = \\ h(x) + B(x)u_{ism} - B(x)(u_{ism} - u_d) = h(x) - u_d = \\ h(x) + B(x)u_d = h(x) - B(x)K_{ism}sign(s) \end{aligned} \tag{4.62}$$

following inequality

$$\dot{V} = \frac{1}{2}s\dot{s} = s(h(x) - K_{ism}sign(s)) < 0 \tag{4.63}$$

is satisfied for

$$K_{ism} > \left|\frac{h_{max}}{B(x)}\right|. \tag{4.64}$$

Similar to the SMPI control, K_{ism} is selected using simulation results with experimentally validated vehicle model.

Aforementioned control methods are evaluated and used for benchmarking in software-in-the-loop simulations, hardware-in-the-loop experiments and in tests with SUV vehicle demonstrators. To explore advantages of using variable structure and sliding mode methods,

three other methods are further introduced. Due to the fact that some of the control approaches are applicable only to the actuators with high operational frequency, evaluation and comparison of first-order sliding mode, variable structure PI control and continuous twisting algorithm will be applied to the vehicle with four individual in-wheel motors (IWM).

4.4.5 Wheel slip control for vehicle with IWMs

Compared to the WSC for SUV demonstrator, proposed WSC architecture for vehicle with IWMs uses principle of direct slip control. Instead of reactive wheel torque T_{react}, such WSC generates electric motor torque demand T_{em}^{*} necessary for maintaining desired wheel slip λ^{*}, see Figure 4.11. Therefore, this approach is applicable not only to ABS, but also for VSC purposes. However, this requires additional activation logic for the ABS mode. In presented study, ABS activates individually for each wheel when wheel slip λ is higher than reference λ^{*}. Deactivation happens if torque demand from distribution function is lower than the torque from WSC. Under this conditions, WSC or distributed torque demand are bypassed to the low-level electric motor controller. Considering that this part of study has an aim of comparing VSS and SMC methods, reference wheel slip value is fixed at the value close to the optimum. Despite this fact, architecture of the controller was designed in such a way that it can be easily extended by reference wheel slip adaptation.

Variable structure PI control. Research in the area of variable structure control was initiated in the late fifties in the former Soviet Union [118]. This control approach proposes attractive tool for the system with variable or switchable system dynamics {utkin2002first. Application of this methodology to WSC can provide benefits in terms of system robustness and control accuracy. This is determined by the fact that braking force and wheel slip dynamics have considerable difference in the stable and unstable area of force-wheel slip diagram. This problem can be solved, as proposed in PI control with anti-windup action. However, this method can be applied only to ABS control. To produce more unified approach, applicable also to VSC systems, variable structure PI (VSPI) is introduced. This uses simple PI control representation with additional switching logic and provided with preliminary tuning method. Similar to the previously introduced WSC methods, control error is expressed as the difference between reference wheel slip λ^{*} and its actual value λ:

$$\lambda_e = \lambda - \lambda^{*}. \tag{4.65}$$

PI control law for driving the control error λ_e and holding this error at the origin during emergency braking is presented as follows:

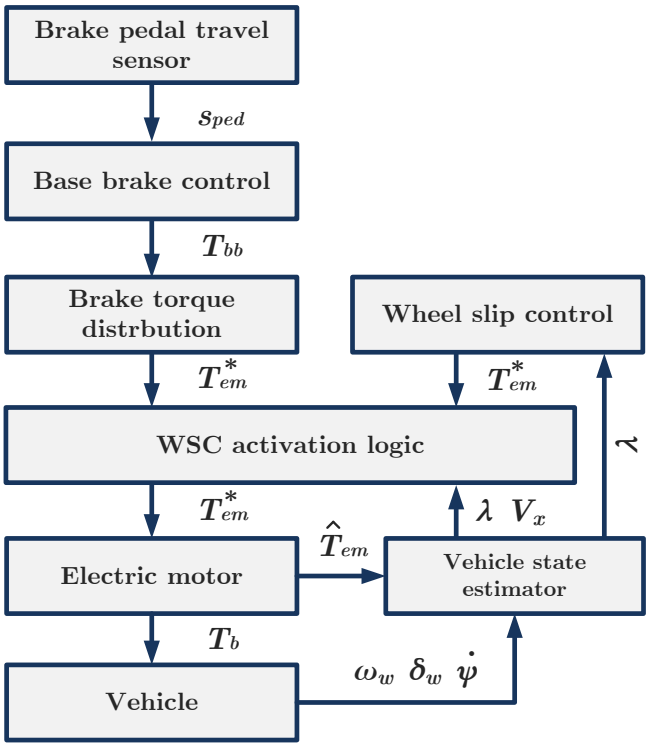

Fig. 4.11 Principle scheme of the developed wheel slip controller for vehicle with IWMs

$$T_{em} = K_p \left(\lambda_e + \frac{1}{t_a} \int \lambda_e \right) \tag{4.66}$$

Assuming constant wheel slip reference $\lambda^* = 0$ and replacing T_{em} in Equation 4.39 with PI control law and considering $\vartheta_2 = \lambda$, following closed-loop representation of the system can be derived:

$$\begin{cases} \dot{\vartheta}_1 = \vartheta_2 \\ \dot{\vartheta}_2 = -\frac{\lambda^* F_x}{m V_x} + \frac{(\vartheta_2 - 1) F_x}{V_x m} - \frac{r_w^2 F_x}{J_w V_x} + \frac{r_w}{J_w V_x} K_p \left(\vartheta_2 + \frac{1}{t_a} \vartheta_1 \right) \end{cases} \tag{4.67}$$

Dividing the second by the first equation, state trajectories can be presented by

$$\frac{d\vartheta_2}{d\vartheta_1} = -\frac{\lambda^* F_x}{m V_x \vartheta_2} + \frac{(\vartheta_2 - 1) F_x}{m V_x \vartheta_2} - \frac{r_w^2 F_x}{J_w V_x \vartheta_2} + \frac{r_w}{J_w V_x} K_p \left(1 + \frac{\vartheta_1}{t_a \vartheta_2} \right) \tag{4.68}$$

To calculate longitudinal tire force F_x, nonlinear steady-state tire model is used. Obtained state trajectories of this closed-loop system allows designing control law for WSC. As it can be seen on the left of Figure 4.12, constant gains of PI control produce not only inefficient solution in terms of brake force, but can also produce traction torque by electric motors.

Considering these issues, VSPI control can be adjusted to have quicker dynamics in unstable area (higher P contribution and lower I), while slower control action should be produced in stable are (lower P contribution and higher I). Therefore, switching between control gains is proposed to be done when wheel slip passes reference value λ^*:

$$K_p = \begin{cases} K_{p1}, & \text{if } \lambda < \lambda^* \\ K_{p2}, & otherwise \end{cases}, \tag{4.69}$$

$$t_a = \begin{cases} t_{a1}, & \text{if } \lambda < \lambda^* \\ t_{a2}, & otherwise \end{cases}. \tag{4.70}$$

Resulting system behavior is presented on the phase plane in middle of Figure 4.12. As it can be seen, the system is driven to the origin with higher wheel slip rate in the area over optimal slip to avoid wheel lock. In the same time, proposed control holds wheel slip close to the optimum when lies under the reference.

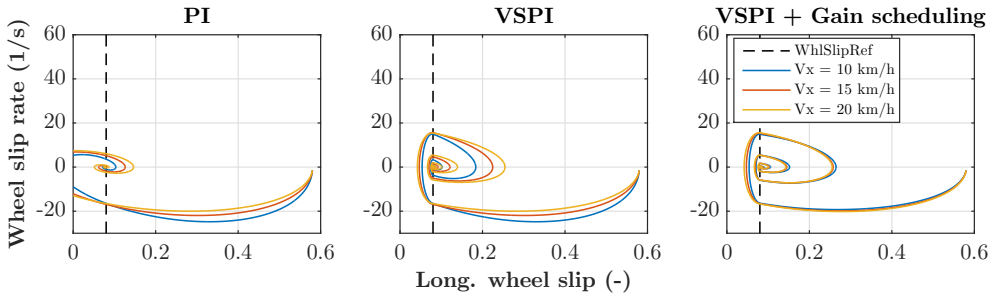

Fig. 4.12 State trajectories of wheel slip dynamics with PI and VSPI WSC: PI control without switching logic (left) switching gains at reference wheel slip (left) and gain scheduling of PI gain in stable and unstable areas (right)

As it was previously shown in on wheel slip frequency response in Figure 4.9 and as it depicted in system trajectories in Figure 4.12, dynamics of the system varies with variation of vehicle velocity. Therefore, gain scheduling of P and I gains of VSPI control should be performed to achieve predictable system response. Right side of Figure 4.12 presents system trajectories after preliminary setting of the control gains scheduled according to the vehicle velocity variation. This provides predictable system behavior for different vehicle velocities and allows to shape gain scheduling curves for K_p and t_a before experiments.

First-order sliding mode control. First-order sliding mode (FOSM) control is nonlinear control method, which forces the system to slide over designed sliding manifold. This method is known by its robustness; however, use of the discrete control part leads to chattering in control signal. Due to this fact, this method was usually applied only in simulation studies

for WSC design, as can cause damaging of mechanical components. Therefore, this method was used for the vehicle with individual IWMs with relatively high system bandwidth and absence of mechanical transmission.

Sliding variable in designed FOSM is defined in the same way as the control error:

$$s = \lambda_e = \lambda - \lambda^* \tag{4.71}$$

The control law for FOSM approach for the system in Equation 4.49 can be defined as

$$T_{em} = -K_{fosm} sign(s), \tag{4.72}$$

where K_{fosm} is a positive constant.

Presenting Equation 4.73 as

$$\dot{\lambda} = B(-r_w F_z \mu_{road}(\lambda) + T_{em} + T_{b,unc}), \tag{4.73}$$

system uncertainty $h(x)$ is determined by

$$h(x) = -r_w F_z \mu_{road}(\lambda) + T_{b,unc} \tag{4.74}$$

Considering Equations 4.73 and 4.75 and referring to [119], following inequality should be satisfied:

$$K_{fosm} \geqslant |h_{max}|. \tag{4.75}$$

One of the main disadvantages of FOSM is presence of chattering, which is critical for mechanical systems. To solve this issue, *sign* function can be replaced with its following approximation [120]:

$$\hat{sign}[x(t)] = \frac{x(t)}{|x(t)| + \varepsilon} \tag{4.76}$$

with reasonably small value of $\varepsilon > 0$. Higher values of ε however can follow to the loss of control performance which is characterized by occurrence of static error in presence of matched disturbances [121].

Although application of FOSM as the WSC is known from various literature sources, this control technique was not tested on the vehicles due to the issues with chattering. Despite this disadvantage of FOSM, feasibility study for IWMs with relatively high system bandwidth was done and compared to ISM, VSPI and CTA control techniques.

Continuous twisting algorithm. Continuous twisting algorithm (CTA) relates to the sliding mode control methods and known by its benefits in terms of disturbances compensation and solving of chattering issue [122]. These advantages of the method motivated its application for the WSC system, which has similar design requirements: providing smooth wheel slip tracking and robustness to disturbances. This control technique produces third-order sliding mode in relation system state. Hence, this method cannot be naturally applied to the considered system. As the solution, system order can be auxiliary increased. According to definition of relative degree of freedom ρ [123], this corresponds to the minimum order of the time derivative of sliding variable s^{ρ}, where control input T_{em} explicitly appears [124]. Computing first and second derivative of the sliding variable, following representation of the system is obtained:

$$\begin{cases} \dot{s} = -\dfrac{1}{V_x}\dfrac{r_w^2}{J_w}F_x + \dfrac{r_w}{J_w V_x}T_{em} \\ \ddot{s} = \ddot{\lambda}^* - \dfrac{r_w^2 \dot{F}_x}{J_w V_x} + \dfrac{r_w^2 F_x \dot{V}_x}{J_w V_x^2} - \dfrac{\dot{F}_x r_w \omega}{m V_x^2} - \dfrac{F_x r_w \dot{\omega}}{m V_x^2} + \dfrac{2F_x r_w \omega \dot{V}_x}{m V_x^3} \\ \quad - \dfrac{r_w \dot{V}_x}{J_w V_x^2}T_{em} + \dfrac{r_w}{J_w V_x}\dot{T}_{em} \end{cases} \tag{4.77}$$

Right hand side of the second equation in this system includes several components, which cannot be estimated in reliable way. Hence, it is proposed to consider them as the system disturbance $w(t)$. Considering this fact, this auxiliary system can be presented in general form as

$$\begin{cases} \dot{\zeta}_1(t) = \zeta_2(t) \\ \dot{\zeta}_2(t) = w(t) + g(t)\,\nu(t) \end{cases} \tag{4.78}$$

Presented system has two auxiliary states $\zeta_1 = s$ and $\zeta_2 = \dot{s}$ and ν represents auxiliary control input. Therefore, control effort T_{em} is expressed as the integral of the auxiliary control input, which provides continuous control input:

$$T_{em} = \int_{\tau_1}^{\tau_2} \nu(t)\,. \tag{4.79}$$

After obtaining this system description, control problem can be formulated. This is concluded in driving the state ζ (which is equal to the wheel slip error λ_e) to the origin despite disturbances which affecting the system. To solve this problem, aforementioned CTA can be applied as in [122]:

$$\begin{cases} \nu(\zeta) = -K_{cta,1}\lceil\zeta_1\rfloor^{\frac{1}{3}} - K_{cta,2}\lceil\zeta_2\rfloor^{\frac{1}{2}} + \eta \\ \dot{\eta} = -K_{cta,3}\lceil\zeta_1\rfloor^{0} - K_{cta,4}\lceil\zeta_2\rfloor^{0} \end{cases} \tag{4.80}$$

where notation $\lceil\cdot\rfloor^{\gamma}$ means $sign(\cdot)|\cdot|^{\gamma}$.

To guarantee stability of CTA control strategy, offline optimization of control gains can be performed. Method, described in [122], was utilized for this purpose to confirm stability of the system.

4.5 Reference wheel slip adaptation

For the WSC control, information about the position of the optimal wheel slip is required to produce maximal tire force as requested by the driver. Such estimation techniques are mainly based on the empirical approaches in rule-based ABS systems [38]. These approaches mainly aimed at determination of the ABS thresholds, which in combination with rule-based control produces suboptimal system operation. As a consequence, this leads to longer braking distance and deteriorated ride quality, as periodic brake pressure modulation and wider reference wheel slip range induce oscillations of the wheel braking force and cause suboptimal system operation, as a consequence.

To overcome these disadvantages, reference wheel slip adaptation method is proposed. Figure 4.13 shows principle scheme presenting relevant system state observers. The reference wheel slip adaptation is based on the estimation of the longitudinal wheel slip λ and longitudinal tire force $\hat{F}_x$, as explained in Section 4.3. This allows to reconstructing F_x-λ characteristics which is further used for observation of the gradient $\frac{\partial F_x}{\partial \lambda}$. This gradient has a positive sign in the linear area of tire longitudinal characteristics, equal to zero at the extremum point and has negative sign in post-extremum area. Therefore, change of the $\frac{\partial F_x}{\partial \lambda}$ sign means that system passes the optimal wheel slip. However, even in presence of knowledge about longitudinal tire force and wheel slip, determination of the gradient sign is a challenging task due to measurement noise and transients occurring during ABS braking.

Therefore, for definition of the reference wheel slip λ^*, the gradient of $\frac{\partial \hat{F}_x}{\partial \lambda}$ is identified by fitting the polynomial. Across several approaches, where functions of different complexity where used for this purpose [125, 34], solution with the linear function is selected:

$$\hat{F}_x = C_1 + C_2\lambda, \tag{4.81}$$

where C_1 and C_2 are coefficients of the polynomial.

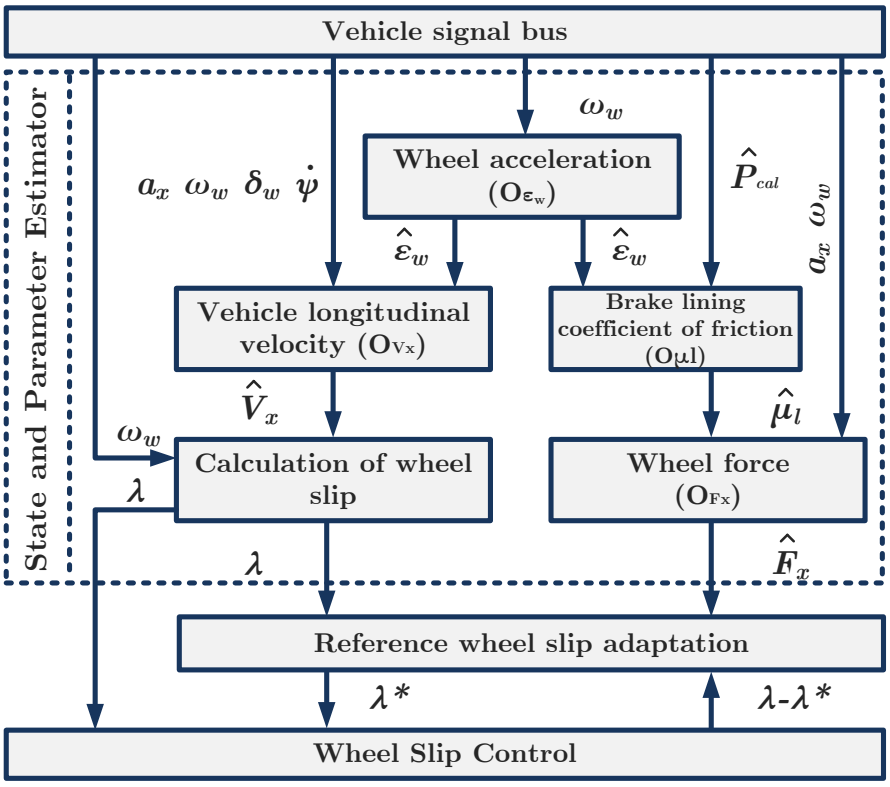

Fig. 4.13 Reference wheel slip adaptation and relevant state estimators

The polynomial is fitted then to the collected set of force $\hat{F}$ and wheel slip λ during predefined time period. These coefficients are estimated by solving the polynomial fitting task. Compared to the approaches, where nonlinear functions are fitted, this one requires linear parameter estimation procedure using RLS method:

$$y = X^T \theta, \tag{4.82}$$

where $y = \hat{F}_x$, $X = \begin{bmatrix} 1 & \lambda \end{bmatrix}^T$, $\theta = \begin{bmatrix} C_1 & C_2 \end{bmatrix}^T$.

Information about y and X is collected during the predefined time Δt, and the length of these elements is $n = \frac{\Delta t}{T_s}$. The sign of the C_2 corresponds to the sign of the gradient $\frac{\partial \hat{F}}{\partial \lambda}$. As soon as the $\frac{\partial \hat{F}}{\partial \lambda}$ gradient is obtained, initial reference set point λ^*_{init} can be determined by taking the mean value of $\begin{bmatrix} \lambda(t_1) & \dots & \lambda(t_n) \end{bmatrix}$. In this form, rapid variation of the reference wheel slip can occur, which causes oscillatory WSC behavior. Therefore, additional set of adaptation rules should be applied providing reference slip value as slowly varying parameter and omitting its variation due to the high values of control error. These rules are summarized in Procedure 1 (see Appendix A).

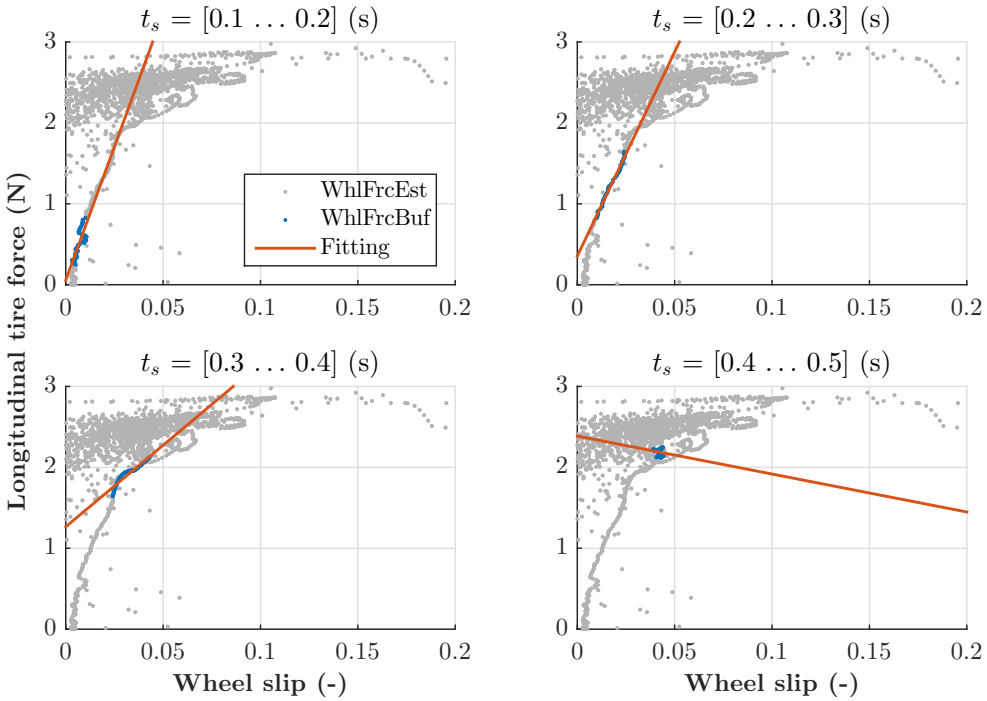

Fig. 4.14 Estimation of the wheel force - wheel slip gradient estimation

Figure 4.14 shows a graphical interpretation of the developed approach. As it can be seen, linear polynomial function is fitted to the measurements collected during 100 ms. Gradient $\frac{\partial \hat{F}_x}{\partial \lambda}$ remains positive during first three iteration. After the fourth iteration, happening after 400 ms of braking, sign of the gradient has changed to negative value, which means that optimum wheel slip value was passed during this time period. After that, WSC will be activated and adaptation Procedure 1 (see Appendix A) is applied to adapt reference wheel slip value.

4.6 Simulation results

For the better correlation between road tests and simulation, road coefficient of friction was reproduced from the real preliminary tests with the vehicle. For this purpose, maximal road coefficient of friction during the braking was determined by the methodology proposed in [126].

This data was used to determine variation range, frequency of occurrence and establishing stochastic model for road coefficient of friction. This allows to reproduce real driving conditions and check control robustness in various road conditions. Experimental data from Lommel proving ground, Alkersleben airport and Tokyo testing track were analyzed and

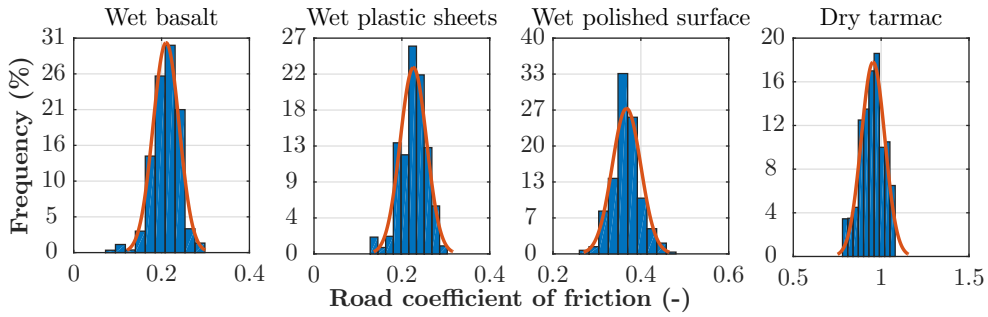

Fig. 4.15 Characterization of the road coefficient of friction

distribution of the road coefficient of friction is summarized for various road surfaces in Figure 4.15. All four surfaces have normal distribution of the road coefficient of friction. After fitting the distribution function and determining its parameters, road profiles were generated and implemented in IPG CarMaker simulation environment.

4.6.1 Wheel slip control with brake blending

The procedure includes sequence of simulations, where the reference value of the wheel slip is varied in the range from values of 0.04 to 0.25. This is done to evaluate control performance in linear, optimal and nonlinear areas of the F_x - λ diagram. This produces an overall picture of system sensitivity to variation of wheel slip setpoint and allows analyzing robustness of the controller. For evaluating PI control with brake blending between OBMs and DEHB, wet basalt and dry tarmac road surfaces were selected and correspond to real friction conditions at Lommel Proving Ground. Road coefficient of friction was modeled as shown in Figure 4.15.

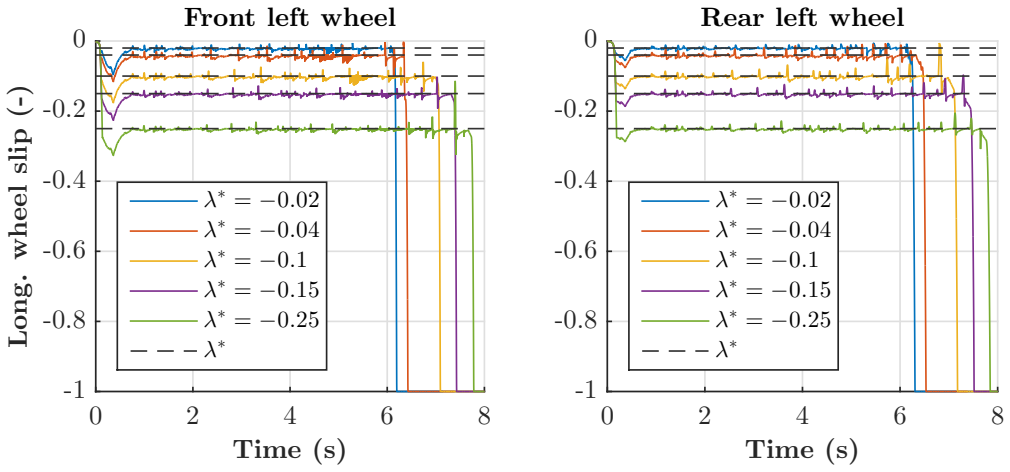

Fig. 4.16 Braking on wet basalt: PI with brake blending

Figure 4.16 presents wheel slip behavior for the driving in low friction conditions. As it can be seen, both rear and front wheels have accurate tracking of the setpoint which is possible to obtain by mainly using OBMs in WSC mode. That means that in such road conditions, OBMs can completely cover torque demand and friction brakes are activated only after reaching velocity of 20 km/h. It is also important to admit that there is no deterioration of control performance after involving DEHB at the final stage of braking. It allows to conclude that WSC was properly tuned and integrated with brake blending control algorithms.

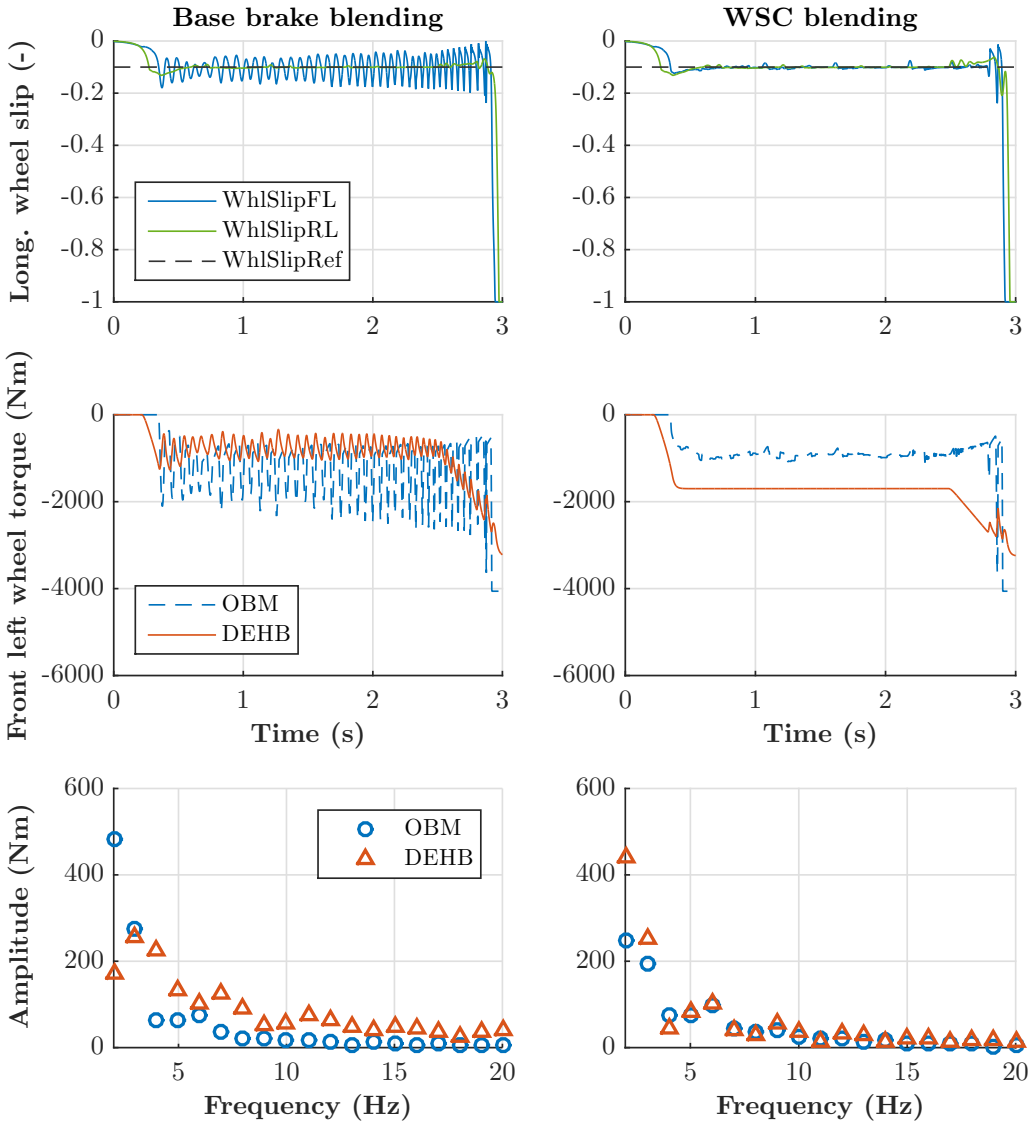

Fig. 4.17 Braking on dry tarmac: comparison of WSC blending strategies

More sophisticated situation occurs during the braking on dry tarmac. Due to OBM torque limitations, they are not able to fulfill the whole torque demand. As a consequence, DEHB should be involved already at the initial phase of braking. Important to admit that this topic is very actual nowadays and improper integration or settings of WSC and brake blending algorithms can cause longer braking distance [127]. For this purpose, main contribution (or high-frequency content, at least) should be sent to electric motors, while the rest is to be covered by friction brakes. Left side of Figure 4.18 presents the case, where this logic was not applied and only torque limitations were applied. This caused instabilities in system, which led to oscillations in wheel slip of the front wheels. It can be clearly seen on torque demand amplitude that DEHB was induced to produce torque in frequency higher than the system bandwidth, while low frequency content was covered by electric motors.

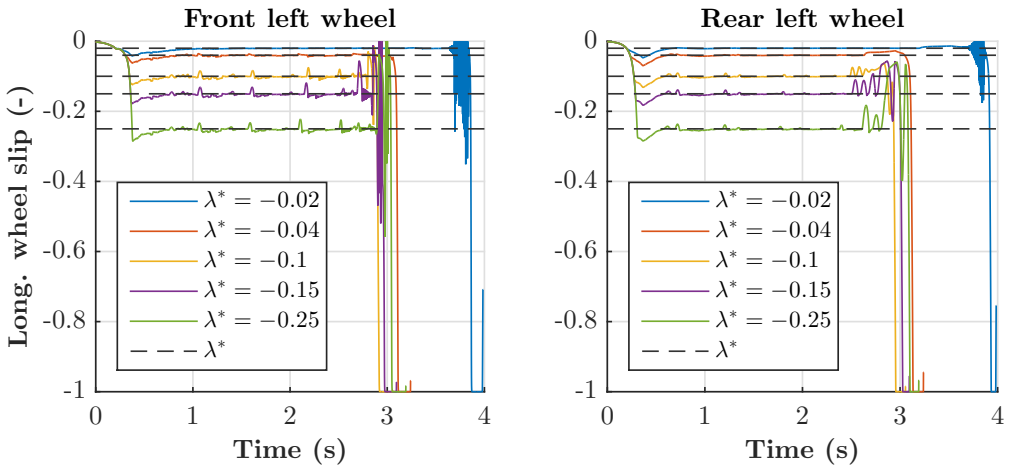

Fig. 4.18 Braking on dry tarmac: PI with brake blending

Applying control strategy, where WSC torque demand is properly split between actuators (right side of Figure 4.18), front wheels produced very precise wheel slip tracking. With this control logic, DEHB received low-frequency content of the brake torque demand, while main WSC effort is provided by electric motors. This can even more clearly seen on amplitude of torque demand, where main contribution of DEHB lies in frequencies up to 8 Hz.

To check sensitivity of this control approach under variation of reference wheel slip value, set of simulations was performed and plotted in Figure 4.18. Important to say that higher values of the reference wheel slip follow to higher brake torque demand and higher torques in DEHB system, as a consequence. Therefore, accurate and smooth tracking of the wheel slip allows confirming also robustness of the proposed integration of WSC and brake blending strategy. Having such control performance, it can be concluded that PI control with anti-windup action in linear area provides robust operation in wide range of road coefficient of friction.

Numerical results from the simulation studies were concluded in Table D.2. Besides that, for assessing possible effects from application of developed control strategies, a rule-based ABS was considered for comparison and uses main principles as in [6]. Conventional ABS approach was applied to the vehicle with DEHB system, dynamics of which is presented in Section 3.3.1. As it can be seen in low and high road friction conditions, OBMs and continuous WSC strategy produces 32 % and 15 % shorter braking distance compared to the rule-based logic. Having less oscillations in braking force, continuous WSC also provides 52 % and 65 % better ride quality by reducing vehicle jerk. These benefits were later assessed in road tests (see Section 6.3), having a serial production vehicle with rule-based ABS for fair comparison.

4.6.2 Wheel slip control with decoupled electro-hydraulic brake system

Research, performed with OBMs and DEHB, motivated further development of the WSC for DEHB systems. As soon as they have slower system dynamics and lower system bandwidth compared to OBMs, it is more competitive to obtain robust WSC operation in various road conditions. For this purpose, SMPI and ISM controls were considered and compared with PI control approach. For the tuning and validation of the developed control strategies for WSC with DEHB system, two cases simulation were considered: braking in low and high friction conditions. Variable road coefficient of friction was composed from the preliminary testing sessions in Alkersleben airport (Germany) as it is shown in Figure 4.15, which in average corresponds to values of 0.36 and 0.98, respectively.

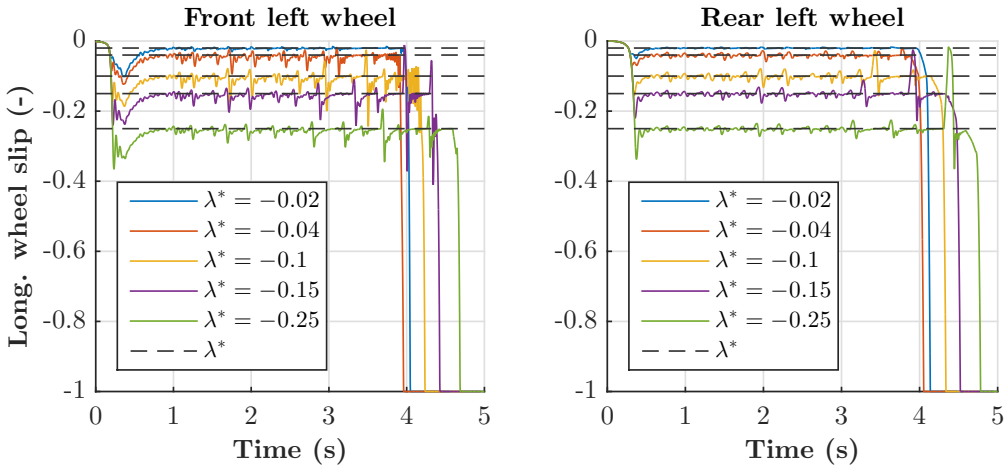

Fig. 4.19 Braking on wet polished surface: PI control

Figures 4.19-4.19 present wheel slip behavior during the braking on wet polished road surface. PI control, applied to the pure DEHB system, does not deviate very much from the results obtained for the hybrid OBM-DEHB system. Although similar system behavior, first peak in WSC is usually a bit higher than in case of electric motors due to slower system response. Nevertheless, compared to the rule-based control approach continuous PI control for DEHB allows to reduce first peak value on 74 % and 45 % for front and rear wheels, respectively, see Table E.1.

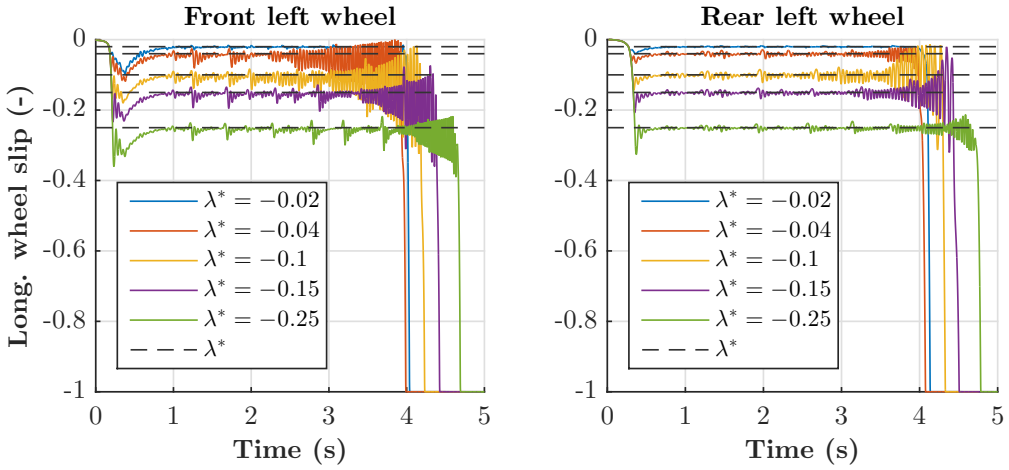

Fig. 4.20 Braking on wet polished surface: SMPI control

These road conditions usually characterized by higher frequency modes of WSC compared to the dry tarmac case. As it can be seen in Figure 4.20, discontinuous part in such road conditions produces high oscillations (chattering) around the reference value of the wheel slip. This phenomena is typical for the sliding mode approaches of lower order. Despite this disadvantage, SMPI control strategy theoretically provides robust system operation and can cope with the variation of the vertical tire force as well as with variation of the road coefficient of friction.

Containing main sliding-mode control features and producing less chattering, ISM control has similar control performance compared to the PI control. This produces smooth and accurate tracking of the reference wheel slip, see Figure 4.21. Developed control reacts on the variation of vertical tire load distribution, which allows to minimize first peak during the WSC braking.

For the simulations on dry tarmac surface, gains of all three considered control approaches were fixed at the same values as in case of braking on wet polished road surface. This was done to check robustness of WSC in respect to variation of road conditions. As it can be observed in Figure 4.22, PI control provides good tracking performance with more oscillatory

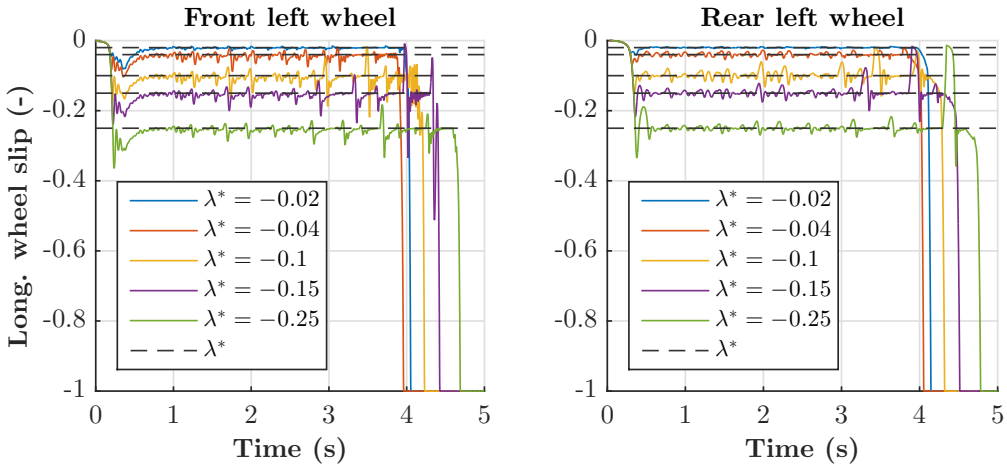

Fig. 4.21 Braking on wet polished surface: ISM control

behavior on front wheels. This effect is determined by higher load transfer and higher brake pressure demand on dry tarmac.

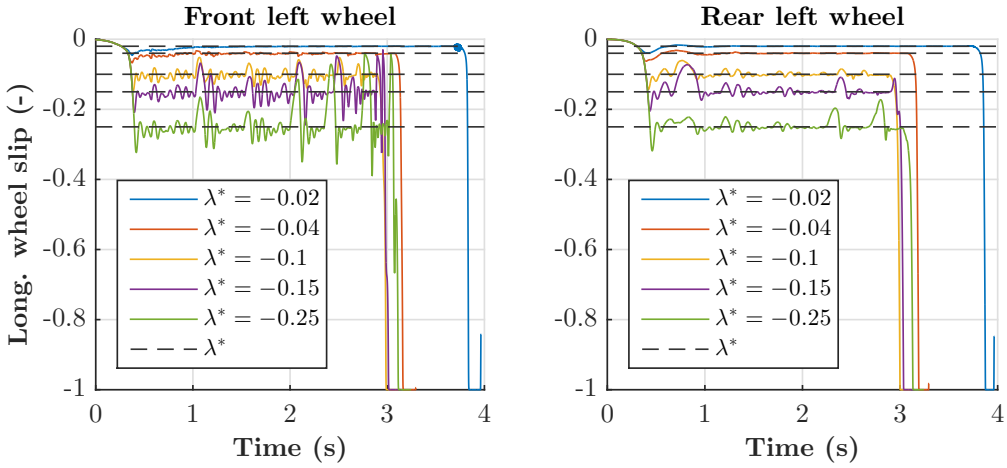

Fig. 4.22 Braking on dry tarmac: PI control

Compared to the PI control, SMPI provides smoother control of the rear wheels even in presence of variable road coefficient of friction, Figure 4.23. However, similar to the case of braking on wet polished road surface, SMPI produces chattering at lower velocities.

In Figure 4.24 deeper cycles in direction of linear area can be recognized in case of rear wheels. In general, similar happens with presented control strategies. As soon as SMPI and ISM have PI control as continuous part, anti-windup part serves for getting wheels back to the setpoint from expected linear area.

Developed control strategies have similar distribution of the control effort in frequency spectrum, as it can be observed in Figure 4.25. This can be explained by the fact that SMPI

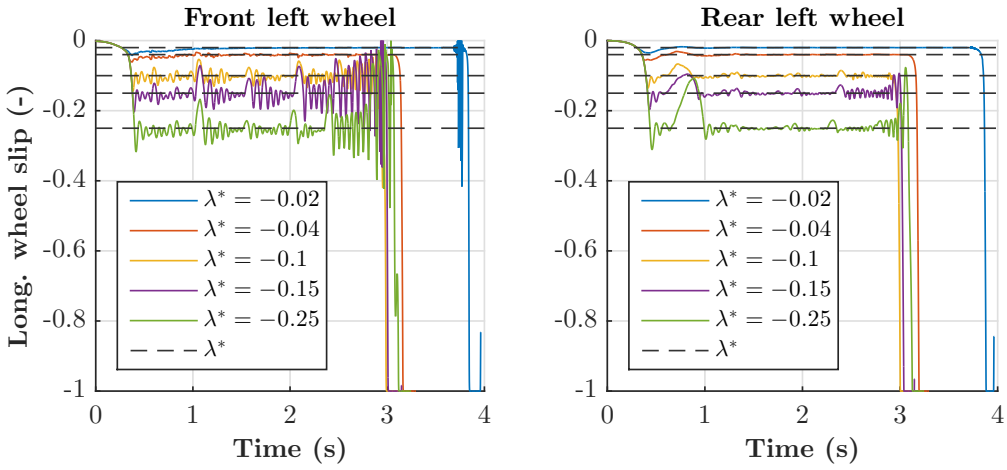

Fig. 4.23 Braking on dry tarmac: SMPI control

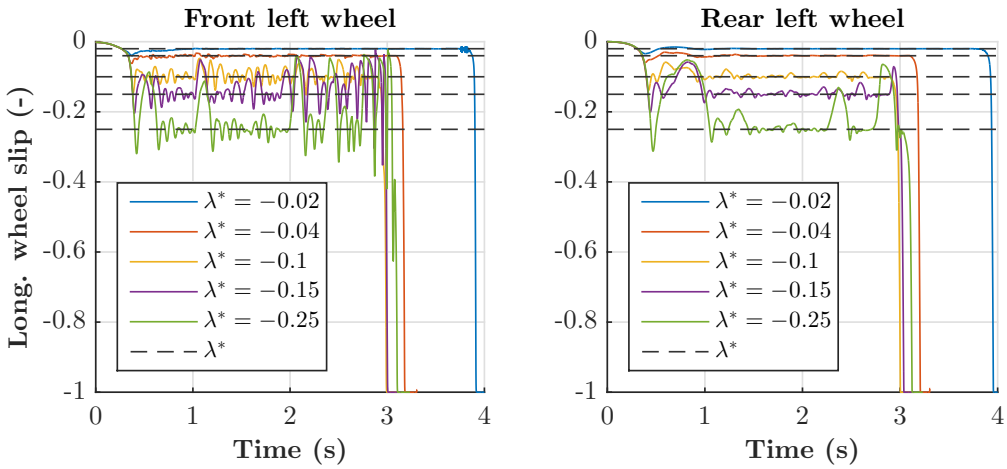

Fig. 4.24 Braking on dry tarmac: ISM control

and ISM controls have PI control as the continuous control part. However, SMPI control has slight difference in amplitude in higher frequencies, which happens due to chattering in brake pressure demand.

4.6.3 Wheel slip control with in-wheel motors

Reference value of the wheel slip was set ($\lambda^* = 0.04$) considering the road surface, tire characteristics and specifications of the measurement system and state estimation routines on the real vehicle prototype. Taking into account limitations of the testing track, braking was performed from the velocity of 30 km/h. Vehicle model parameters were adjusted according to the specification of compact vehicle demonstrator equipped with four individual IWMs. The road surface presents a composition of wet plastic sheets and road coefficient of friction

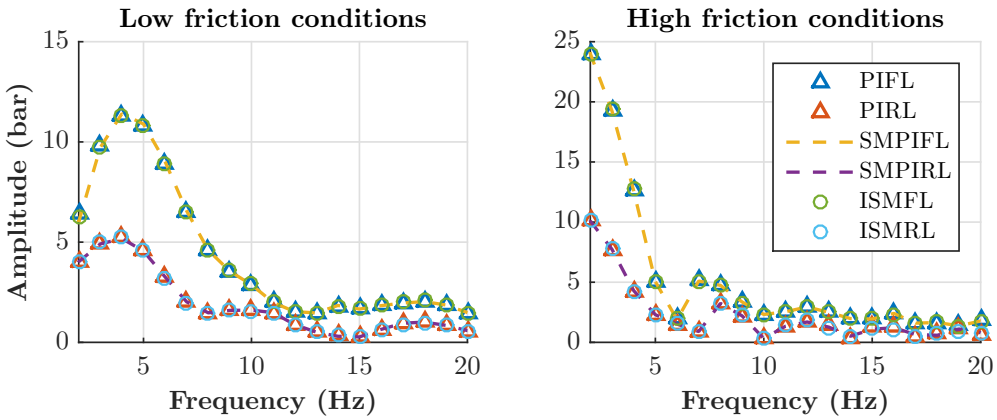

Fig. 4.25 Distribution of the brake pressure demand in frequency spectrum

has value of 0.21 in average. Simulations were performed to tune control algorithms and assess their performance not only in relation to IWMs, but also to evaluate their applicability to the other types of decoupled brake systems. For this purpose, control torque demand is presented in addition to wheel slip profiles in Figure 4.26.

FOSM control quickly reaches the reference wheel slip. In sense of agility and first WSC peak, this control provides the best behavior. However, chattering is typical for FOSM - after reaching setpoint it produces wheel torque demand with high oscillations amplitude and frequency. In general, this approach might be used for IWMs with direct torque transmission to the wheels. Nevertheless, this approach is not applicable to be used with DEHB or OBM as can follow to damages of mechanical system. Figure 4.27 shows that FOSM has high wheel torque demands in the area of 50 to 90 Hz.

Proposed VSPI strategy has similar properties as PI control with anti-windup action in linear region, presented in previous subsections. This algorithm produces the highest first peak value due to presence of integral part but in the same time provides smooth and precise tracking after reaching the setpoint. Important to admit that such WSC is possible even in presence of inhomogenous road surface and with relatively low value of the reference wheel slip. Such control performance is possible by proper tuning of control gains for linear and nonlinear regions of F_x - λ diagram.

First peak as well as oscillations around setpoit were eliminated by applying ISM control. Important to admit that low-pass filter in discontinuous control action of ISM had higher cutoff frequency than for DEHB system from previous subsection. This is applicable in case of IWMs, which have relatively quick system response and wider system bandwidth. This leads to some slight chattering in terms of wheel torque demand which can be covered by IWMs.

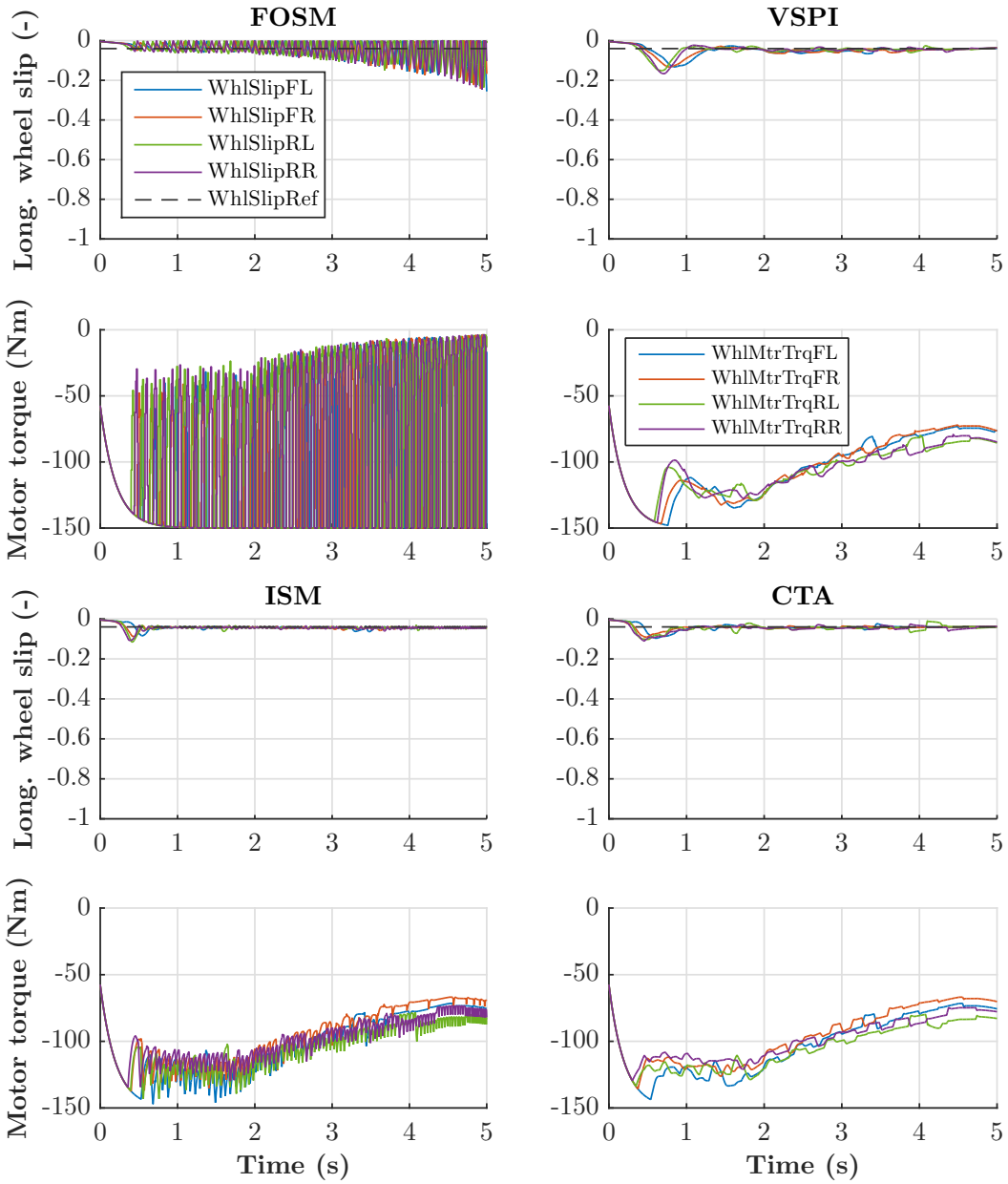

Fig. 4.26 Wheel slip control with in-wheel motors in low road friction conditions

Application of CTA approach allows having similar wheel slip behavior compared to ISM. But as it can be observed on the wheel torque demand, this strategy produces very smooth torque demand. This means that having almost all benefits in terms of WSC, this control can be applied to many other types of decoupled brake systems, as does operates in relatively small frequencies compared to the other control approaches, see Figure 4.27.

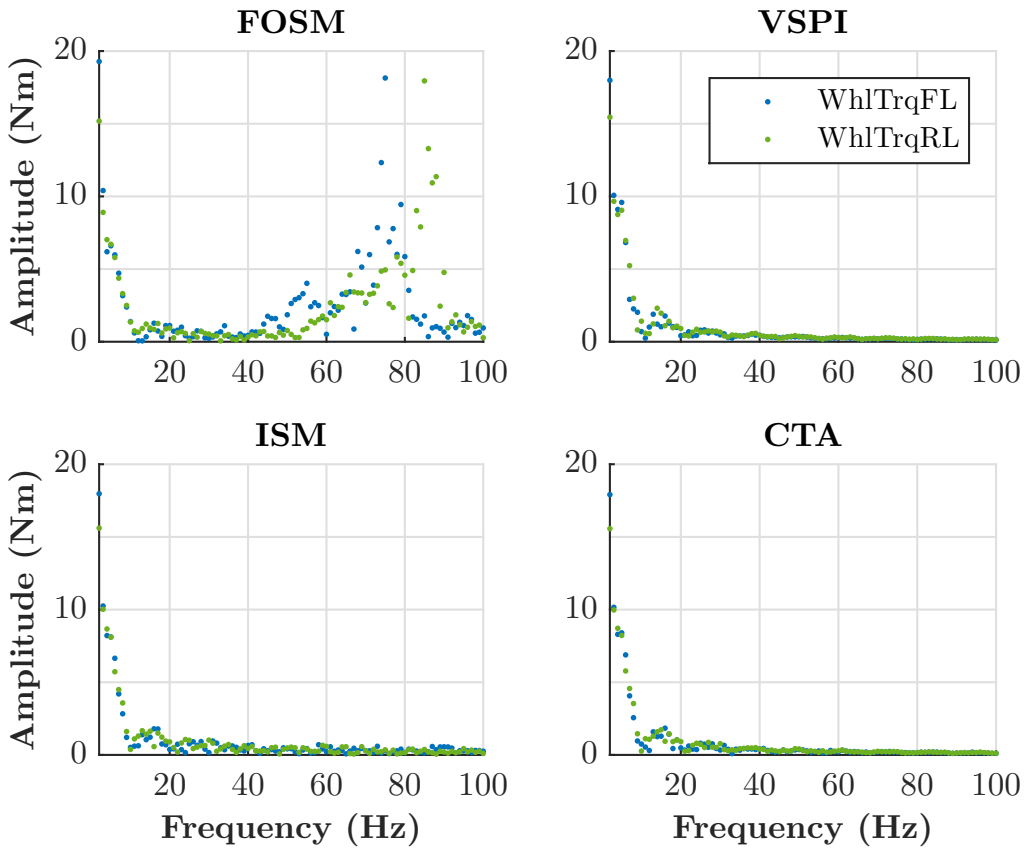

Fig. 4.27 Distribution of the brake torque demand in frequency spectrum

To assess benefits of developed WSC strategies, rule-based approach was used for comparison. For fair comparison of control methods, rule-based approach was used in combination with IWMs. Numerical evaluation of each control strategy was summarized in Table G.3. This shows that VSPI, ISM and CTA controls produce 10 % shorter brake distance than rule-based approach. This was achieved by precise tacking of reference slip value, where $RMSD_\lambda$ varies between 0.01 and 0.03 for front and rear wheels depending on the method. These three approaches show up to 70 % reduction of the first peak compared to the rule-based approach. Due to occurrence of chattering, FOSM remained longer time below optimal wheel slip and has 1 % longer braking distance than rule-based approach, as a consequence. In presence of such wheel force oscillations, FOSM produces the highest level of vehicle jerk deviation from zero value. This has 51 % worse ride quality than rule-based ABS, while VSPI, ISM and CTA methods enhance this characteristic on 82 %.

4.6.4 Chapter summary

In this chapter state estimation and brake system control functions were proposed. Tuning and testing of algorithms in simulation environment was done for all relevant testing cases. Following remarks and conclusion can be given to summarize outcomes of this chapter:

- Developed continuous WSC for considered brake system configurations produce shorter braking distance and reduce vehicle longitudinal jerk compared to rule-based approach for all considered brake system configurations;
- Brake blending with control prioritization in WSC mode showed stable behavior both in low and high road friction conditions despite differences in DEHB and OBM dynamics. This approach was patented by author in [128];
- In the development process of ABS and WSC algorithms, specific road surfaces should be also considered. Author has performed additional investigations of corresponding control approaches for icy road, wet icy road and irregular road conditions, which are explained in details in [129, 88].

Chapter 5

Experimental investigation of the developed control strategy

5.1 Hardware-in-the-loop test rig

Before performing road tests, proposed DEHB WSC algorithms were additionally tested and tuned at the developed hardware-in-the-loop test rig, Figure 5.1. In general, this allows to considering realistic plant uncertainties and reproduce communication delays in the control system. As soon as some of the developed WSC algorithms were developed for the pure friction brake system, performing tuning at the test rig allows to spare a lot of time for trimming algorithms at the proving ground. For this purpose the same SCB brake system was mounted at the rig and connected via corresponding interfaces to the real-time platform produced by dSPACE GmbH.

The developed HIL test rig includes several principle components performing following functions:

- ds1007 processor board provides real-time simulation of the vehicle dynamics software
- ds2002 analogue input board performs measurements of the brake pressure and provides this information to the vehicle dynamics simulation environment to calculate wheel brake torque at each wheel. Besides that, this is used for collecting information about brake pedal travel and pedal force from hydraulic brake pedal robot.
- ds2101 analogue output board produces corresponding reference signals about reference brake pedal travel and pedal force to the hydraulic brake pedal robot.
- ds4302 CAN board is connected to the internal controller of the SCB unit providing interfaces for the brake system control.

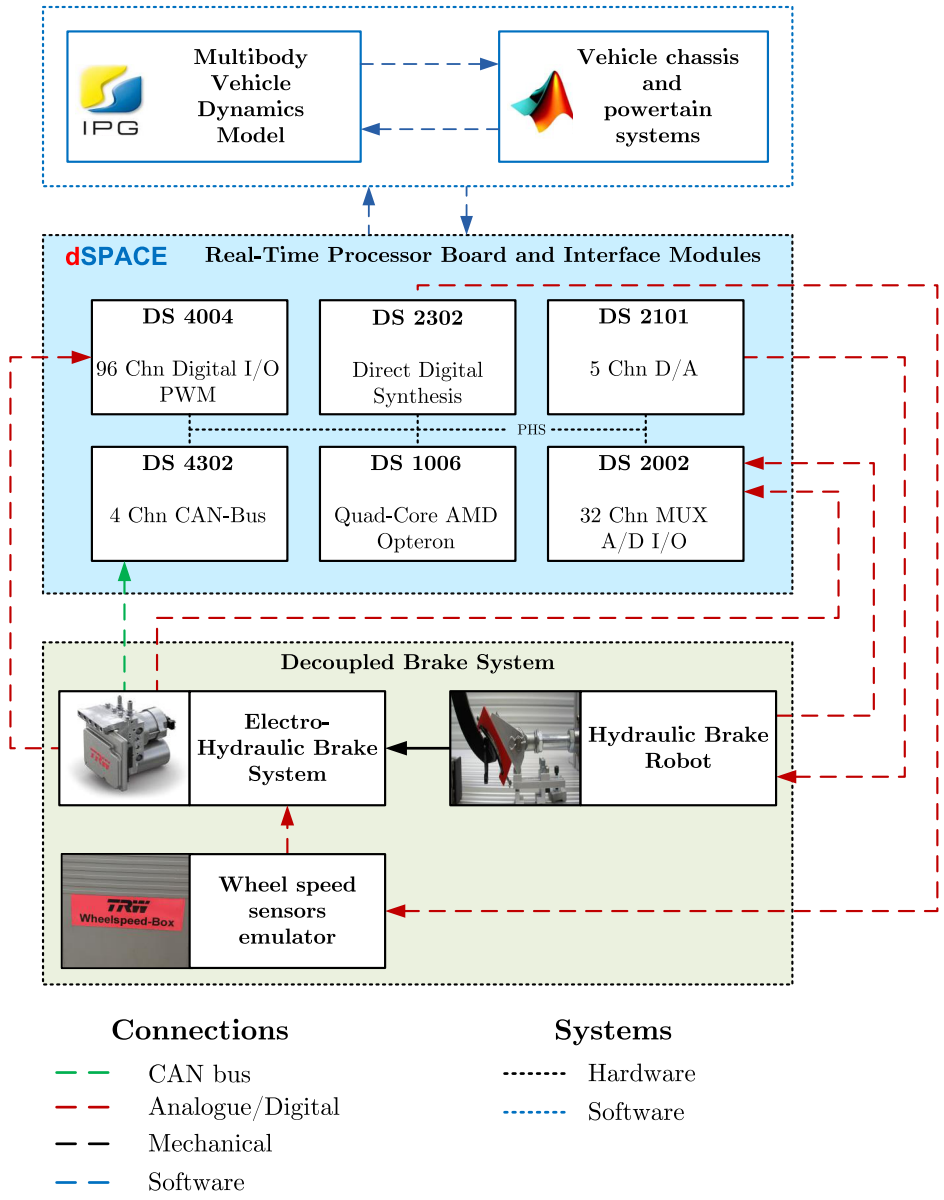

Fig. 5.1 Hardware-in-the-loop brake test rig

- ds2302 board is used as the emulator and uses information about wheel angular speeds from simulation software and sends this to the wheel speed sensors encoder in a converted form.
- Wheel speeds sensors encoder, provided by ZF TRW, produces analogue wheel speed signals to the internal controller of SCB unit encoding digital information received from ds2302.

- Hydraulic brake pedal robot is physically coupled with the brake pedal and provides its actuation. More technical details on the design and control of the hydraulic brake pedal robot can be found in [108].

Calculation of the wheel speed is based on the time and pulse counter information reproducing realistic communication delays and inaccuracies in wheel speed estimation. This uses the same wheel speed calculation routines as on the vehicle demonstrator. Hardware-in-the-loop tests were performed in advance to the road tests to perform fine tuning of the algorithms.

5.2 Wheel slip control with decoupled electro-hydraulic brake system

Initial tuning of the WSC was performed on the road surfaces with preset values of road coefficient of friction. Average value of two relevant road surfaces were used: $\mu_{road} = 0.4; 0.95$. For the final evaluation of the control performance, inhomogeneous road surface was used as for simulations in Section .

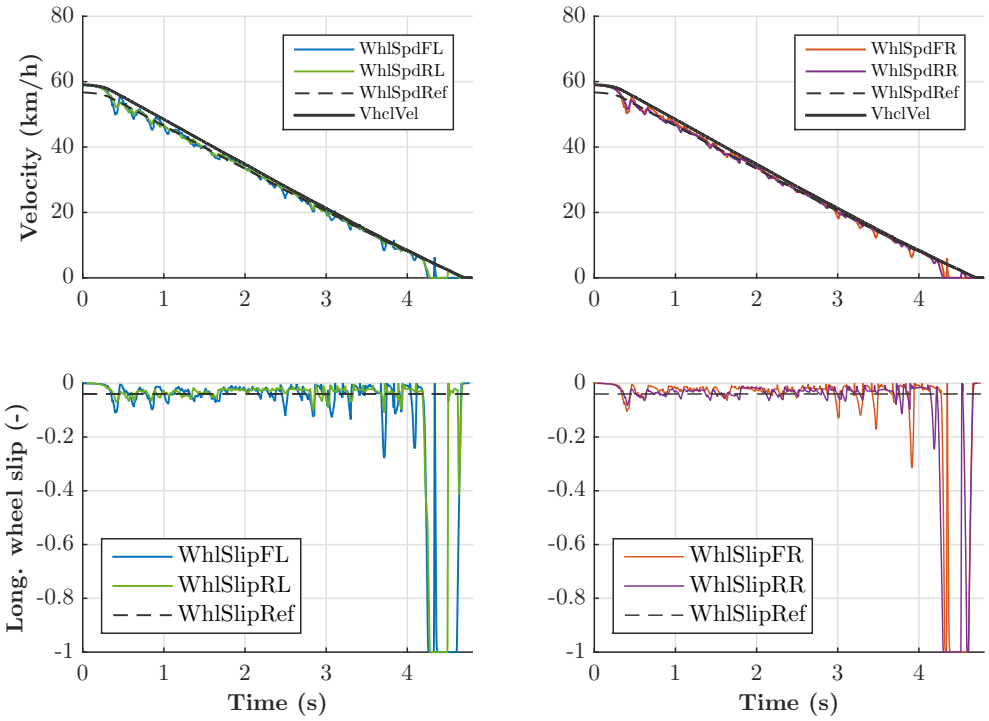

Fig. 5.2 Braking in low road friction conditions: PI control

In considered braking tests, wheel slip reference was fixed at the values, which located close to the optimal point: 0.04 and 0.1 for low and high friction conditions, respectively. Referring to the fact that DEHB has uncertainties in terms of brake pressure control, at least five repetitions were considered for final control evaluation summarized in Table E.1.

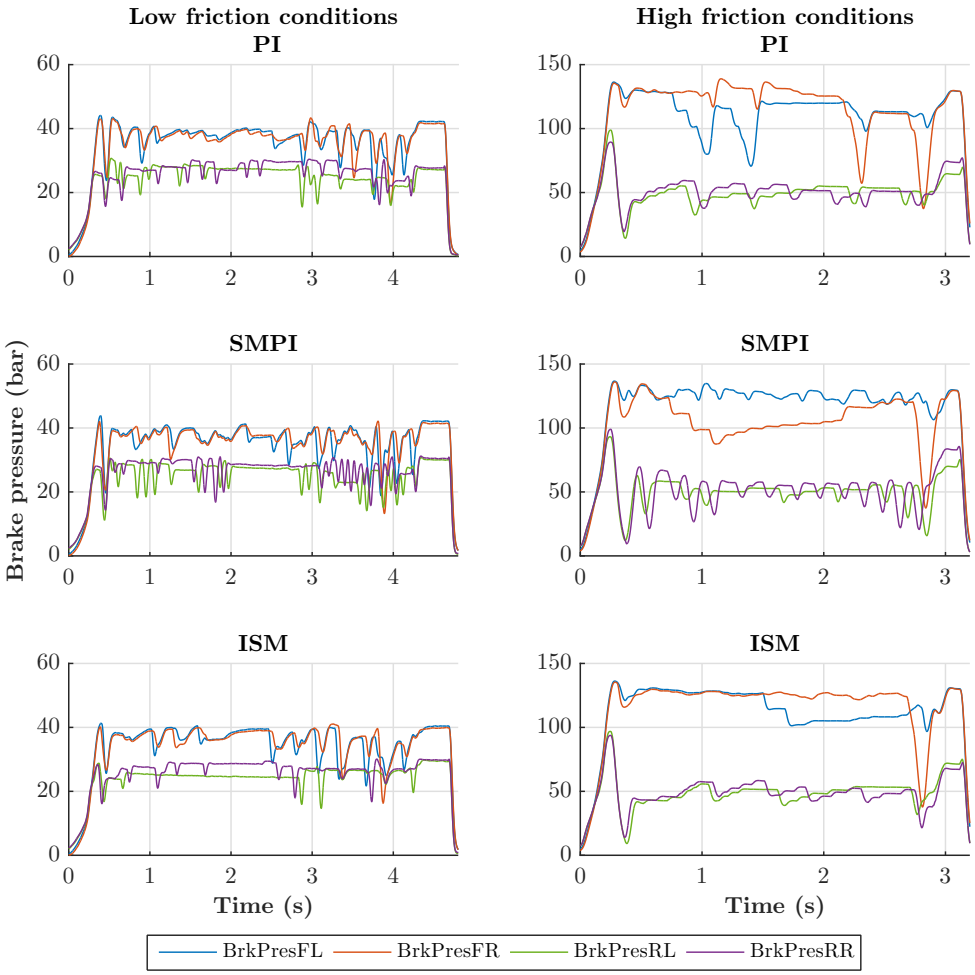

Fig. 5.3 Braking in low and high road friction conditions: brake pressure profile

Compared to the presented simulation cases, HIL tests allow to consider realistic hydraulic interference between pressures in calipers during WSC braking mode. Besides that, dynamics of the brake pressure control is very dependent on its absolute value and on the road friction conditions, as a consequence. This is especially interesting to be analyzed in case of SMPI and ISM controls, which were designed to be robust to the plant uncertainties. Figure 5.2 presents wheel speed and wheel slip profiles for the PI control strategy. It can be observed that wheel slip has oscillations at the initial stage of braking and clear peak at the first cycle of braking. In Figure 5.3 it can be seen that PI control has deeper brake pressure cycles,

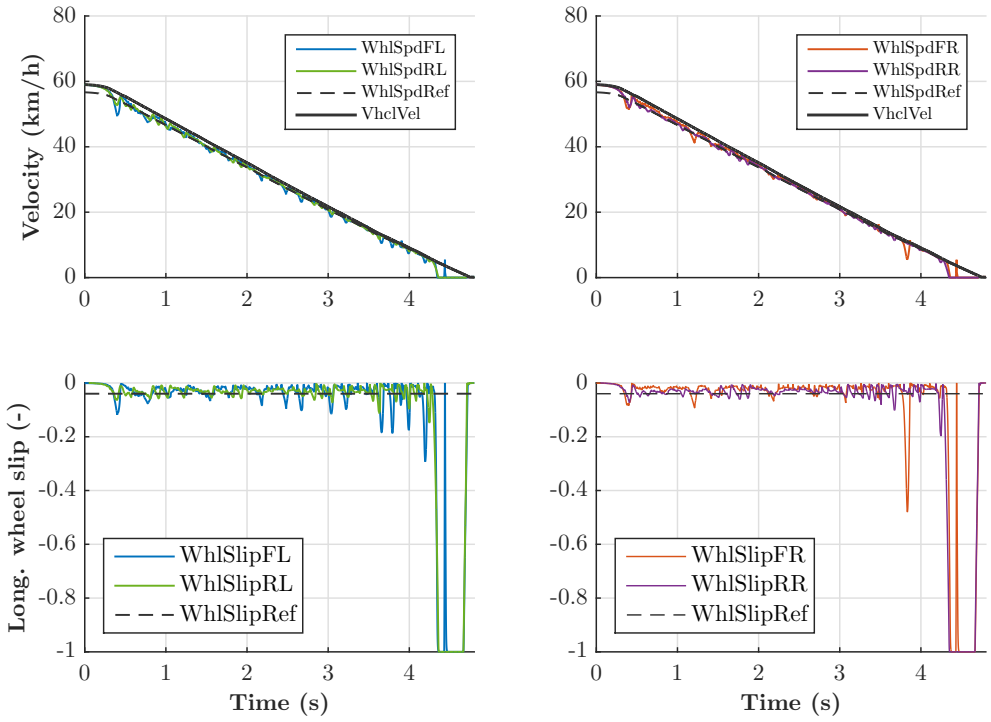

Fig. 5.4 Braking in low road friction conditions: sliding mode PI control

characterized by relatively low frequency. Compared to the simulation, short wheel locking occurs at velocities lower than 10 km/h. In these conditions wheel slip dynamics has much higher gain due to the presence of vehicle velocity in denominator (see Equation 4.39), wheel speed measurements are less accurate and, as a consequence, it is sophisticated to control wheel slip in this range of vehicle velocities. Therefore, deactivation of the WSC happens progressively already from 8 km/h to avoid possible damage of hydraulic valves in EHCU, which may be forced to operate at higher frequencies.

Referring to the simulation results, it was observed that SMPI control produces high-frequency content in wheel torque (or brake pressure) demand. Before implementing this control strategy, it was important to confirm that the DEHB system can cope with such control mode. As it can be seen on brake pressure profile in Figure 5.3, SMPI forces the system to operate at higher frequency compared to PI control. Such quicker reaction and consideration of plant uncertainties on the control design stage, resulted in much better tracking performance of the wheel slip. Compared to the PI, $RMSD_\lambda$ was at least 50 % lower for front and rear wheels. As a consequence, this resulted in 2 % shorter braking distance as in PI case. Moreover, variation of the braking distance also was significantly reduced. This indicates advantages in control system robustness compared to PI control. However,

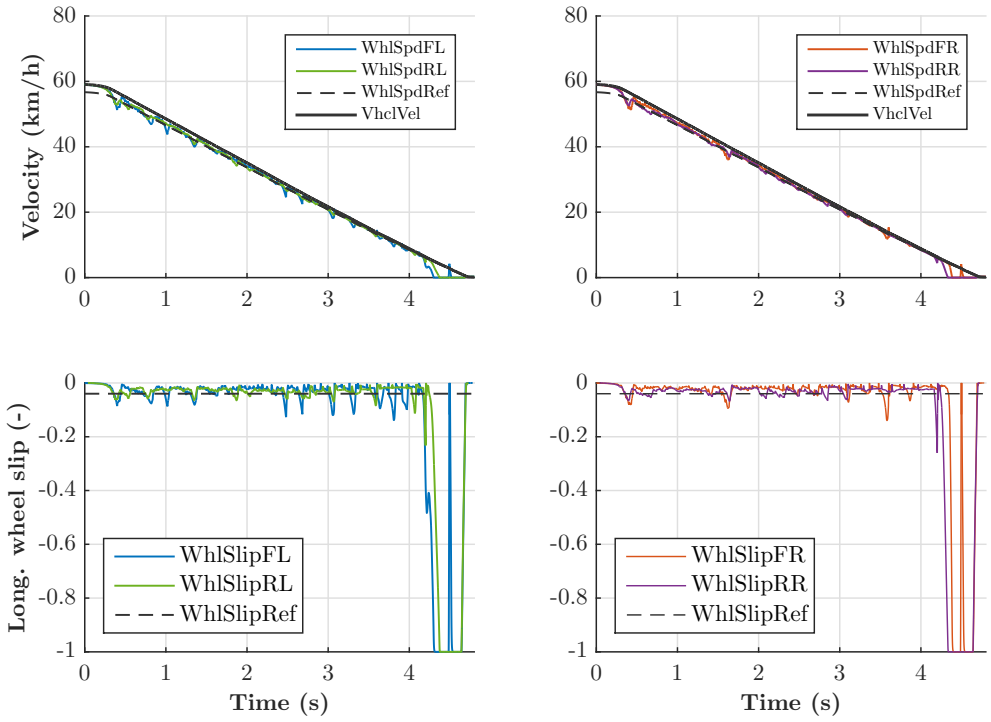

Fig. 5.5 Braking in low road friction conditions: integral sliding mode control

such brake pressure modulation mode has negative influence on the ride quality. This led to almost the same numerical standard deviation of vehicle jerk as for PI.

Compared to PI and SMPI methods, ISM demonstrated precise and in the same time smooth tracking of the wheel slip reference value in simulations, see Section . This was achieved by adjustment of the low-pass filter of discontinuous part, which produces brake torque demand without oscillations typical for the SM methods and significant phase shift due to application of filter. HIL experiments confirmed these benefits of ISM. As it can be seen in Figure 5.5, this approach reacts quickly on possible wheel lock having the lowest first peak among considered control methods. This afterward hold wheel slip close to the optimal wheel slip without significant deviations during the whole braking event. However, to avoid longer operation in linear area, it can be recommended to shift reference wheel slip on 2 % above expected wheel slip optimum. This may be caused in cases, where K_{ism} has too high values and system can produce longer delays for returning to optimal area, as a consequence. Such control performance is also well reflected in brake pressure profile in Figure 5.3: pressure in calipers does not oscillate as in cases of PI and SMPI controls and does not have a deep pressure cycle at initial stage of braking. As soon as in considered DEHB there is still a hydraulic cross-talk between calipers, ISM can be considered as the most applicable WSC method for such configuration of hydraulic brake-by-wire system. Providing compensation of

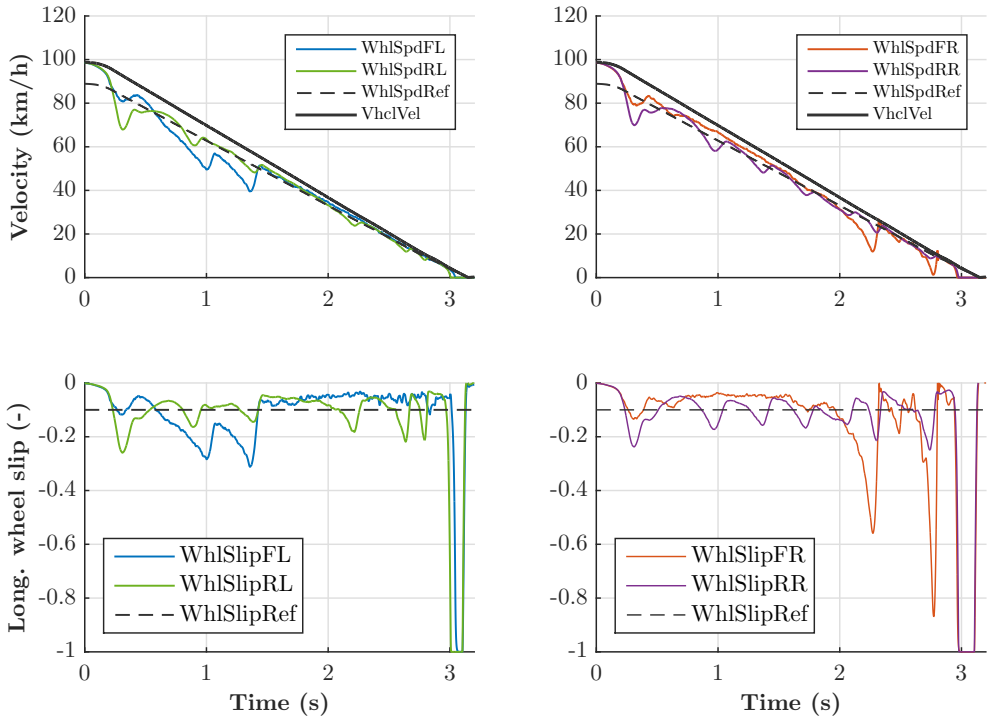

Fig. 5.6 Braking in high road friction conditions: PI control

plant uncertainties and smooth wheel torque demand, this strategy has miserable variation of braking distance, which underlines method's robustness, and provides the 23 % ride quality compared to PI and SMPI strategies.

In general, it can be said that three developed control strategies provided expected results and correlate well with simulation results for low road friction conditions. This was possible to be realized by using DEHB system which can go up to 8-9 Hz of brake pressure modulation frequency with relatively high amplitudes of brake pressure at initial stage of braking.

To confirm robustness of three proposed approaches, emergency braking HIL tests were performed in high road friction conditions. For this purpose, settings of the control gains were taken the same as in low-μ_{road} braking case. As it was mentioned before operation at higher brake pressures may cause inaccuracies in direct brake pressure control, which happens in the closed-loop with WSC. In this sense, PI control produced very high deviations as it is demonstrated in Figure 5.6. Important to remind that road coefficient of friction is presented by stochastic model. Therefore, at some points PI control does not produce agile reaction to μ_{road} variation having deeper cycles in cases, where road friction drops.

As soon as plant uncertainties and components related to the tire force variation were considered in SMPI control, this strategy shows better tracking of the reference wheel slip. The system reacted in agile way as road μ_{road} varied avoiding deep cycling events, see Figure

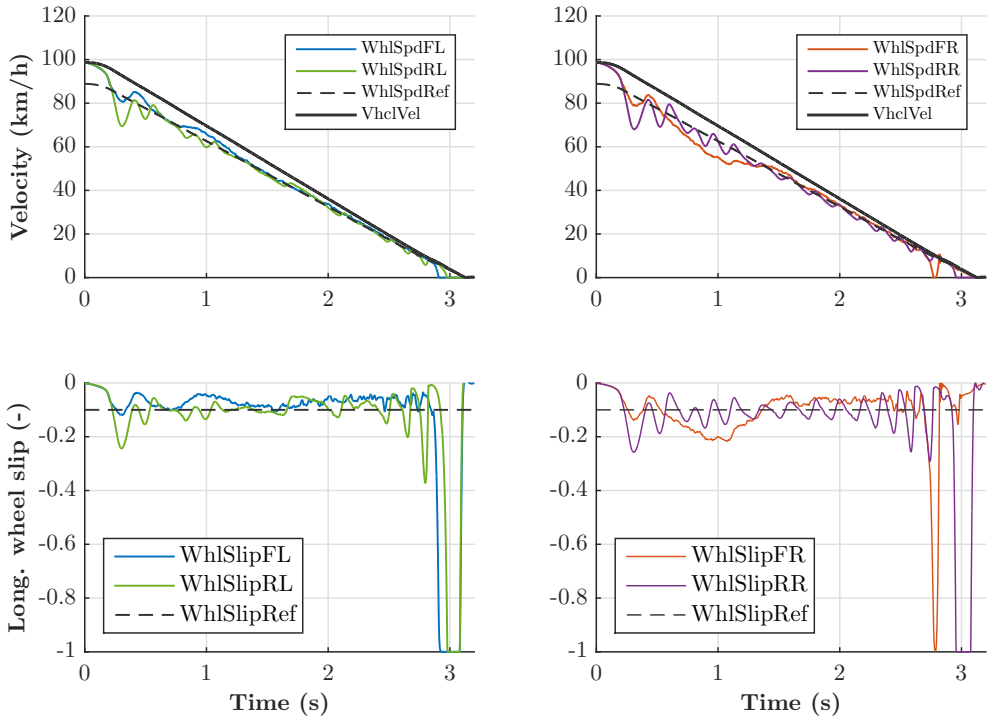

Fig. 5.7 Braking in high road friction conditions: sliding mode PI control

5.7. Discrete part of SMPI produces corresponding control contribution, which forces the system to keep wheel slip at optimal point by modulation of the brake pressure with higher frequency, see Figure 5.3.

Better control performance was demonstrated by ISM control. Discontinuous part in this control is filtered and produces less chattering as in SMPI case. This allows simultaneous compensation of road friction and vertical tire load variations and generation of smooth brake pressure profile, Figure 5.3. This results in up to 13% better ride quality among considered control strategies, while wheel slip tracking performance and braking distance remain comparable.

Low deviations of the braking distance in presence of different wheel slip performance can be explained by the properties of considered tires in high friction conditions: force degradation is not that high after passing the optimal wheel slip. For sure, this might be different with other type of tires, where SMPI and ISM controls are expected to provide benefits also in terms of the braking distance.

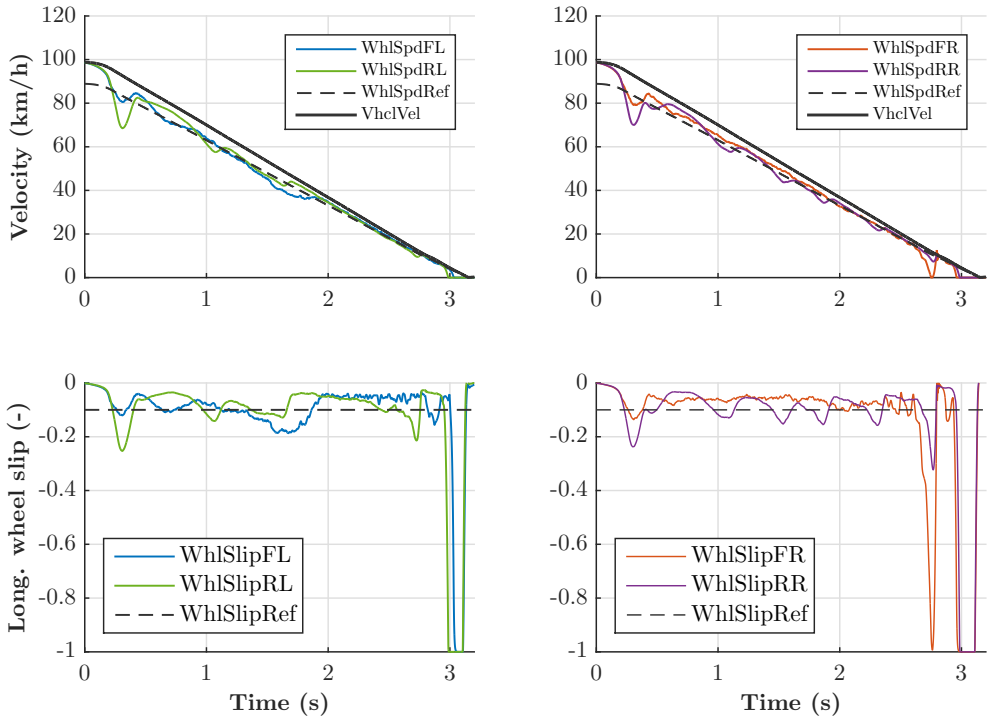

Fig. 5.8 Braking in high road friction conditions: integral sliding mode control

5.3 Chapter summary

Developed control strategies PI, SMPI and ISM were test by means of HIL technique using DEHB system. Obtained results were numerically summarized in Table E.1 and together with described observations allow making following conclusions:

- HIL experiments correlate with results obtained in simulation having difference not higher than 6 % in braking distance
- PI control can cause instabilities in WSC when using real DEHB brake actuator and stochastic road friction model
- Compared to PI control, SMPI strategy provides better wheel slip tracking in low road friction condition but might be unstable while braking on road with high coefficient of friction
- ISM provides robust operation in low as well as in high road friction conditions
- Among considered control methods, ISM control demonstrated significantly better ride quality

- Derived brake pressure profiles allowed exclude risks in damaging DEHB system during road tests in both low and high road friction conditions

Chapter 6

Experimental validation of the developed control strategies on the vehicle prototypes

6.1 Vehicle specifications

6.1.1 SUV with four individual on-board electric motors

Electric vehicle demonstrator used for experimental validation of WSC and brake blending control is based on the SUV Range Rover Evoque platform, Figure 6.1. This vehicle has four individual on-board motors, which transfer torque to the wheel through the half-shafts. Having peak torque of 200 Nm in traction and braking modes, each motor can produce approximately 2000 Nm at the wheel through the two-stage reducer. Vehicle and powertrain technical data is summarized in Table 6.2.

Fig. 6.1 Vehicle demonstrator with on-board electric motors: individual electric motors on the front axle (left) and vehicle demonstrator at Lommel Proving Ground (right)

DEHB system implemented on the EV demonstrator uses SCB technology developed by ZF TRW. The system is coupled to other vehicle subsystems and components through two CAN connections. The Vehicle CAN is responsible for embedding DEHB system into the vehicle architecture. In particular, the communication between EHCU and VCU is realized through this CAN. The Private CAN transmits signals about system status, pedal travel and wheel speeds. For the purposes WSC and state estimator validation, vehicle was equipped with following devices: dSPACE processor board DS1005 with digital input/output, CAN and multi-channel A/D boards; VBOX RaceLogic dual antenna; Correvit optical velocity sensor; Kistler wheel force sensor.

Table 6.1 Vehicle demonstrator with on-board electric motors: technical data

Vehicle	
Vehicle type	Land Rover Range Rover Evoque
Full mass (kg)	2117
Driveline	All wheel drive
Maximal speed (km/h)	182
Tire size	235/55 R19
Wheelbase (m)	2.660
Track width (m)	1.625
Transmission	two-stage reducer with helical gears
Gear ratio	1:10.5
Half-shaft torsional stiffness (Nm/rad)	6500
Electric motors	
Peak torque (Nm)	200
Peak power (kW)	100
Nominal torque (Nm)	135
Nominal power (kW)	42
Maximum speed (rpm)	15000

6.1.2 SUV with decoupled electro-hydraulic brake system

SUV demonstrator equipped with SCB DEHB system is shown in Fig. 6.2. For validation of the state estimator, additional measurement systems were installed: dSPACE processor board DS1007 with digital input/output, CAN and multi-channel A/D boards; brake pressure sensors; brakes temperature sensors; Kistler wheel force sensor RoaDyn S635; Racelogic VBOX dual antenna (VB3i SL) 100 Hz GPS Data Logger.

Straight-line braking maneuvers were done in high and low road friction conditions at the airport Alkersleben, Germany. Braking tests in low friction conditions were performed with

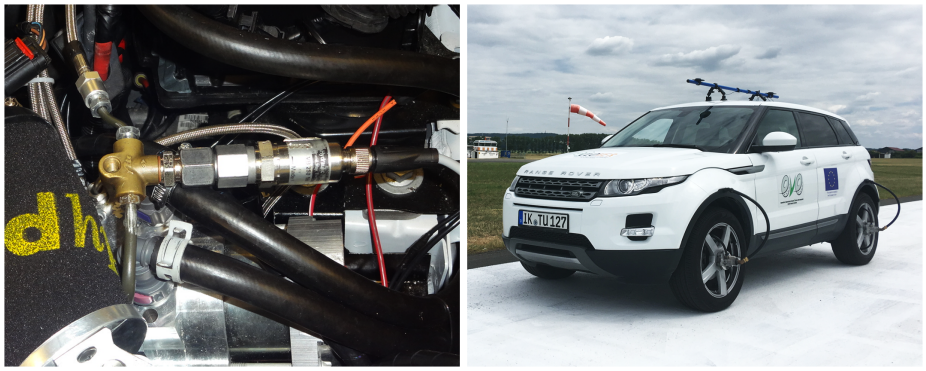

Fig. 6.2 Vehicle demonstrator with decoupled electro-hydraulic brake system: SCB system (left) and vehicle demonstrator at Alkersleben airport (right)

initial velocity of 60 km/h due to limitations in the road section length, while 100 km/h was the initial velocity for high road friction conditions. Specifications of the vehicle and brake system are presented in the Table 6.2. Validation of developed WSC control were performed at Lommel Proving Ground, Belgium [130] on the road surface composed of the basalt tiles, which are continuously wet by water sprinklers. Straight-line braking tests were carried out from velocity of 60 km/h due to limitation in road section length.

Table 6.2 Vehicle demonstrator with decoupled electro-hydraulic brake system: technical data

Vehicle	
Vehicle type	Land Rover Range Rover Evoque
Full mass (kg)	2275
Driveline	Front wheel drive
Maximal speed (km/h)	182
Tire size	235/55 R19
Wheelbase (m)	2.660
Track width (m)	1.625
Gearbox	Six-speed, manual
Engine type	Diesel internal combustion engine
Engine capacity (l)	1.999
Brakes	
Front equivalent brake radius (m)	0.12
Rear equivalent brake radius (m)	0.1325
Front brake cylinder diameter (m)	0.057
Rear brake cylinder diameter (m)	0.04

6.1.3 Vehicle demonstrator with four individual in-wheel electric motors

The vehicle demonstrator is equipped with four individual outer-rotor-type IWMs, which adopt a principles of direct drive system [131]. This means that reaction forces from the road are transmitted directly to the motors without gear reduction or backlash. This vehicle was used for assessment of WSC strategies based on VS and SM methods. Therefore, vehicle state estimator was not used in this part of research. For providing vehicle velocity measurements to WSC, Correvit optical sensor was used. Algorithms were implemented on the dSPACE real-time platform equipped with ds1005 processor board.

Fig. 6.3 Vehicle demonstrator with in-wheel electric motors: hub electric motor at front left wheel (left) and vehicle demonstrator at University of Tokyo testing track (right)

Road tests were done with the initial velocity of 25 km/h considering length of the track section. For providing low road friction conditions, wet plastic sheets were utilized.

Table 6.3 Vehicle demonstrator with four individual in-wheel electric motors: technical data

Vehicle specification	
Vehicle type	FPEV2-Kanon
Full mass (kg)	870
Driveline	All wheel drive
Wheelbase (m)	1.7
Track width (m)	1.3
Wheel radius (m)	0.302
Electric motors	
Front motor peak torque (Nm)	$\pm$500 Nm
Rear motor peak torque (Nm)	$\pm$340 Nm

For better readability, experimental results presented in next sections were classified according to utilized brake system type, applied control strategies and testing conditions, as shown in Figure 6.4.

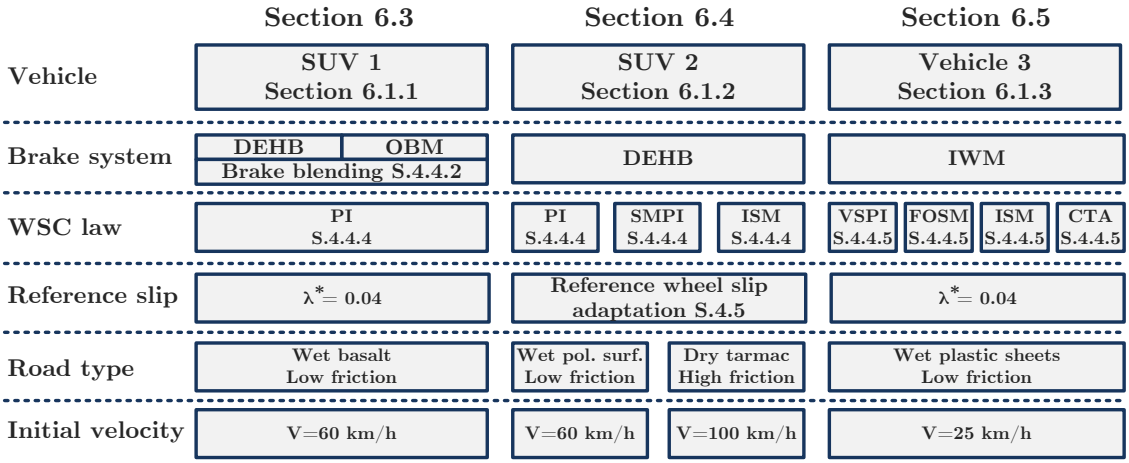

Fig. 6.4 Overview of performed experimental validation tests with vehicle prototypes

6.2 Validation of the state estimator

State estimator developed in Section 4.3 was validated experimentally during the road tests with SUV demonstrators. One of the main tasks was estimation of vehicle velocity during continuous WSC where wheels are kept at non-zero reference value. This situation is different to the rule-based ABS approaches, as wheels are not periodically being unlocked to estimate vehicle deceleration and velocity. Figure 6.5 presents a case of braking in high road friction conditions with activated WSC. Properly detected wheel lock status allows reassigning gains in the velocity state observer between other wheels and vehicle deceleration sensor. Estimated and measured velocities have root-mean square deviation about 0.8 km/h.

Similar occurs during the braking in low road friction conditions, Figure 6.6. RMSD between estimated and measured values has average value of 0.5 km/h in this particular case. The highest difference occurs at initial stage of braking and can be reduced by further inclusion of disturbances estimation in overall state observer architecture. This is determined by the fact that e.g. rolling resistance causes deviation between measured wheel and real vehicle velocities.

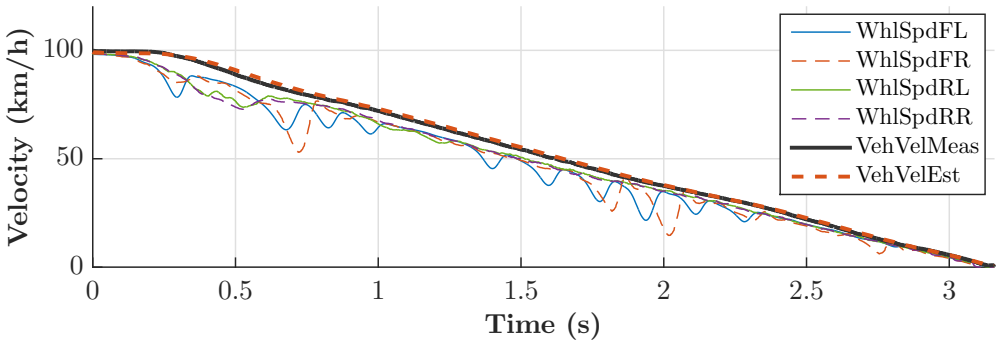

Fig. 6.5 Validation of vehicle velocity estimator: ABS braking in high road friction conditions

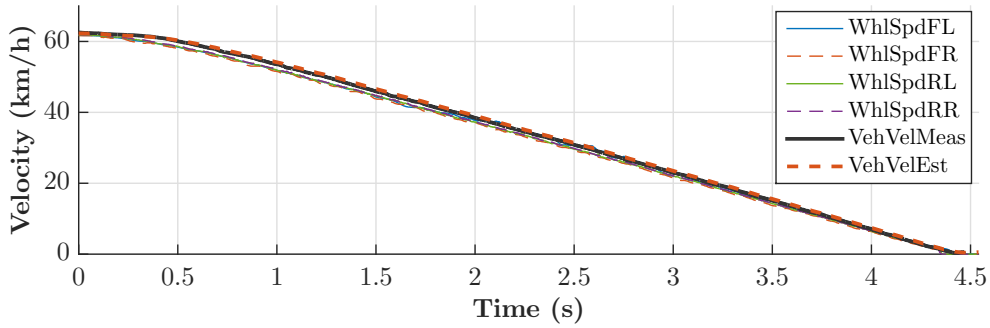

Fig. 6.6 Validation of vehicle velocity estimator: ABS braking in low road friction conditions

Although aforementioned possible improvements, these results present velocity estimation applicable for WSC purposes. Compared to the state of the art solutions, active wheel speed sensors on the rear axle (more accurate wheel speed measurements at low velocities) and longitudinal acceleration sensor (more accurate information about acceleration than conventional estimation techniques) were utilized and allowed accurate velocity estimation for the developed WSC algorithms.

Obtained velocity was used for the calculation of longitudinal wheel slip, as well as for estimations of its reference value. To validate estimation of longitudinal tire force necessary for reference wheel slip adaptation logic, measuring wheel hub was mounted at the front right wheel on the SUV demonstrator described in subsection 6.1.2. As it can be on the left side of Figure 6.7, observed and measured relation between longitudinal tire force and wheel slip shows exact correlation in linear and nonlinear areas. This allows application of adaptation logic (Appendix B) for further determination of reference wheel slip value. One of the main influencing disturbance in this case is the lining coefficient of friction. Its variation is influenced by various environmental conditions and operation modes of friction brakes. This variation is well-captured by RLS estimator, as shown on the right side of Figure 6.7.

This observer together with reference adaptation logic is further tested in closed-loop with developed WSC in Section 6.4.

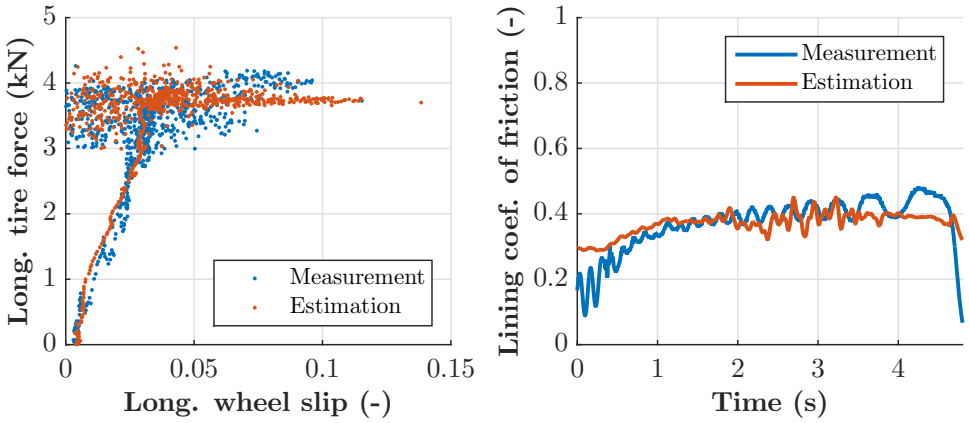

Fig. 6.7 Validation of state estimator during WSC: tire longitudinal force (left) and lining coefficient of friction (right) at front right wheel

Additionally to the straight line braking tests, a set of lateral tests with demonstrator from subsection 6.1.1 was performed to check robustness of the tire forces and vehicle states estimator. This allows to check accuracy of longitudinal and lateral forces estimation under combined slip conditions. Figures in Appendix G present relevant estimations for steady cornering and slalom tests. They show accurate reconstruction of tire forces and vehicle states validated with experimental data.

6.3 Wheel slip control with brake blending

The tests with the SUV equipped with four individual OBMs and DEHB system were performed in low road friction conditions at the Ford Lommel Proving Ground [130]. Emergency braking tests were performed to check possibility of using electric motors as main actuator in ABS mode and assess their advantages over EHB and DEHB systems. In particular, developed PI with anti-windup approach for WSC was applied to the vehicle with OBM configuration and serial production rule-based algorithms were used in the vehicles with EHB and DEHB systems. For detailed specifications of the brake system configurations, interested can refer to the author's paper [115].

In electric vehicle configuration, torque demand was completely covered by OBMs and progressively blended with DEHB when reaching vehicle velocity of 20 km/h. From this point, DEHB overtakes brake control functions which allows to hold the vehicle in stand still positions at the end of braking event. Another two vehicle configurations used pure EHB

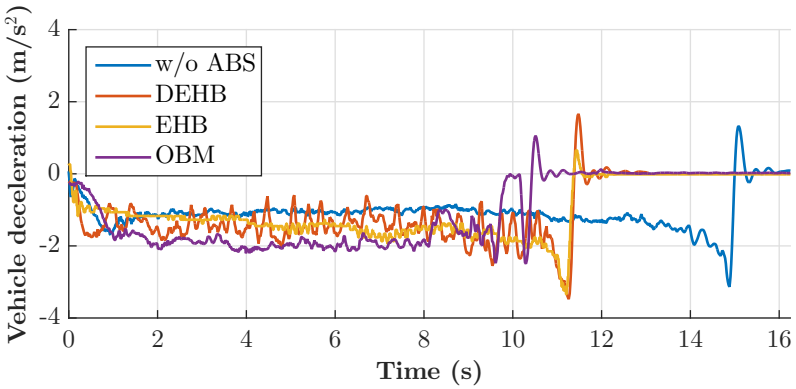

Fig. 6.8 Vehicle deceleration profile: braking in low road friction conditions

or DEHB control to provide ABS braking. Hence, following brake system configurations installed on the same SUV type were considered for benchmarking: a) OBMs and DEHB with brake blending functions and continuous ABS control; b) stand-alone DEHB with rule-based ABS; c) stand-alone DEHB for baseline braking without ABS; c) stand-alone EHB with rule-based ABS.

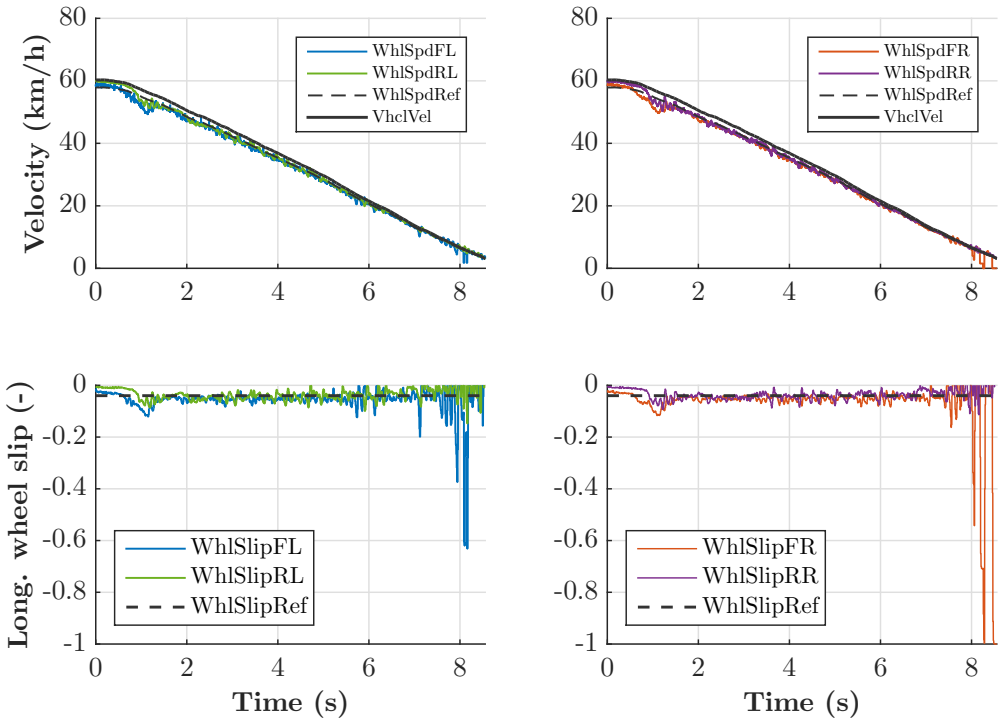

Fig. 6.9 Electric vehicle with continuous WSC: wheel slip and velocity profile

One of the main ABS tasks is to achieve a required vehicle deceleration as requested by driver in emergency braking cases by avoiding the wheels lock. The vehicle deceleration

profile for four brake system configurations is shown in Figure 6.8. Here the rule-based ABS strategy used in EHB and DEHB systems demonstrates comparable results in terms of the braking time and mean deceleration having 1.4 m/s^2 in both cases. The highest achieved deceleration of 1.9 m/s^2 was performed by the developed continuous ABS system, which involves electric brakes in the most of braking time. Such braking performance produced by OBMs was achieved by smooth and precise tracking of the wheel slip reference, as shown in Figure 6.9. All four controlled wheels achieved $RMSD_\lambda = 0.05$ when electric motors were operating alone, and $RMSD_\lambda = 0.07$ when DEHB interaction occurred at lower velocities with preset reference value $\lambda^* = 0.04$.

Such precise tracking was realizable due to quick electric motors reaction and applied brake blending strategy as described in Section 4.4.2. Figure 6.10 presents brake torque profile of OBM and DEHB during ABS braking with electric vehicle. As it can be seen, operational frequencies can achieve 8-10 Hz with such configuration which is distinctly higher than for conventional EHB systems.

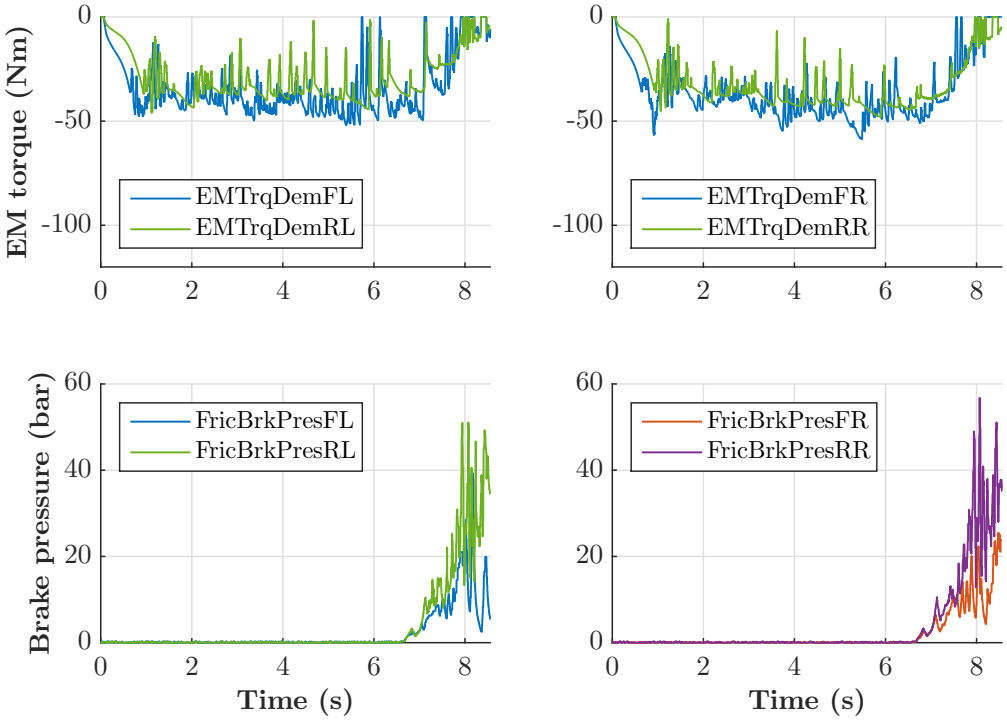

Fig. 6.10 Electric vehicle with continuous WSC: drivetrain torque demand and brake pressure

As soon as the rule-based algorithms and both EHB and DEHB systems were represented by the industrial solutions, the reference value of the wheel slip ratio could not be accessed and tracking performance of the system was not analyzed for these two systems. However, knowledge about optimal wheel slip (around $\lambda = 0.04$) allows assessing system performance

by comparing with mean wheel slip values. As it can be seen in Table G.1 and in Figures 6.11 and 6.12, EHB and DEHB systems operated at higher wheel slip values. This is determined not only by the optimum seeking routines in rule-based algorithm, but also by limitations in operational frequency of hydraulic actuator. ABS in these cases was reaching only 1-3 Hz, which is significantly lower than aforementioned frequency of electric motors supplied with continuous ABS control. Due to these limitations and applied switching logic, a suboptimal operation is inevitable for conventional ABS approaches.

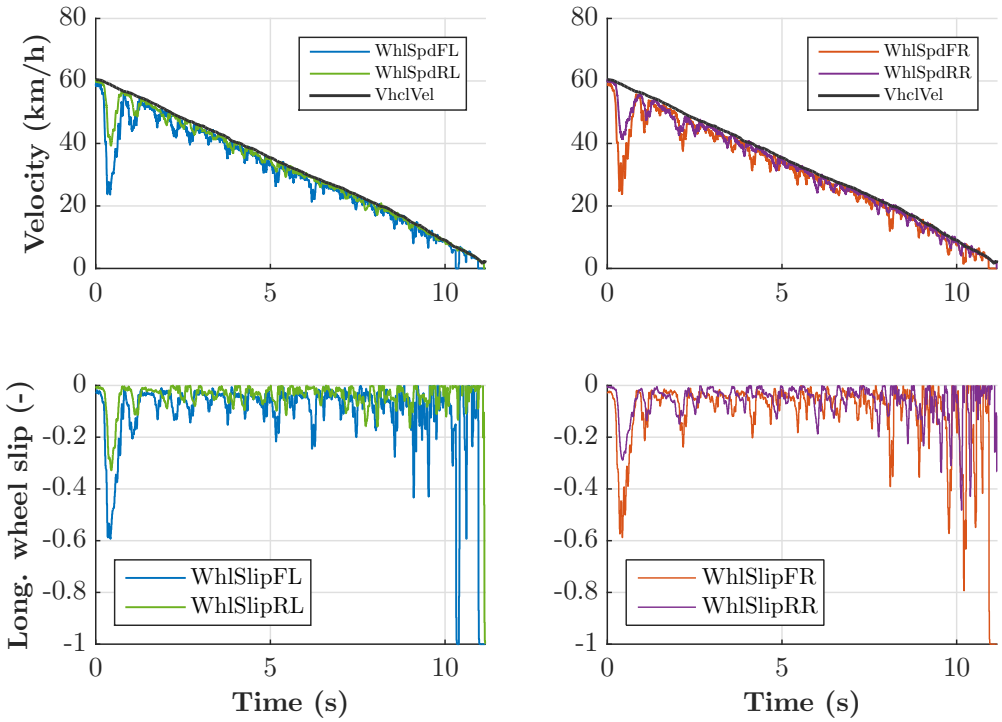

Fig. 6.11 Vehicle with decoupled electro-hydraulic brake system: wheel slip and velocity profile

Another important factor influencing on brake performance is how agile ABS reacts on variation of wheel slip dynamics at activation phase. First peak of the initial ABS control cycle can be seen on the velocity profile in, Figures 6.10,6.11 and 6.12. As soon as on the electric vehicle electro-hydraulic brake system was mostly used as the backup solution, tuning of the system was not performed. Due to this fact the ABS of the decoupled electro-hydraulic brake system has a peak of 0.57 and 0.31 for front and rear wheels, which can be significantly reduced by adjusting the control parameters of the algorithm. A quicker reaction is observed by the conventional hydraulic ABS: peak value of 0.36 both on front and rear wheels. The best performance in terms of the system adaptability and reaction was

demonstrated by developed continuous ABS control with combined brake system, where peak values of the initial cycle are just of 0.06 and 0.06 for front and rear wheels, respectively.

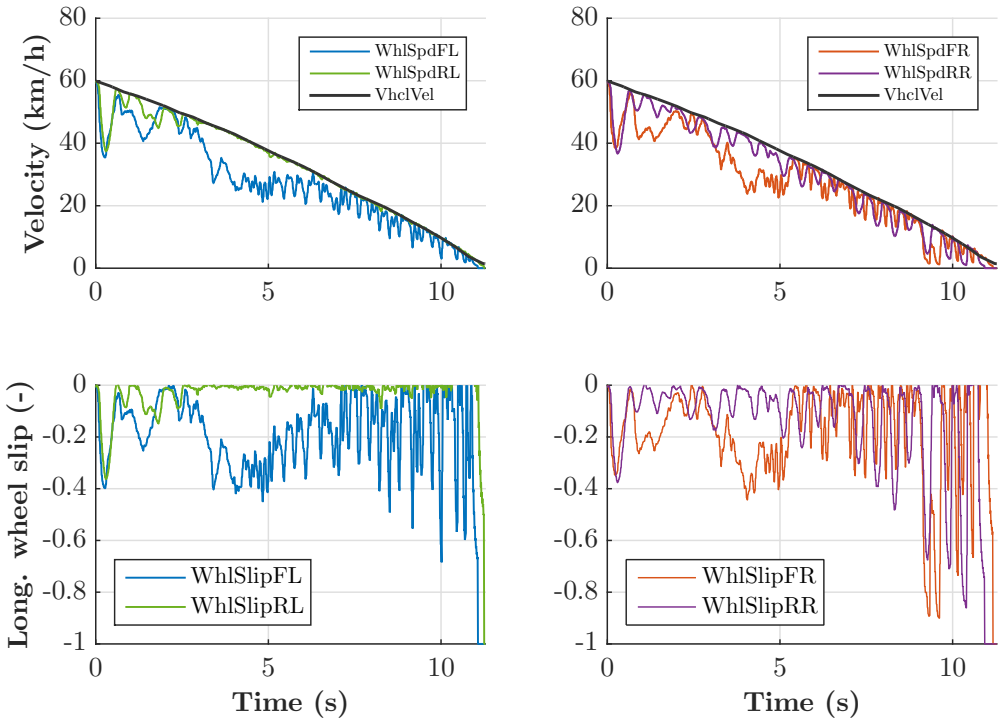

Fig. 6.12 Vehicle with decoupled electro-hydraulic brake system: wheel slip and velocity profile

Negative influence on the ride quality during the ABS braking occurs due to the fluctuations in the braking force that produce oscillations in the vehicle deceleration, as a consequence. To characterize the driving comfort characteristics, vehicle jerk signal was derived from the vehicle acceleration measurements. The less is the vehicle jerk the better ride quality is provided by the ABS. The lowest STD value has been obtained for the braking with continuous ABS of electric vehicle with $STD_{j_x} = 0.3m/s^3$ as compared with the EHB ABS $STD_{j_x} = 0.7m/s^3$ and DEHB ABS $STD_{j_x} = 0.8m/s^3$. Therefore, developed continuous ABS strategy is certainly advantageous also in terms of ride quality. Such system property is especially important for the high vehicle automation levels, where the driver should not experience such oscillations even during ABS braking.

Obtained experimental results were numerically summarized in Table G.1 and graphically in radar plot, as shown in Figure 6.13. In this figure, *better system performance corresponds to higher values on the chart*, as all numerical criteria were normalized for better readability. Such graphical representation and aforementioned analysis allows to make following conclusions:

- Braking distance with continuous electric ABS is 20 % less than in case of rule-based ABS;
- In terms the ABS adaptability, electric ABS showed significant reduction of the first peak value in comparison to the other investigated solutions;
- Better ride quality was achieved by using continuous ABS with brake blending, which reduces vehicle jerk up to 76 % as compared with the rule-based systems.

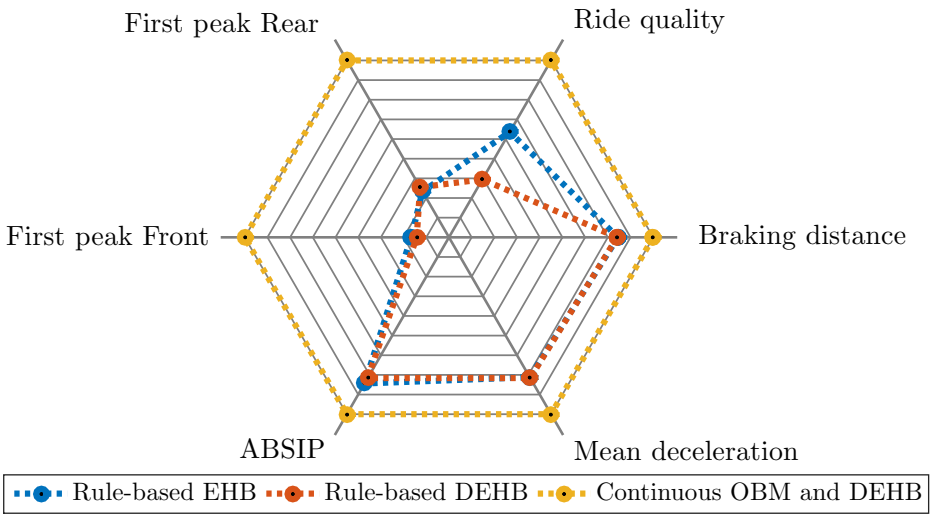

Fig. 6.13 Experimental comparison of developed ABS system with state of the art solutions

Evident advantages of using continuous ABS control have motivated author to apply this control strategy to the DEHB system. This allows checking influence of the control strategy on braking performance and ride quality, while using the same brake system actuator. Next section presents experimental results for the vehicle demonstrator from Section 6.1.2 equipped with DEHB system. This analyzes PI control law with anti-windup action, compares this strategy with robust SMPI and ISM strategies and involves reference slip adaptation and vehicle state and parameter estimator in closed-loop with developed WSC approaches.

6.4 Wheel slip control with decoupled electro-hydraulic brake system

Designed for WSC purposes PI, SMPI and ISM control algorithms were tested on the SUV demonstrator equipped with DEHB system (Section 6.1.2) in closed-loop with the

state estimator, i.e. using only on-board sensors installed on the serial production vehicle. To evaluate advantages of developed controls over the state-of-the-art solutions, typical switching rule-based control was considered for comparison. As it was mentioned in the previous section, this algorithm is characterized by deep periodic cycles of the wheel slip typical for SUV applications. To evaluate effectiveness of the reference adaptation (RA) algorithm, both cases with adaptive and preset reference wheel slip were considered. The preset value was selected to be so close as possible to the optimal area of the F_x-λ diagram.

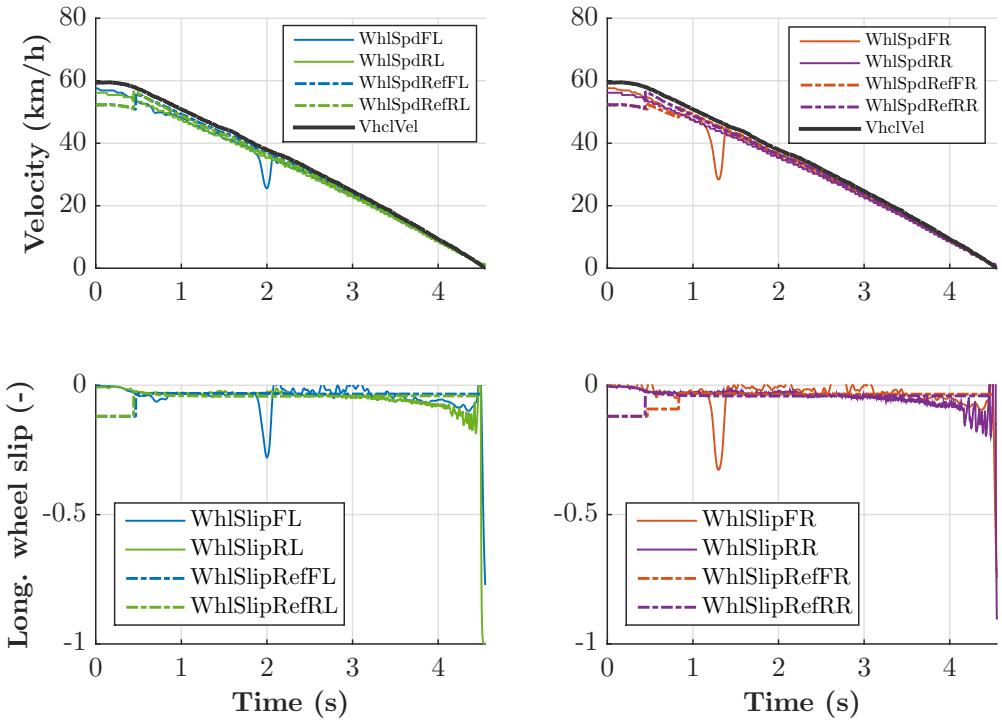

Fig. 6.14 Braking in low road friction conditions: PI control

After preliminary tuning of the control gains in SIL and HIL environments, they were fine-tuned on the vehicle during the tests in low road friction conditions. As soon as appropriate RMSD values of the wheel slip were achieved for each control strategy, six developed controller configurations were further considered and numerically evaluated, as it was presented in Table 4.1: PI, SMPI and ISM with the preset reference and with reference adaptation algorithm. Important to admit that five test repetitions were considered for evaluation of each control strategy. Compared to the switching rule-based control, on the low friction road surface the braking distance was reduced by application of developed controls with and without reference adaptation algorithm in 25 % and 31 %, respectively. The shortest braking distance was achieved by ISM RA control, which is on 7 % and 2 % shorter than PI RA and SM RA correspondingly. More robust operation of the system can be

seen by comparing variations of the braking distance: switching rule-based causes deviation in 9 % from the median value, while this can be reduced up to 3 % in the case of ISM RA control.

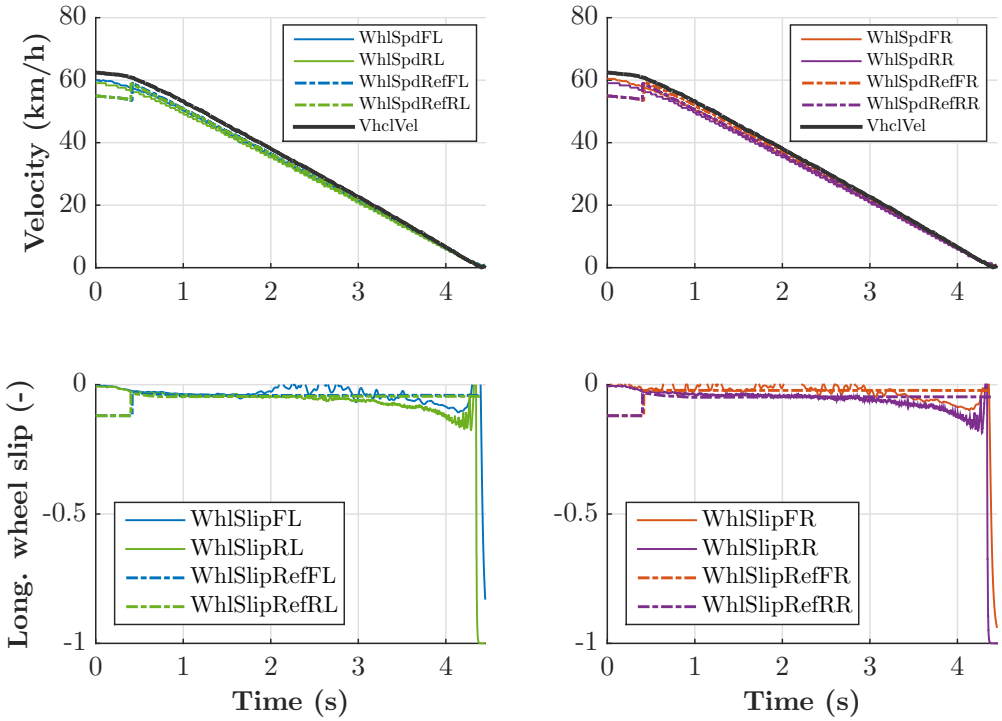

Fig. 6.15 Braking in low road friction conditions: sliding mode PI control

Assessing the effectiveness of the reference adaptation algorithm itself, it provides a reduction in braking distance up to 2 % in comparison to the cases with preset reference wheel slip. It confirms hypothesis that during the emergency braking the optimal area of the F_x-λ diagram can deviate from its initial value and emphasizes importance of the reference adaptation. In particular, reference wheel slip in low-μ conditions varied during the test in the range from 0.02 up to 0.05, while preset reference value was at 0.04. All six controller types have evident advantage over the switching rule-based control in terms of ride quality by reducing longitudinal deceleration oscillations in 55 % as indicated by STD of the deceleration in Table G.2. This is achieved by smooth tracking of the wheel slip (see Figure 6.14, 6.15 and 6.16) as well as by proper estimation of the reference wheel slip and its slow variation.

Existing continuous WSC methods usually do not assure required system robustness. Once the control gains are properly tuned for the low-μ road surface, the control can produce more oscillatory behavior in high-μ friction conditions that is caused by the nature of tire-road interaction. Therefore, to check the robustness, control gains were kept the same as

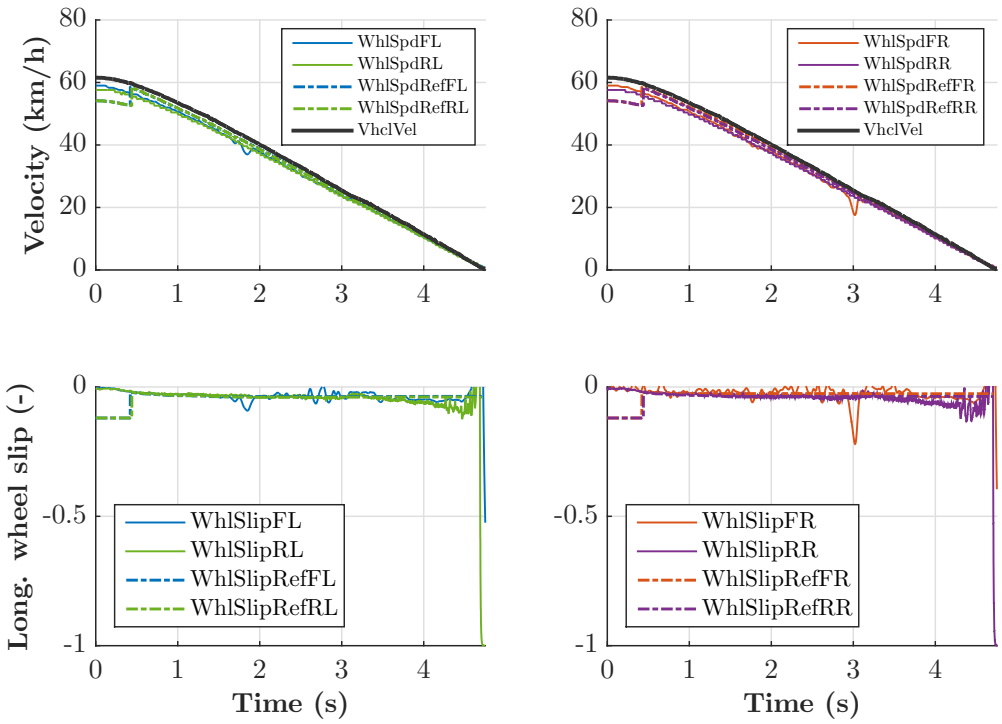

Fig. 6.16 Braking in low road friction conditions: integral sliding mode control

during the tests on the low-μ surface. As a result, wheel slip RMSD remained at almost the same level for SMPI and ISM, while PI control has three-four times higher deviations due to the more oscillatory behavior, Figure 6.17. Important to admit that SMPI control has less stable behavior compared to ISM control, which provided smooth wheel slip tracking in high road friction conditions, see Figure 6.18 and 6.19, respectively.

In terms of braking distance and ride quality, it leads in the case of PI control with constant wheel slip reference ($\lambda^* = 0.1$) to comparable results with the switching rule-based control. Even by applying PI RA, a 3 % shorter braking distance can be attained with still comparable ride quality. Moreover, difference between the minimal and maximal braking distance remains in a quite high range for PI control that indicates insufficient robustness. A similar problem occurs with SMPI control, which produces more chattering on the high-μ road. It results in almost the same ride quality, while the braking distance is reduced in 4 % compared to the switching rule-based control.

Much better results were shown by ISM, where the braking distance was reduced on 9 % and ride quality was improved on 27 %. Important to admit that by application of RA strategy less effect in reduction of the braking distance in high road friction conditions was attained. It happens due to the thinner optimal area of F_x-λ diagram and a more homogeneous type of

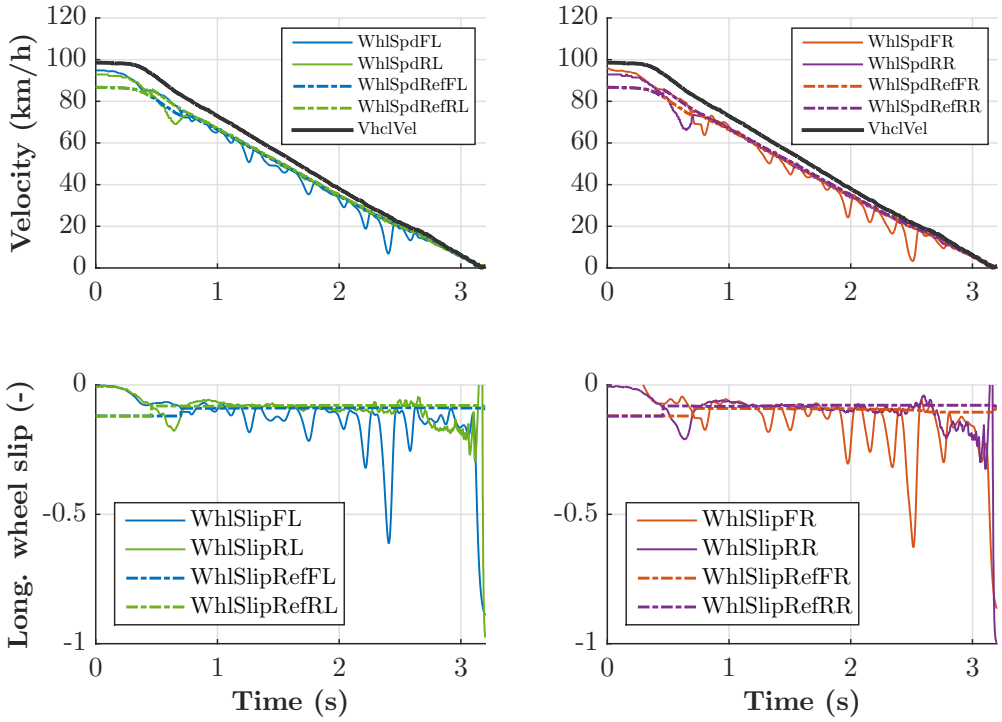

Fig. 6.17 Braking in high road friction conditions: PI control

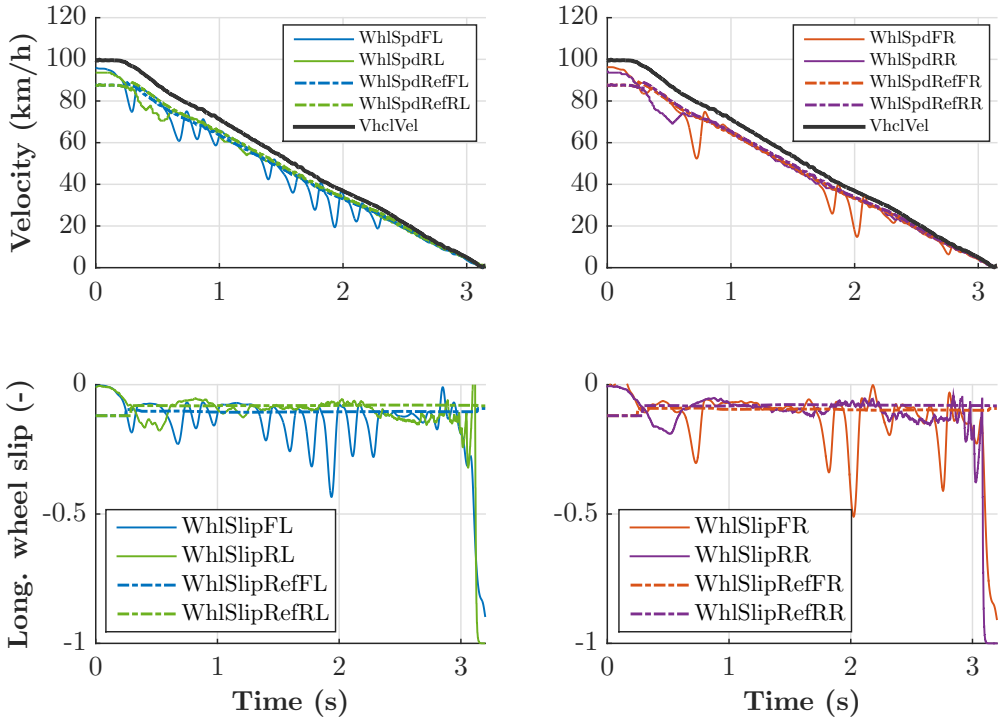

Fig. 6.18 Braking in high road friction conditions: sliding mode PI control

the road surface, where variation of the reference wheel slip produced by reference was from 0.09 up to 0.11 remaining most of the time at 0.1.

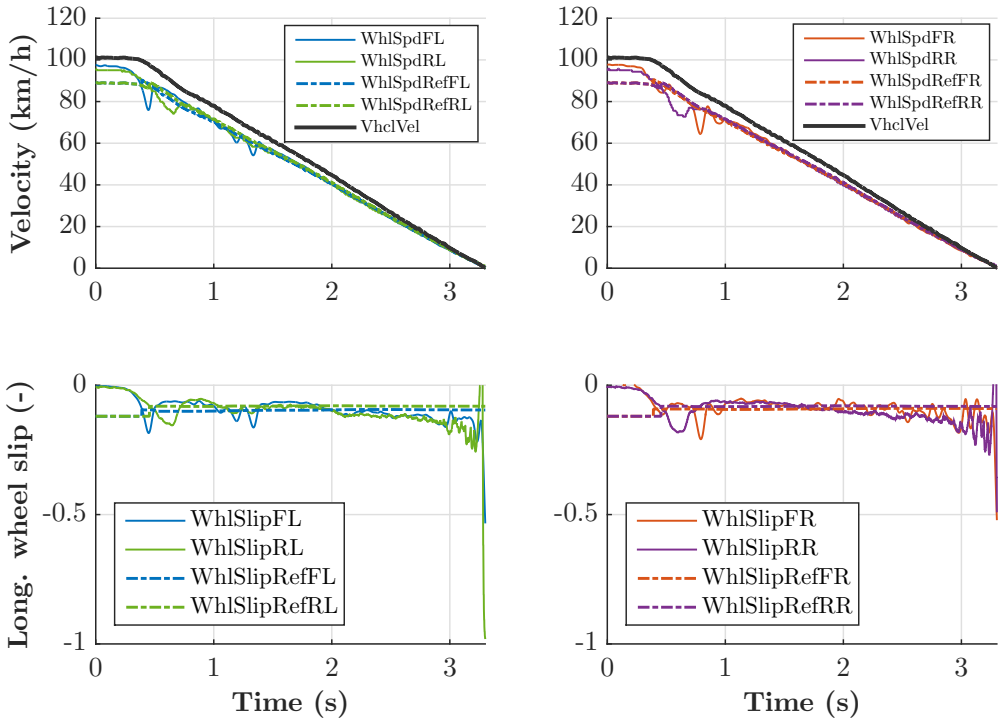

Fig. 6.19 Braking in high road friction conditions: integral sliding mode control

Obtained numerical assessment of developed WSC control strategies is summarized in Table G.2. Following conclusions can be drawn based on presented results evaluation:

- Developed continuous control strategies showed up to 31 % and 9 % braking distance reduction compared to the industrial rule-based approach in low and high road friction conditions, respectively;
- Developed continuous control strategies produced up to 55 % and 27 % better ride quality compared to the industrial rule-based approach in low and high road friction conditions, respectively;
- Applied reference adaptation strategy allows accurate identification of optimal wheel slip value, which allows reducing braking distance up to 3 %;
- PI, SMPI and ISM showed precise wheel slip tracking on low-μ road surface; however, PI and SMPI have oscillatory behavior in high road friction conditions, while ISM provides smooth and precise tracking;

- Developed controls were tested in closed-loop with velocity estimator and reference adaptation logic, which did not deteriorate system control performance.

Attractive properties of sliding-mode approaches and their effectiveness in application to WSC tasks motivated further investigation of these algorithms. For this purpose, vehicle with four individual IWMs was selected as experimental facility. Using IWM motors it is possible to assess pure effects from sliding-mode control algorithms due to their relatively high system bandwidth and quicker system reaction among other known brake system configurations. Next section present experimental comparison of PI, VSPI, ISM and CTA controls applied to WSC tasks.

6.5 Wheel slip control with in-wheel electric motors

Tests in low road friction conditions were performed with the vehicle demonstrator equipped with four individual IWMs (Section 6.1.3) to compare variable structure and sliding mode methods in application to WSC. Due to the track limitations, all tests were performed with initial velocity of 30 km/h. Plastic sheets continuously wetted by water sprinklers were used to provide low road friction with $\mu_{road} \approx 0.2$.

Compared to the simulation results, where FOSM produced significant chattering and higher deviation from the reference value, this effect was attenuated during road tests. Such high-frequency modulation of braking torque was not bypassed by tires, which have first-order order dynamics with lower cutoff frequency. This effect led to better tracking performance than in simulation, where transient tire dynamics were not experimentally validated for this type of vehicle. Among other control approaches, FOSM has the most agile reaction during initial phase of ABS activation and first peak for the front and rear wheels has the lowest value. Despite these advantages, FOSM still produces oscillatory torque behavior, which has negative influence on ride quality.

VSPI control showed the worst tracking performance for the front and rear wheels. Switching of the control gains at reference wheel slip point allows compensating difference in system dynamics. However, this leads to more oscillatory behavior of requested wheel torque. As a consequence, first peak has relatively high values and system oscillates with such amplitude during the whole braking event. Despite this fact, ride quality did not suffer from these oscillations, as they have relatively low modulation frequency.

Having PI control as the continuous control action, ISM approach has, however, much better results in terms of tracking performance and system adaptability compared to VSPI control. Such system adaptability was guaranteed by discrete control part responsible for

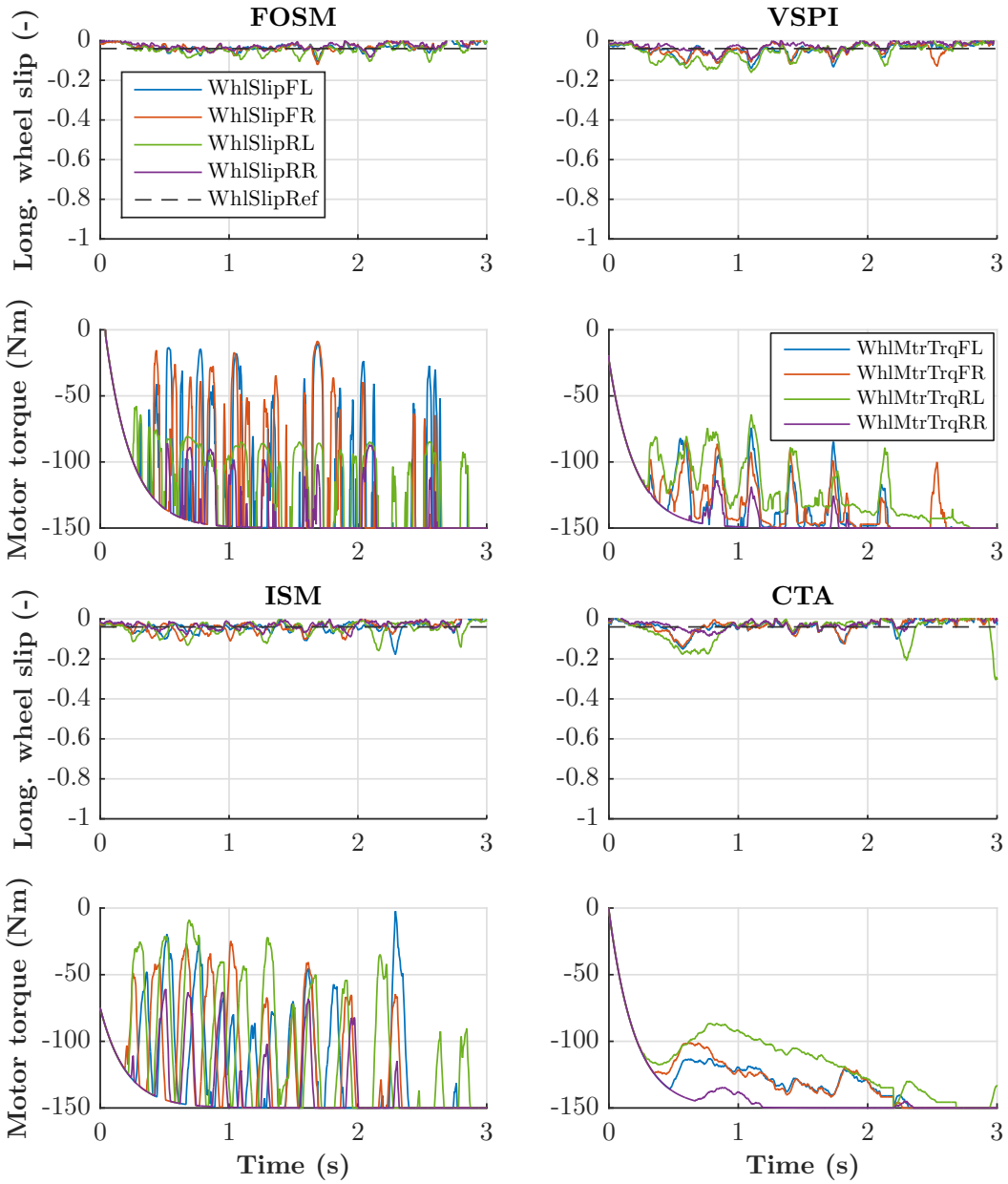

Fig. 6.20 Wheel slip control with in-wheel motors in low road friction conditions

disturbance rejection. ISM control provided ride quality comparable with VSPI and CTA approaches.

The most precise and smooth control action was produced by CTA algorithm due to the presence of integral control part and subsequent integration of virtual input. Theoretically this approach handles variation of the road conditions and vertical load during the emergency,

which was confirmed experimentally for this particular case. However, presence of the integral part leads to significantly slower system reaction at ABS activation stage. Hence, CTA has the highest first peak for front and rear wheels. Nevertheless, such progressive variation has huge benefits in terms of ride quality compared to torque modulation. As the results, CTA provides lowest longitudinal vehicle jerk during emergency braking.

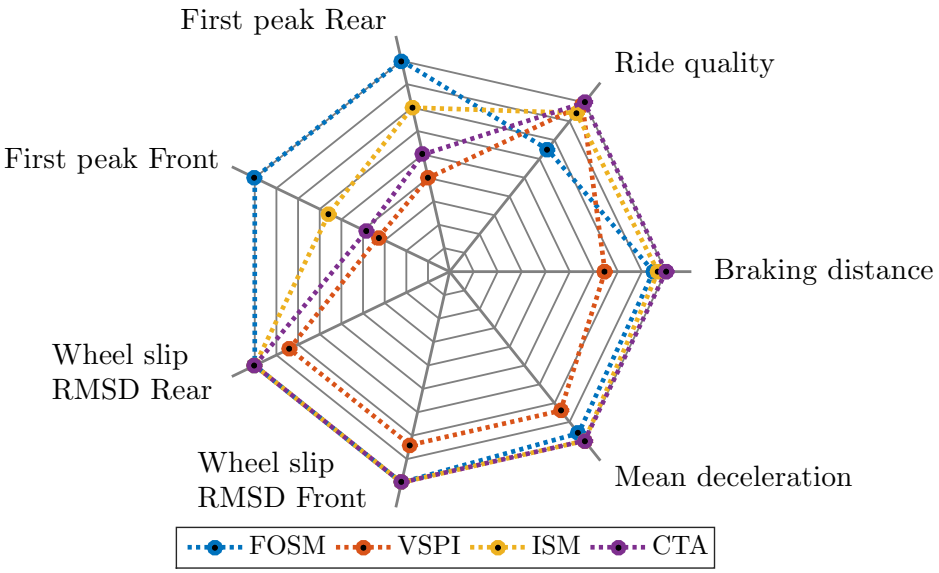

Fig. 6.21 Experimental comparison of developed WSC control strategies for the vehicle with IWMs

Results were summarized numerically in Table G.3 and presented as normalized criteria on the radar plot in Figure 6.21. Considering these results, following conclusions about investigated variable structure and sliding mode approaches can be drawn:

- FOSM has the most agile reaction in WSC mode providing the lowest first peak;
- Compared to the simulation results, FOSM braking torque was filtered by tire longitudinal dynamics, which resulted in precise wheel slip tracking;
- Chattering in FOSM produced high-frequency braking torque demand, which negatively influenced ride quality during the WSC braking;
- VSPI control produced the worst results in terms of control and braking performance due to more oscillatory brake torque demand modulation;
- CTA provides WSC solution applicable not only for IWMs, but also to brake actuators with slower dynamics; this is determined by smooth and progressive variation of the braking torque demand.

Chapter 7

Conclusions

Following contributions in the area of WSC control design were done by the author in the presented thesis:

- To perform simulation studies with developed WSC, mathematical models of longitudinal and lateral vehicle dynamics and chassis and powertrains systems were proposed and validated with experimental data. This also allowed developing state estimator using derived system's mathematical description.
- Approach on the tire dynamics parametrization using vehicle experimental data is provided to provide realistic tire dynamics in WSC mode in SIL and HIL experiments. This approach allowed shortening the calibration time for system's tuning during the road tests.
- Overall architecture of brake controller was proposed considering specified system requirements. In particular, this presents control solution for the brake systems of electric and automated vehicles.
- Brake blending strategy was developed for the vehicles with combined brake system architecture. Special focus has been given to the WSC mode guaranteeing stable system behavior independently from the type of used actuator.
- Continuous WSC was designed using PI control approach in combination with brake blending for the vehicle with combined DEHB and individual OBMs system. Obtained experimental results showed 20 % reduction of braking distance compared to the vehicle with conventional control and EHB system. Besides that, ride quality was significantly improved that shows applicability of this method for automated vehicles.

- Continuous WSC for the vehicle with DEHB was designed using PI and robust SM control methods: SMPI and ISM. The latter method produced up to 31 % and 9 % braking distance reduction compared to the industrial rule-based approach in low and high road friction conditions, respectively. Important to admit that this method allowed enhancing ride quality during WSC mode, which emphasizes benefits in using this method in application to automated vehicles.

- Vehicle state estimator was designed to provide necessary information for WSC and experimentally validated using tests with the vehicle demonstrators. Important to admit that this method does not require inclusion of parametrized tire model, which is advantageous over known approaches. Due to this fact, this method can be used for real-time estimation of typical tire characteristics.

- Reference wheel slip adaptation logic was proposed and showed accurate identification of wheel slip reference value in low and high road friction conditions. This method does not negatively influences control performance of WSC and allows further improvement of braking performance.

- Experimental analysis of VSPI, FOSM, ISM and CTA control methods in application to WSC allowed comparing these method in terms of control performance. Among considered control laws, CTA showed simultaneous improvement in braking performance and ride quality providing smooth and precise tracking of wheel slip without typical modulation of wheel torque. This method can find an application not only in vehicle with IWMs, but can be used with brake actuators with much slower system dynamics.

References

[1] B. Heißing and M. Ersoy, "Chassis Handbook: Fundamentals, Driving Dynamics, Components, Mechatronics, Perspectives (ATZ/MTZ-Fachbuch)," *Vieweg-Teubner Verlag*, pp. 61–63, 2011.

[2] H. Wallentowitz, A. Freialdenhoven, and I. Olschewski, "Technologietrends fahrwerk," *Strategien in der Automobilindustrie: Technologietrends und Marktentwicklungen*, pp. 177–199, 2009.

[3] P. E. Pfeffer, "Active chassis systems," *Auto Tech Review*, vol. 1, no. 7, pp. 26–31, 2012.

[4] R. D. Fruechte, A. M. Karmel, J. H. Rillings, N. A. Schilke, N. M. Boustany, and B. S. Repa, "Integrated vehicle control," in *Vehicular Technology Conference, 1989, IEEE 39th*, pp. 868–877, IEEE, 1989.

[5] R. Limpert, "Brake design and safety, warrendale, pa: Society of automotive engineers," 1999.

[6] R. B. GmbH., K. Reif, and K.-H. Dietsche, *Automotive handbook*. Robert Bosch GmbH, 2014.

[7] R. Isermann, *Fahrdynamik-Regelung: Modellbildung, Fahrerassistenzsysteme, Mechatronik*. Springer-Verlag, 2006.

[8] M. G. Patterson, "What is energy efficiency?: Concepts, indicators and methodological issues," *Energy policy*, vol. 24, no. 5, pp. 377–390, 1996.

[9] "Vehicle Dynamics Terminology," Standard SAE J670:200801, 2008.

[10] T. Armour, D. Allwright, C. Cawthorn, C. Dent, J. Dewynne, J. Fehribach, G. Fay, J. Lees-Miller, J. Ward, R. Whittaker, *et al.*, "Chauffeur braking," 2009.

[11] S. B. Choi, "Antilock brake system with a continuous wheel slip control to maximize the braking performance and the ride quality," *IEEE Transactions on Control Systems Technology*, vol. 16, no. 5, pp. 996–1003, 2008.

[12] A. Sharma, *Text book of elementary statistics*. Discovery Publishing House, 2005.

[13] R. Baun, "Das neue e-klasse t-modell von mercedes-benz," *ATZ-Automobiltechnische Zeitschrift*, vol. 105, no. 6, pp. 544–546, 2003.

[14] M.-Y. v. Hohenthal, "Enwicklung-Historisches: Mercedes SL–Mehr als ein halbes Jahrhundert offen fur Neues," *ATZ-Automobiltechnische Zeitschrift*, vol. 107, no. 4, pp. 308–319, 2005.

[15] J. Böhm, S. Stölzl, P. Willimowski, J. Nell, and R. Oehler, "Electromechanical brake system," Feb. 5 2002. US Patent 6,345,225.

[16] E. Katsuyama, "Decoupled 3d moment control using in-wheel motors," *Vehicle System Dynamics*, vol. 51, no. 1, pp. 18–31, 2013.

[17] D. Tavernini, E. Velenis, and S. Longo, "Model-based active brake force distribution for pitch angle minimization," in *Decision and Control (CDC), 2015 IEEE 54th Annual Conference on*, pp. 197–202, IEEE, 2015.

[18] A. Stevens and W. Penny, "Elektrische Bremse für Motorwagen," 1899. 121043.

[19] R. Schwarz, R. Isermann, J. Böhm, J. Nell, and P. Rieth, "Modeling and control of an electromechanical disk brake," tech. rep., SAE Technical Paper, 1998.

[20] M. Putz, B. Faul, C. Wunsch, and J. E. Morgan, "The ve electromechanical brake with fully integrated actuators in a suv class vehicle; vienna engineering; eurobrake 2012," tech. rep., EB2012-ABT-22.

[21] C. Jo, S. Lee, H. Song, Y. Cho, I. Kim, D. Hyun, and H. Kim, "Design and control of an upper-wedge-type electronic brake," *Proceedings of the Institution of Mechanical Engineers, Part D: Journal of Automobile Engineering*, vol. 224, no. 11, pp. 1393–1405, 2010.

[22] L. M. Ho, R. Roberts, H. Hartmann, and B. Gombert, "The electronic wedge brake-ewb," tech. rep., SAE Technical Paper, 2006.

[23] J. Fox, R. Roberts, C. Baier-Welt, L. M. Ho, L. Lacraru, and B. Gombert, "Modeling and control of a single motor electronic wedge brake," tech. rep., SAE Technical Paper, 2007.

[24] J. G. Kim, M. J. Kim, J. K. Kim, and K.-H. Noh, "Developing of electronic wedge brake with cross wedge," tech. rep., SAE Technical Paper, 2009.

[25] O. Kwon, D. Shin, and M. Kim, "Improvement of braking efficiency for electro-mechanical brake using double wedge structure," *KSAE07-G0014*, pp. 30–34, 2007.

[26] J. D. Carlson, D. F. LeRoy, J. C. Holzheimer, D. R. Prindle, and R. H. Marjoram, "Controllable brake," Dec. 1 1998. US Patent 5,842,547.

[27] K. Karakoc, *Design of a magnetorheological brake system based on magnetic circuit optimization*. PhD thesis, 2007.

[28] B. Assadsangabi, F. Daneshmand, N. Vahdati, M. Eghtesad, and Y. Bazargan-Lari, "Optimization and design of disk-type mr brakes," *International Journal of Automotive Technology*, vol. 12, no. 6, pp. 921–932, 2011.

[29] E. J. Park, D. Stoikov, L. F. da Luz, and A. Suleman, "A performance evaluation of an automotive magnetorheological brake design with a sliding mode controller," *Mechatronics*, vol. 16, no. 7, pp. 405–416, 2006.

[30] W.-D. Jonner, H. Winner, L. Dreilich, and E. Schunck, "Electrohydraulic brake system-the first approach to brake-by-wire technology," tech. rep., SAE Technical Paper, 1996.

[31] W. Achenbach and U. Stoll, "Weltneuheit bei den bremsen: Die sensotronic brake control (sbc)," *Der neue Mercedes SL. Sonderausgabe der Automobiltechnischen Zeitschrift (ATZ) und der Motortechnischen Zeitschrift (MTZ)*, vol. 103, no. Sonderheft, 2001.

[32] "Integriertes Bremssystem: elektronische Stabilitätskontrolle (ESC) und regeneratives System in einer einzigen, integrierten Einheit." https://www.zf.com/corporate/de_de/products/product_range/cars/cars_integrated_brake_control.shtml. Accessed: 2018-05-15.

[33] C. F. Lee, D. Savitski, C. Manzie, and V. Ivanov, "Active brake judder compensation using an electro-hydraulic brake system," *SAE International Journal of Commercial Vehicles*, vol. 8, no. 2015-01-0619, pp. 20–26, 2015.

[34] S. Semmler, *Regelung der Fahrzeugbremsdynamik mit kontinuierlich einstellbaren Radbremsen*. PhD thesis, TU Darmstadt, Düsseldorf, Januar 2006.

[35] D. Krehl, "Alternative antriebe sind nicht alternativlos," *MTZ - Motortechnische Zeitschrift*, vol. 2, pp. 6–7, 2014.

[36] C. Chatzikomis, A. Sorniotti, P. Gruber, M. Zanchetta, D. Willans, and B. Balcombe, "Comparison of Path Tracking and Torque-Vectoring Controllers for Autonomous Electric Vehicles," *IEEE Transactions on Intelligent Vehicles*, 2018.

[37] H. Winner, S. Hakuli, F. Lotz, and C. Singer, *Handbook of Driver Assistance Systems: Basic Information, Components and Systems for Active Safety and Comfort*. Springer Publishing Company, Incorporated, 2015.

[38] R. Bosch and P. T. Girling, *Automotive handbook*. Society of Automotive Engineers, US, 1996.

[39] S. Kerst, B. Shyrokau, and E. Holweg, "Anti-lock braking control based on bearing load sensing," *Proc. of EuroBrake2015, Dresden, Germany*, pp. 4–6, 2015.

[40] E. Suraci, P. Abagnale, D. Amoroso, and F. Mariniello, "Development and road tests of an abs control system," *Vehicle System Dynamics*, vol. 44, no. sup1, pp. 393–401, 2006.

[41] S. Murata, "Innovation by in-wheel-motor drive unit," *Vehicle System Dynamics*, vol. 50, no. 6, pp. 807–830, 2012.

[42] H. Fujimoto and K. Maeda, "Optimal yaw-rate control for electric vehicles with active front-rear steering and four-wheel driving-braking force distribution," in *Industrial Electronics Society, IECON 2013-39th Annual Conference of the IEEE*, pp. 6514–6519, IEEE, 2013.

[43] Y. Wang, H. Fujimoto, and S. Hara, "Driving force distribution and control for EV with four in-wheel motors: A case study of acceleration on split-friction surfaces," *IEEE Transactions on Industrial Electronics*, vol. 64, pp. 3380–3388, April 2017.

[44] H. Gao, X. Zhang, Y. Liu, and D. Li, "Longitudinal control for Mengshi autonomous vehicle via Gauss cloud model," *Sustainability*, vol. 9, no. 12, p. 2259, 2017.

[45] G. Xie, H. Gao, L. Qian, B. Huang, K. Li, and J. Wang, "Vehicle trajectory prediction by integrating physics-and maneuver-based approaches using interactive multiple models," *IEEE Transactions on Industrial Electronics*, 2017.

[46] H. Jing, Z. Liu, and H. Chen, "A switched control strategy for antilock braking system with on/off valves," *IEEE Transactions on Vehicular Technology*, vol. 60, no. 4, pp. 1470–1484, 2011.

[47] J. J. Castillo, J. A. Cabrera, A. J. Guerra, and A. Simón, "A novel electrohydraulic brake system with tire–road friction estimation and continuous brake pressure control," *IEEE Transactions on Industrial Electronics*, vol. 63, no. 3, pp. 1863–1875, 2016.

[48] S. Drakunov, U. Ozguner, P. Dix, and B. Ashrafi, "ABS control using optimum search via sliding modes," *IEEE Transactions on Control Systems Technology*, vol. 3, no. 1, pp. 79–85, 1995.

[49] M. Amodeo, A. Ferrara, R. Terzaghi, and C. Vecchio, "Wheel slip control via second-order sliding-mode generation," *IEEE Transactions on Intelligent Transportation Systems*, vol. 11, pp. 122–131, March 2010.

[50] Y. W. Liang, C. C. Chen, D. C. Liaw, and Y. T. Wei, "Nonlinear reliable control with application to a vehicle antilock brake system," *IEEE Transactions on Industrial Informatics*, vol. 9, pp. 2114–2123, Nov 2013.

[51] R. de Castro, R. E. Araùjo, and D. Freitas, "Wheel slip control of EVs based on sliding mode technique with conditional integrators," *IEEE Transactions on Industrial Electronics*, vol. 60, pp. 3256–3271, Aug 2013.

[52] T. Shim, S. Chang, and S. Lee, "Investigation of sliding-surface design on the performance of sliding mode controller in antilock braking systems," *IEEE Transactions on Vehicular Technology*, vol. 57, pp. 747–759, March 2008.

[53] M. Tanelli and A. Ferrara, "Enhancing robustness and performance via switched second order sliding mode control," *IEEE Transactions on Automatic Control*, vol. 58, pp. 962–974, April 2013.

[54] E. Kayacan, Y. Oniz, and O. Kaynak, "A grey system modeling approach for sliding-mode control of antilock braking system," *IEEE Transactions on Industrial Electronics*, vol. 56, pp. 3244–3252, Aug 2009.

[55] K. Berntorp, "Joint wheel-slip and vehicle-motion estimation based on inertial, GPS, and wheel-speed sensors," *IEEE Transactions on Control Systems Technology*, vol. 24, pp. 1020–1027, May 2016.

[56] W. Y. Wang, I. H. Li, M. C. Chen, S. F. Su, and S. B. Hsu, "Dynamic slip-ratio estimation and control of antilock braking systems using an observer-based direct adaptive fuzzy-neural controller," *IEEE Transactions on Industrial Electronics*, vol. 56, pp. 1746–1756, May 2009.

[57] D. Nesic, A. Mohammadi, and C. Manzie, "A framework for extremum seeking control of systems with parameter uncertainties," *IEEE Transactions on Automatic Control*, vol. 58, pp. 435–448, Feb 2013.

[58] C. Lee, K. Hedrick, and K. Yi, "Real-time slip-based estimation of maximum tire-road friction coefficient," *IEEE/ASME Transactions on Mechatronics*, vol. 9, pp. 454–458, June 2004.

[59] S. Semmler, "Regelung der Fahrzeugbremsdynamik mit kontinuierlich einstellbaren Radbremsen," *Fortschritt Berichte-VDI Reihe 12 Verkehrstechnik Fahrzeugtechnik*, vol. 632, 2006.

[60] Z. Qi, S. Taheri, B. Wang, and H. Yu, "Estimation of the tyre-road maximum friction coefficient and slip slope based on a novel tyre model," *Vehicle System Dynamics*, vol. 53, no. 4, pp. 506–525, 2015.

[61] "Regulation (EEC) No 4064/89 merger procedure," tech. rep., 17/03/1999.

[62] P. Sapun, "Passenger cars report 2017 – Small SUVs," tech. rep., Statista, 2017.

[63] ICCT, "European vehicle market statistics - pocketbook 2017/18," tech. rep., The International Council on Clean Transportation, 2017.

[64] S. C. Davis and L. F. Truett, "An analysis of the impact of sport utility vehicles in the united states," tech. rep., Oak Ridge National Laboratory, 2000.

[65] S. Gunster, "'You belong outside': Advertising, nature, and the SUV," *Ethics & the Environment*, vol. 9, no. 2, pp. 4–32, 2004.

[66] B.-C. Chen and H. Peng, "Differential-braking-based rollover prevention for sport utility vehicles with human-in-the-loop evaluations," *Vehicle System Dynamics*, vol. 36, no. 4-5, pp. 359–389, 2001.

[67] J. Mayrose and D. V. Jehle, "Vehicle weight and fatality risk for sport utility vehicle versus passenger car crashes," *Journal of Trauma and Acute Care Surgery*, vol. 53, no. 4, pp. 751–753, 2002.

[68] F. An, D. Gordon, H. He, D. Kodjak, and D. Rutherford, "Passenger vehicle greenhouse gas and fuel economy standards: a global update," *The international council on clean transportation, Washington DC*, 2007.

[69] T. Lieven, S. Mühlmeier, S. Henkel, and J. F. Waller, "Who will buy electric cars? an empirical study in germany," *Transportation Research Part D: Transport and Environment*, vol. 16, no. 3, pp. 236–243, 2011.

[70] International Council on Clean Transportation Europe, "European vehicle market statistics - Pocketbook 2017/18," 2017.

[71] "Electric-VEhicle Control of individual wheel Torque for On- and Off-Road Conditions (E-VECTOORC)." https://cordis.europa.eu/project/rcn/99412_en.html. Accessed: 2018-05-13.

[72] "Innovative Engineering of Ground Vehicles with Integrated Active Chassis Systems (EVE)." https://cordis.europa.eu/project/rcn/194375_en.html. Accessed: 2018-05-13.

[73] "Robust Control, State Estimation and Disturbance Compensation for Highly Dynamic Environmental Mechatronic Systems (CLOVER)." https://cordis.europa.eu/project/rcn/206521_en.html. Accessed: 2018-05-13.

[74] C. Ghike and T. Shim, "14 degree-of-freedom vehicle model for roll dynamics study," no. 2006-01-1277, 2006.

[75] L. Louis and D. Schramm, "Nonlinear state estimation of tire-road contact forces using a 14 dof vehicle model," in *Applied mechanics and materials*, vol. 165, pp. 155–159, Trans Tech Publ, 2012.

[76] F. Cheli, A. Concas, E. Giangiulio, and E. Sabbioni, "A simplified abs numerical model: Comparison with hil and full scale experimental tests," *Computers & Structures*, vol. 86, no. 13-14, pp. 1494–1502, 2008.

[77] M. Doumiati, A. Charara, A. Victorino, and D. Lechner, *Vehicle Dynamics Estimation using Kalman Filtering: Experimental Validation*. John Wiley & Sons, 2012.

[78] B. Ganzel, "Slip control boost braking system," Dec. 29 2015. US Patent 9,221,443.

[79] R. Rajamani, G. Phanomchoeng, D. Piyabongkarn, and J. Y. Lew, "Algorithms for real-time estimation of individual wheel tire-road friction coefficients," *IEEE/ASME Transactions on Mechatronics*, vol. 17, pp. 1183–1195, Dec 2012.

[80] M. Salman, "A robust servo-electronic controller for brake force distribution," *Journal of Dynamic Systems, Measurement, and Control*, vol. 112, no. 3, pp. 442–447, 1990.

[81] M. Kuang, M. Fodor, D. Hrovat, and M. Tran, "Hydraulic brake system modeling and control for active control of vehicle dynamics," in *American Control Conference, 1999. Proceedings of the 1999*, vol. 6, pp. 4538–4542, IEEE, 1999.

[82] D. Savitski, B. Shyrokau, and V. Ivanov, "Base-brake functions of electric vehicle: disturbance compensation in decoupled brake system," *International Journal of Vehicle Design*, vol. 70, no. 1, pp. 69–97, 2016.

[83] V. Ricciardi, D. Savitski, K. Augsburg, and V. Ivanov, "Estimation of brake friction coefficient for blending function of base braking control," *SAE International Journal of Passenger Cars-Mechanical Systems*, vol. 10, no. 2017-01-2520, pp. 774–785, 2017.

[84] F. Bottiglione, A. Sorniotti, and L. Shead, "The effect of half-shaft torsion dynamics on the performance of a traction control system for electric vehicles," *Proceedings of the Institution of Mechanical Engineers, Part D: Journal of Automobile Engineering*, vol. 226, no. 9, pp. 1145–1159, 2012.

[85] R. A. Krenz, "Vehicle response to throttle tip-in/tip-out," tech. rep., SAE Technical Paper, 1985.

[86] "Stepwise Coastdown Methodology for Measuring Tire Rolling Resistance," Standard SAE J2452:2017, 2017.

[87] K. Höpping, K. Augsburg, and F. Büchner, "Extending the magic formula tire model for large inflation pressure changes by using measurement data from a corner module test rig," vol. 11, 03 2018.

[88] D. Savitski, D. Schleinin, V. Ivanov, K. Augsburg, E. Jimenez, R. He, C. Sandu, and P. Barber, "Improvement of traction performance and off-road mobility for a vehicle with four individual electric motors: Driving over icy road," *Journal of Terramechanics*, vol. 69, pp. 33–43, 2017.

[89] M. W. Sayers and D. Han, "A generic multibody vehicle model for simulating handling and braking," *Vehicle system dynamics*, vol. 25, no. S1, pp. 599–613, 1996.

[90] P. W. A. Zegelaar, "The dynamic response of tyres to brake torque variations and road unevennesses," 1998.

[91] G. Rill, *Road vehicle dynamics: Fundamentals and modeling*. CRC Press, 2011.

[92] E. Giangiulio and D. Arosio, "Vehicle, road, tire and electronic control system interaction - prediction and validation of handling behaviour," in *Tire technology conference*, 2006.

[93] "Passenger cars – Steady-state circular driving behaviour – Open-loop test methods," Standard ISO 4138:2004, 2004.

[94] "Road vehicles - Lateral transient response test methods - Open-loop test methods," Standard ISO 7401:2003, 2003.

[95] "Passenger cars - Stopping distance at straight-line braking with ABS - Open-loop test method," Standard ISO 21994:2007, 2007.

[96] K. M. Marshek, J. F. Cuderman, and M. J. Johnson, "Performance of anti-lock braking system equipped passenger vehicles-part ii: Braking as a function of initial vehicle speed in braking maneuver," tech. rep., SAE Technical Paper, 2002.

[97] M. Zirkel, *Einsetzung von Videosensoren für die Fahrzustandsschätzung und aktive Fahrsicherheitssysteme am Fahrzeug*. Master's thesis, 2018.

[98] D. G. Luenberger, "Observing the state of a linear system," *IEEE transactions on military electronics*, vol. 8, no. 2, pp. 74–80, 1964.

[99] R. Kalman, "On the general theory of control systems," *IRE Transactions on Automatic Control*, vol. 4, no. 3, pp. 110–110, 1959.

[100] K. Ogata and Y. Yang, *Modern control engineering*, vol. 4. Prentice hall India, 2002.

[101] S. Antonov, A. Fehn, and A. Kugi, "Unscented kalman filter for vehicle state estimation," *Vehicle System Dynamics*, vol. 49, no. 9, pp. 1497–1520, 2011.

[102] U. Kiencke and L. Nielsen, *Automotive control systems: for engine, driveline, and vehicle*. IOP Publishing, 2000.

[103] L. Imsland, T. A. Johansen, T. I. Fossen, H. F. Grip, J. C. Kalkkuhl, and A. Suissa, "Vehicle velocity estimation using nonlinear observers," *Automatica*, vol. 42, no. 12, pp. 2091–2103, 2006.

[104] M. Klomp, Y. Gao, and F. Bruzelius, "Longitudinal velocity and road slope estimation in hybrid electric vehicles employing early detection of excessive wheel slip," *Vehicle System Dynamics*, vol. 52, no. sup1, pp. 172–188, 2014.

[105] S. Gramstat, *Methoden der in-situ Visualisierung der Reibzonendynamik trockenlaufender Reibpaarungen unter Ergänzung physikalischer und chemischer Charakterisierungen der Reibpartner / Sebastian Gramstat*. 2015.

[106] N. D'alfio, A. Morgando, and A. Sorniotti, "Electro-hydraulic brake systems: design and test through hardware-in-the-loop simulation," *Vehicle System Dynamics*, vol. 44, no. sup1, pp. 378–392, 2006.

[107] J. Sendler, *Untersuchungen zur ergonomiegerechten Gestaltung der Mensch-Maschine-Schnittstellen von aktuellen Pkw-Bremsanlagen*. 2012.

[108] R. Trutschel, *Analytische und experimentelle Untersuchung der Mensch-Maschine-Schnittstellen von Pkw-Bremsanlagen*. 2007.

[109] "Braking of passenger cars," UN Regulation No. 13-H, 2014.

[110] D. Savitski, "Brake system design for semi-trailer truck with full-weight of 26 tons. Investigation of ABS operation.," May 2006.

[111] J. M. Rodriguez, R. Meneses, and J. Orus, "Active vibration control for electric vehicle compliant drivetrains," in *Industrial Electronics Society, IECON 2013-39th Annual Conference of the IEEE*, pp. 2590–2595, IEEE, 2013.

[112] S. M. Savaresi and M. Tanelli, *Active braking control systems design for vehicles*. Springer Science & Business Media, 2010.

[113] S. De Pinto, C. Chatzikomis, A. Sorniotti, and G. Mantriota, "Comparison of traction controllers for electric vehicles with on-board drivetrains," *IEEE Transactions on Vehicular Technology*, vol. 66, no. 8, pp. 6715–6727, 2017.

[114] T. A. Johansen, I. Petersen, J. Kalkkuhl, and J. Ludemann, "Gain-scheduled wheel slip control in automotive brake systems," *IEEE Transactions on Control Systems Technology*, vol. 11, no. 6, pp. 799–811, 2003.

[115] D. Savitski, V. Ivanov, K. Augsburg, B. Shyrokau, R. Wragge-Morley, T. Pütz, and P. Barber, "The new paradigm of an anti-lock braking system for a full electric vehicle: experimental investigation and benchmarking," *Proceedings of the Institution of Mechanical Engineers, Part D: Journal of Automobile Engineering*, vol. 230, no. 10, pp. 1364–1377, 2016.

[116] V. I. Utkin, *Sliding modes in control and optimization*. Springer Science & Business Media, 2013.

[117] V. Utkin and J. Shi, "Integral sliding mode in systems operating under uncertainty conditions," in *Decision and Control, 1996., Proceedings of the 35th IEEE Conference on*, vol. 4, pp. 4591–4596, IEEE, 1996.

[118] V. I. Utkin, "First stage of vss: people and events," in *Variable structure systems: towards the 21st century*, pp. 1–32, Springer, 2002.

[119] J. Dávila, L. Fridman, and A. Ferrara, "Introduction to sliding mode control," *Sliding Mode Control of Vehicle Dynamics*, p. 1, 2017.

[120] G. Ambrosino, G. Celentano, and F. Garofalo, "Robust model tracking control for a class of nonlinear plants," *IEEE Transactions on Automatic Control*, vol. 30, no. 3, pp. 275–279, 1985.

[121] D. Efimov, A. Polyakov, L. Fridman, W. Perruquetti, and J.-P. Richard, "Delayed sliding mode control," *Automatica*, vol. 64, pp. 37–43, 2016.

[122] V. Torres-González, L. M. Fridman, and J. A. Moreno, "Continuous twisting algorithm," in *Decision and Control (CDC), 2015 IEEE 54th Annual Conference on*, pp. 5397–5401, IEEE, 2015.

[123] A. Pisano, "Second order sliding modes: Theory and applications," *Universita Studi di Cagliari, Disseration*, 2000.

[124] G. P. Incremona, E. Regolin, A. Mosca, and A. Ferrara, "Sliding mode control algorithms for wheel slip control of road vehicles," in *American Control Conference (ACC), 2017*, pp. 4297–4302, IEEE, 2017.

[125] M. Tanelli, L. Piroddi, and S. M. Savaresi, "Real-time identification of tire–road friction conditions," *IET control theory & applications*, vol. 3, no. 7, pp. 891–906, 2009.

[126] I. Juga, P. Nurmi, and M. Hippi, "Statistical modelling of wintertime road surface friction," *Meteorological Applications*, vol. 20, no. 3, pp. 318–329, 2013.

[127] "Tesla Model 3 shows 60-0 mph braking weakness in CR tests, Tesla fires back with own test results." https://electrek.co/2018/05/21/tesla-model-3-braking-weakness-cr-tests-tesla-denies/. Accessed: 2018-06-22.

[128] V. Ivanov, B. Shyrokau, D. Savitski, K. Augsburg, J. Orus, J.-M. Rodriguez-Fortun, R. Meneses, J. Theunissen, K. Janssen, and D. Steenbeke, "System und Verfahren zur Antriebs- und Bremsmomentregelung in Elektrofahrzeugen mit Einzelradantrieb," 03 2014. DE 102014003992A1.

[129] V. Ivanov, D. Savitski, K. Augsburg, P. Barber, B. Knauder, and J. Zehetner, "Wheel slip control for all-wheel drive electric vehicle with compensation of road disturbances," *Journal of Terramechanics*, vol. 61, pp. 1–10, 2015.

[130] "Lommel Proving Ground." http://www.fordlpg.com. Accessed: 2018-05-15.

[131] H. Fujimoto and S. Harada, "Model-based range extension control system for electric vehicles with front and rear driving-braking force distributions," *IEEE Transactions on Industrial Electronics*, vol. 62, no. 5, pp. 3245–3254, 2015.

Appendix A

State estimation

Random walk process

$$\begin{bmatrix} \dot{x}_1 \\ \dot{x}_2 \end{bmatrix} = \begin{bmatrix} 0 & 1 \\ 0 & 0 \end{bmatrix} \begin{bmatrix} x_1 \\ x_2 \end{bmatrix} \tag{A.1}$$

Longitudinal and lateral tire forces, sideslip angle observer

State matrix:

$$A = \begin{bmatrix} 1 & 0 & 0 & 0 & 0 & 0 & 0 & 0 & 0 & 0 & 0 & 0 \\ 0 & 1 & 0 & 0 & 0 & 0 & 0 & 0 & 0 & 0 & 0 & 0 \\ 0 & 0 & 1 & 0 & 0 & 0 & 0 & 0 & 0 & 0 & 0 & 0 \\ 0 & 0 & 0 & 1 & 0 & 0 & 0 & 0 & 0 & 0 & 0 & 0 \\ a_{4,1} & 0 & 0 & 0 & 1 & 0 & 0 & 0 & 0 & 0 & 0 & 0 \\ 0 & a_{5,2} & 0 & 0 & 0 & 1 & 0 & 0 & 0 & 0 & 0 & 0 \\ 0 & 0 & a_{6,3} & 0 & 0 & 0 & 1 & 0 & 0 & 0 & 0 & 0 \\ 0 & 0 & 0 & a_{7,4} & 0 & 0 & 0 & 1 & 0 & 0 & 0 & 0 \\ 0 & 0 & 0 & 0 & 0 & 0 & 0 & 0 & 1 & 0 & 0 & 0 \\ 0 & 0 & 0 & 0 & 0 & 0 & 0 & 0 & 0 & 1 & 0 & 0 \\ a_{11,1} & a_{11,2} & 0 & 0 & 0 & 0 & 0 & 0 & a_{11,9} & a_{11,10} & 1 & a_{11,12} \\ a_{12,1} & a_{12,2} & a_{12,3} & a_{12,4} & 0 & 0 & 0 & 0 & a_{11,9} & a_{12,10} & 0 & 1 \end{bmatrix} \tag{A.2}$$

where the non-zero and non-singular terms

$a_{4,1} = -T_s \frac{r_w}{J_w}$, $a_{5,2} = -T_s \frac{r_w}{J_w}$, $a_{6,3} = -T_s \frac{r_w}{J_w}$, $a_{7,4} = -T_s \frac{r_w}{J_w}$,

$a_{11,1} = T_s \frac{sin(\delta)}{m_v}$, $a_{11,2} = T_s \frac{sin(\delta)}{m_v}$, $a_{11,10} = T_s \frac{1}{m_v}$, $a_{11,9} = T_s \frac{cos(\delta)}{m_v}$,

$a_{11,12} = -T_s V_x$ $a_{12,1} = T_s \frac{l_f sin(delta) + \frac{t_f}{2} cos(\delta)}{I_{zz}}$, $a_{12,2} = T_s \frac{l_f sin(\delta) - \frac{t_f}{2} cos(\delta)}{I_{zz}}$,

$a_{12,3} = -T_s \frac{t_r}{2I_{zz}}$, $a_{12,4} = T_s \frac{t_r}{2I_{zz}}$, $a_{12,9} = T_s \left(\frac{l_f * cos(delta)}{I_{zz}} + \frac{t_f}{2} \frac{sin(delta)}{I_{zz}} \right)$, $a_{12,10} = -T_s \frac{l_r}{I_{zz}}$.
Input matrix:

$$B = \begin{bmatrix} 0 & 0 & 0 & 0 \\ 0 & 0 & 0 & 0 \\ 0 & 0 & 0 & 0 \\ 0 & 0 & 0 & 0 \\ T_s \frac{1}{J_w} & 0 & 0 & 0 \\ 0 & T_s \frac{1}{J_w} & 0 & 0 \\ 0 & 0 & T_s \frac{1}{J_w} & 0 \\ 0 & 0 & 0 & T_s \frac{1}{J_w} \\ 0 & 0 & 0 & 0 \\ 0 & 0 & 0 & 0 \\ 0 & 0 & 0 & 0 \\ 0 & 0 & 0 & 0 \end{bmatrix} \tag{A.3}$$

Output matrix:

$$C = \begin{bmatrix} \frac{cos\delta}{m_v} & \frac{cos\delta}{m_v} & \frac{1}{m_v} & \frac{1}{m_v} & 0 & 0 & 0 & 0 & \frac{cos(\delta)}{m_v} & 0 & 0 & 0 & & & \\ 0 & 0 & 0 & 0 & 1 & 0 & 0 & 0 & 0 & 0 & 0 & 0 & 0 & 0 & 0 \\ 0 & 0 & 0 & 0 & 0 & 1 & 0 & 0 & 0 & 0 & 0 & 0 & 0 & 0 & 0 \\ 0 & 0 & 0 & 0 & 0 & 0 & 1 & 0 & 0 & 0 & 0 & 0 & 0 & 0 & 0 \\ 0 & 0 & 0 & 0 & 0 & 0 & 0 & 1 & 0 & 0 & 0 & 0 & 0 & 0 & 0 \\ \frac{sin\delta}{m_v} & \frac{sin\delta}{m_v} & 0 & 0 & 0 & 0 & 0 & 0 & \frac{cos\delta}{m_v} & \frac{1}{m_v} & 0 & 0 & 0 & 0 & 0 \\ 0 & 0 & 0 & 0 & 0 & 0 & 0 & 0 & 0 & 0 & 0 & 0 & 0 & 0 & 1 \end{bmatrix} \tag{A.4}$$

Vertical tire forces observer

Output matrix:

$$C = \begin{bmatrix} T_s & 0 & 0 & 0 & 0 & 0 & 0 & 0 & 0 \\ 0 & 0 & 0 & 0 & 1 & 0 & 0 & 0 & 0 \\ 0 & 0 & 0 & 0 & 0 & 0 & 1 & 0 & 0 \\ 1 & 1 & 1 & 1 & 0 & 0 & 0 & 0 & 0 \end{bmatrix} \tag{A.5}$$

State matrix:

$$A = \begin{bmatrix} 1 & 0 & 0 & 0 & 0 & -T_s m_v \frac{h_c}{2L} & 0 & -T_s m_v \frac{h_c l_r}{t_f L} & 0 \\ 0 & 0 & 0 & 0 & 0 & -T_s m_v \frac{h_c}{2L} & 0 & T_s m_v \frac{h_c l_r}{t_f L} & 0 \\ 0 & 0 & 0 & 0 & 0 & T_s m_v \frac{h_c}{2L} & 0 & -T_s m_v \frac{h_c l_f}{t_r L} & 0 \\ 0 & 0 & 0 & 0 & 0 & T_s m_v \frac{h_c}{2L} & 0 & T_s m_v \frac{h_c l_f}{t_r L} & 0 \\ 0 & 0 & 0 & 0 & 1 & T_s & 0 & 0 & 0 \\ 0 & 0 & 0 & 0 & 0 & 1 & 0 & 0 & 0 \\ 0 & 0 & 0 & 0 & 0 & 0 & 1 & T_s & 0 \\ 0 & 0 & 0 & 0 & 0 & 0 & 0 & 1 & 0 \\ 0 & 0 & 0 & 0 & 0 & 0 & 0 & 0 & 1 \end{bmatrix} \tag{A.6}$$

Appendix B

Reference wheel slip adaptation

Procedure 1 Seeking for optimal reference wheel slip λ^*

Require: Brake pedal travel s_{ped}, wheel slip $\lambda_w^{ij}(t)$, estimated wheel force $\hat{F}_x(t)$, estimated slope sign $sign(\nabla f) = sign\left(\frac{\partial \hat{F}_x}{\partial \lambda}\right)$.

Ensure: Reference wheel slip $\lambda^* \hat{=} max\{F_x(\lambda)\}$, $\forall \lambda \in [0,1]$.

1: Initial value $\lambda^{*,ij} = \lambda_{init}$ corresponds to the higher values of wheel slip to avoid fault-interaction of WSC.
2: Peak detection to activate WSC:
3: **if** $s_{ped} > 1$ mm & $\lambda^{ij} > \lambda_{lim}$ & $sgn(\nabla f_k^{ij}) \neq sgn(\nabla f_{k-1}^{ij})$ **then**
4: $\quad \lambda_k^{*,ij} = \frac{1}{k-n} \sum_{i=k-n}^{k} \lambda^{ij}(i)$
5: $\quad \lambda_{d,k}^{ij} = \lambda_k^{*,ij}$
6: **else**
7: $\quad \lambda_k^{*,ij} = \lambda_{k-1}^{*,ij}$
8: **end if**
9: After WSC activation, $\lambda^{*,ij}$ is progressively adapted:
10: **if** $s_{ped} > 1$ mm & $\lambda > \lambda_{lim}$ & $sgn(\nabla f_k) \neq sgn(\nabla f_{k-1})$ & $|\lambda_k - \lambda_k^{*,ij}| < \lambda_{e,lim}$ **then**
11: $\quad \lambda_{d,k}^{ij} = \frac{1}{k-n} \sum_{i=k-n}^{k} \lambda^{ij}(i)$
12: $\quad \lambda_k^{*,ij} = \lambda_{k-1}^{*,ij} + K_\lambda \int_{t_{k-1}}^{t_k} \left(\lambda_{d,k}^{ij} - \lambda_{k-1}^{*,ij}\right)$
13: **else**
14: $\quad \lambda_k^{*,ij} = \lambda_{k-1}^{*,ij} + K_\lambda \int_{t_{k-1}}^{t_k} \left(\lambda_{d,k}^{ij} - \lambda_{k-1}^{*,ij}\right)$
15: **end if**
16: Apply $\lambda^{*,ij}$ to WSC.

Appendix C

Linear on-board electric powertrain model

State vector:

$$X = \begin{bmatrix} \dot{\theta}_{em} & \theta_{em} & \dot{\theta}_{w} & \theta_{w} & T_{em} \end{bmatrix} \tag{C.1}$$

Input vector:

$$U = T_{em} \tag{C.2}$$

State matrix:

$$A = \begin{bmatrix} -\frac{\beta_{hs} i_g^2}{J_{hs} \eta_{cvj}} & -\frac{k_{hs} i_g^2}{J_{hs} \eta_{cvj}} & \frac{\beta_{hs} i_g}{J_{hs} \eta_{cvj}} & \frac{k_{hs} i_g}{J_{hs} \eta_{cvj}} & \frac{1}{J_{hs}} \\ 1 & 0 & 0 & 0 & 0 \\ \frac{\beta_{hs} i_g}{J_w} & \frac{k_{hs} i_g}{J_w} & -\frac{\beta_{hs}}{J_w} & -\frac{k_{hs}}{J_w} & 0 \\ 0 & 0 & 1 & 0 & 0 \\ -K_{AVC} \frac{i_g}{\tau_{em}} & 0 & K_{AVC} \frac{1}{\tau_{em}} & 0 & -\frac{1}{\tau_{em}} \end{bmatrix} \tag{C.3}$$

where $i_g = i_{g,1} i_{g,2}$

Input matrix:

$$B = \begin{bmatrix} 0 \\ 0 \\ 0 \\ 0 \\ \frac{1}{\tau_{em}} \end{bmatrix} \tag{C.4}$$

Appendix D

Numerical assessment of simulation results

Table D.1 WSC numerical evaluation for the braking in low friction conditions with IWMs

Evaluation criterion	RB	FOSM	VSPI	ISM	CTA
Wheel slip FL RMSD, (-)	-	0.03	0.03	0.01	0.01
Wheel slip FR RMSD, (-)	-	0.04	0.03	0.01	0.01
Wheel slip RL RMSD, (-)	-	0.03	0.03	0.01	0.01
Wheel slip RR RMSD, (-)	-	0.03	0.03	0.01	0.01
Wheel slip first peak FL, (-)	0.45	0.06	0.13	0.08	0.09
Wheel slip first peak FR, (-)	0.42	0.05	0.13	0.09	0.09
Wheel slip first peak RL, (-)	0.27	0.06	0.15	0.11	0.10
Wheel slip first peak RR, (-)	0.38	0.06	0.17	0.11	0.11
Braking distance, (m)	23.2	23.7	21.0	20.9	20.9
WSCIP, (-)	1	0.9	1.1	1.1	1.1
Jerk STD, (m/s^3)	2.3	4.7	0.4	0.4	0.4

Table D.2 WSC numerical evaluation for various reference wheel slip values: vehicle with on-board electric motors and decoupled-electro-hydraulic brake system

		Low road friction		High road friction	
Evaluation criterion	λ^*	RB	PI	RB	PI
Wheel slip FL RMSD, (-)	0.02	-	0.01	-	0.01
	0.04	-	0.01	-	0.01
	0.1	-	0.01	-	0.01
	0.15	-	0.01	-	0.02
	0.25	-	0.01	-	0.03
Wheel slip FR RMSD, (-)	0.02	-	0.01	-	0.01
	0.04	-	0.01	-	0.01
	0.1	-	0.02	-	0.01
	0.15	-	0.02	-	0.01
	0.25	-	0.01	-	0.03
Wheel slip RL RMSD, (-)	0.02	-	0.01	-	0.01
	0.04	-	0.01	-	0.01
	0.1	-	0.01	-	0.01
	0.15	-	0.01	-	0.02
	0.25	-	0.01	-	0.04
Wheel slip RR RMSD, (-)	0.02	-	0.01	-	0.01
	0.04	-	0.01	-	0.01
	0.1	-	0.01	-	0.01
	0.15	-	0.01	-	0.02
	0.25	-	0.02	-	0.04
Wheel slip first peak FL, (-)	0.02	-	0.10	-	0.04
	0.04	0.42	0.11	-	0.06
	0.1	-	0.17	0.63	012
	0.15	-	0.23	-	0.18
	0.25	-	0.32	-	0.29
Wheel slip first peak FR, (-)	0.02	-	0.10	-	0.04
	0.04	0.40	0.12	-	0.06
	0.1	-	0.18	0.63	0.12
	0.15	-	0.23	-	0.18
	0.25	-	0.32	-	0.29
Wheel slip first peak RL, (-)	0.02	-	0.06	-	0.05
	0.04	0.22	0.08	-	0.07
	0.1	-	0.14	0.57	0.13
	0.15	-	0.19	-	0.18
	0.25	-	0.29	-	0.28
Wheel slip first peak RR, (-)	0.02	-	0.06	-	0.05
	0.04	0.19	0.08	-	0.07
	0.1	-	0.14	0.58	0.13
	0.15	-	0.19	-	0.18
	0.25	-	0.29	-	0.28
Braking distance, (m)	0.02	-	55.8	-	50.8
	0.04	86.1	57.7	-	41.9
	0.1	-	63.9	46.5	39.6
	0.15	-	67.0	-	40.1
	0.25	-	70.4	-	41.5
WSCIP, (-)	0.02	-	1.4	-	0.9
	0.04	1	1.4	-	1.1
	0.1	-	1.3	1	1.1
	0.15	-	1.2	-	1.1
	0.25	-	1.2	-	1.1
Jerk STD, (m/s^3)	0.02	-	2.2	-	8.5
	0.04	5.2	2.5	-	2.8
	0.1	-	2.2	9.1	3.2
	0.15	-	2.1	-	4.7
	0.25	-	2.0	-	5.4

Table D.3 WSC numerical evaluation for various reference wheel slip values: vehicle with decoupled electro-hydraulic brake system

		Low road friction				High road friction			
Evaluation criterion	λ^*	RB	PI	SMPI	ISM	RB	PI	SMPI	ISM
Wheel slip FL RMSD, (-)	0.02	-	0.02	0.02	0.01	-	0.01	0.01	0.01
	0.04	-	0.02	0.03	0.02	-	0.01	0.01	0.01
	0.1	-	0.03	0.04	0.03	-	0.01	0.02	0.04
	0.15	-	0.03	0.03	0.04	-	0.03	0.04	0.07
	0.25	-	0.02	0.02	0.06	-	0.05	0.05	0.11
Wheel slip FR RMSD, (-)	0.02	-	0.02	0.02	0.01	-	0.01	0.01	0.01
	0.04	-	0.02	0.03	0.02	-	0.01	0.01	0.01
	0.1	-	0.02	0.04	0.03	-	0.01	0.01	0.04
	0.15	-	0.02	0.03	0.04	-	0.03	0.03	0.07
	0.25	-	0.02	0.02	0.06	-	0.05	0.05	0.11
Wheel slip RL RMSD, (-)	0.02	-	0.01	0.01	0.01	-	0.01	0.01	0.01
	0.04	-	0.01	0.01	0.01	-	0.01	0.01	0.01
	0.1	-	0.01	0.02	0.03	-	0.01	0.01	0.04
	0.15	-	0.02	0.02	0.05	-	0.02	0.02	0.06
	0.25	-	0.03	0.01	0.08	-	0.02	0.04	0.12
Wheel slip RR RMSD, (-)	0.02	-	0.01	0.01	0.01	-	0.01	0.01	0.01
	0.04	-	0.01	0.01	0.01	-	0.01	0.01	0.01
	0.1	-	0.01	0.02	0.03	-	0.01	0.01	0.04
	0.15	-	0.01	0.01	0.04	-	0.02	0.01	0.06
	0.25	-	0.01	0.01	0.07	-	0.03	0.03	0.12
Wheel slip first peak FL, (-)	0.02	-	0.1	0.1	0.08	-	0.04	0.04	0.04
	0.04	0.47	0.12	0.12	0.10	-	0.06	0.06	0.06
	0.1	-	0.40	0.18	0.17	0.62	0.14	0.14	0.14
	0.15	-	0.40	0.23	0.23	-	0.20	0.20	0.20
	0.25	-	0.40	0.36	0.36	-	0.32	0.31	0.32
Wheel slip first peak FR, (-)	0.02	-	0.10	0.1	0.09	-	0.05	0.04	0.04
	0.04	0.47	0.12	0.12	0.11	-	0.07	0.06	0.06
	0.1	-	0.18	0.18	0.17	0.63	0.15	0.15	0.15
	0.15	-	0.24	0.24	0.24	-	0.21	0.21	0.21
	0.25	-	0.37	0.37	0.36	-	0.32	0.31	0.31
Wheel slip first peak RL, (-)	0.02	-	0.05	0.04	0.04	-	0.04	0.04	0.03
	0.04	0.14	0.07	0.07	0.07	-	0.06	0.06	0.06
	0.1	-	0.15	0.14	0.15	0.57	0.14	0.14	0.14
	0.15	-	0.22	0.20	0.21	-	0.20	0.20	0.20
	0.25	-	0.34	0.33	0.33	-	0.31	0.31	0.31
Wheel slip first peak RR, (-)	0.02	-	0.05	0.04	0.04	-	0.04	0.04	0.03
	0.04	0.12	0.07	0.06	0.06	-	0.06	0.06	0.06
	0.1	-	0.15	0.14	0.15	0.58	0.14	0.13	0.14
	0.15	-	0.22	0.20	0.21	-	0.20	0.20	0.20
	0.25	-	0.33	0.32	0.33	-	0.32	0.31	0.31
Braking distance, (m)	0.02	-	35.7	35.6	35.7	-	52.0	52.0	53.6
	0.04	55.9	35.0	35.1	34.8	-	43.6	43.6	43.8
	0.1	-	37.5	37.5	37.4	46.5	41.2	41.2	41.2
	0.15	-	39.2	39.2	39.2	-	41.7	41.6	41.6
	0.25	-	41.5	41.5	41.5	-	43.1	43.0	43.0
WSCIP, (-)	0.02	-	1.5	1.5	1.5	-	1.1	1.1	1.1
	0.04	1	1.5	1.5	1.5	-	1.4	1.4	1.4
	0.1	-	1.4	1.4	1.4	1	1.5	1.5	1.4
	0.15	-	1.4	1.4	1.4	-	1.4	1.4	1.4
	0.25	-	1.3	1.3	1.3	-	1.4	1.4	1.4
Jerk STD, (m/s^3)	0.02	-	1.0	1.1	1.0	-	4.8	4.9	4.5
	0.04	7.4	1.2	1.2	1.2	-	4.1	4.0	4.1
	0.1	-	1.2	1.5	1.2	9.1	4.4	4.3	4.4
	0.15	-	1.1	1.2	1.2	-	4.4	4.9	4.6
	0.25	-	0.9	0.9	0.9	-	4.3	4.5	4.6

Appendix E

Numerical assessment of hardware-in-the-loop test results

Table E.1 WSC numerical evaluation of hardware-in-the-loop tests for the vehicle with decoupled electro-hydraulic brake system

	Low road friction			High road friction		
Evaluation criterion	PI	SMPI	ISM	PI	SMPI	ISM
Wheel slip FL RMSD, (-)	0.15	0.06	0.08	0.16	0.12	0.12
Wheel slip FR RMSD, (-)	0.10	0.05	0.03	0.26	0.23	0.23
Wheel slip RL RMSD, (-)	0.15	0.05	0.02	0.21	0.18	0.17
Wheel slip RR RMSD, (-)	0.13	0.07	0.08	0.21	0.19	0.19
Wheel slip first peak FL, (-)	0.11	0.11	0.09	0.18	0.12	0.12
Wheel slip first peak FR, (-)	0.11	0.08	0.09	0.13	0.18	0.13
Wheel slip first peak RL, (-)	0.07	0.06	0.06	0.26	0.24	0.23
Wheel slip first peak RR, (-)	0.08	0.07	0.07	0.24	0.25	0.23
Median braking distance, (m)	36.9	36.3	36.3	43.8	43.7	43.4
Max. braking distance, (m)	36.9	36.3	36.4	44.0	43.7	43.8
Min. braking distance, (m)	36.1	36.3	36.2	43.6	43.6	43.2
Jerk STD, (m/s^3)	2.5	2.6	2.1	5.4	5.3	4.7

Appendix F

Validation of vehicle state observer

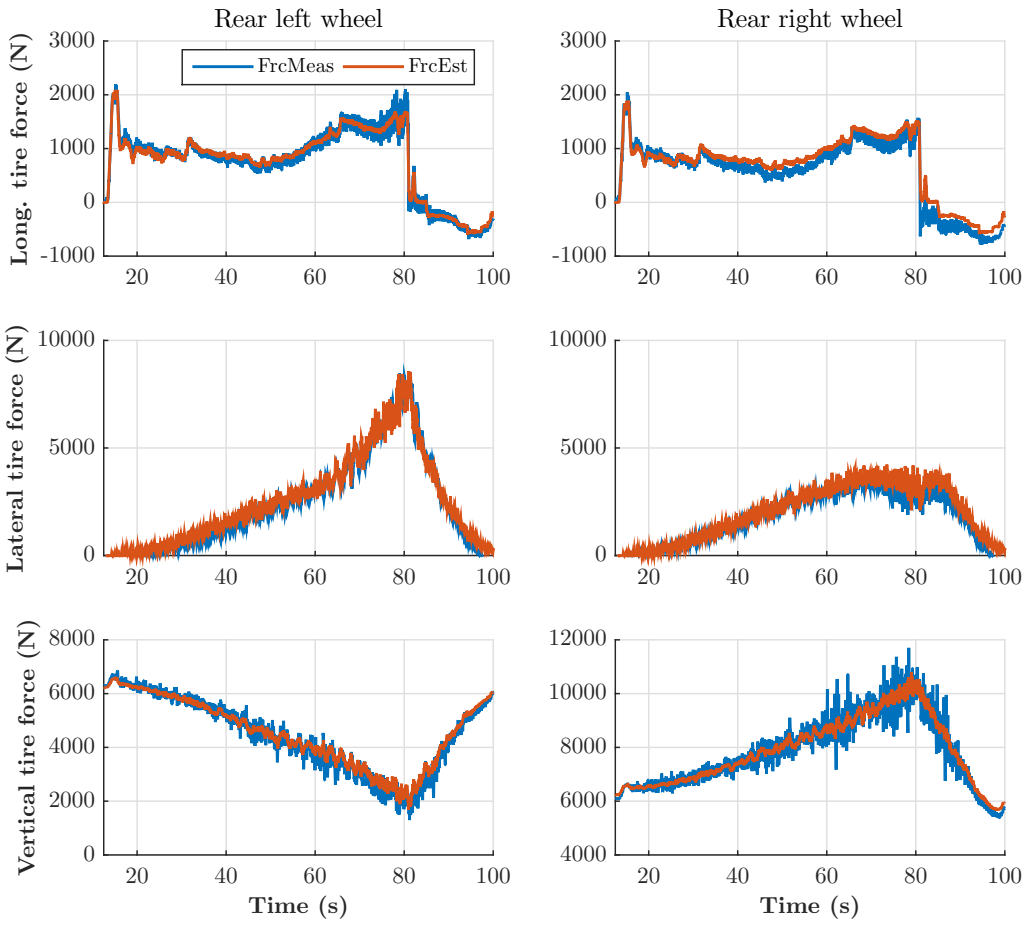

Fig. F.1 Validation of the state estimator during steady cornering maneuver: longitudinal, lateral and vertical tire forces

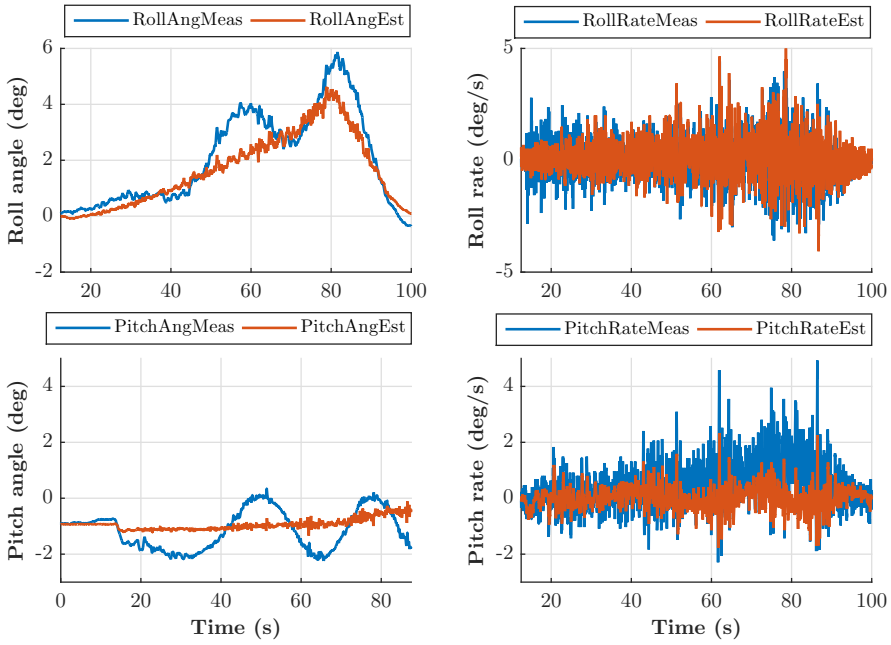

Fig. F.2 Validation of the state estimator during steady cornering maneuver: pitch and roll motion

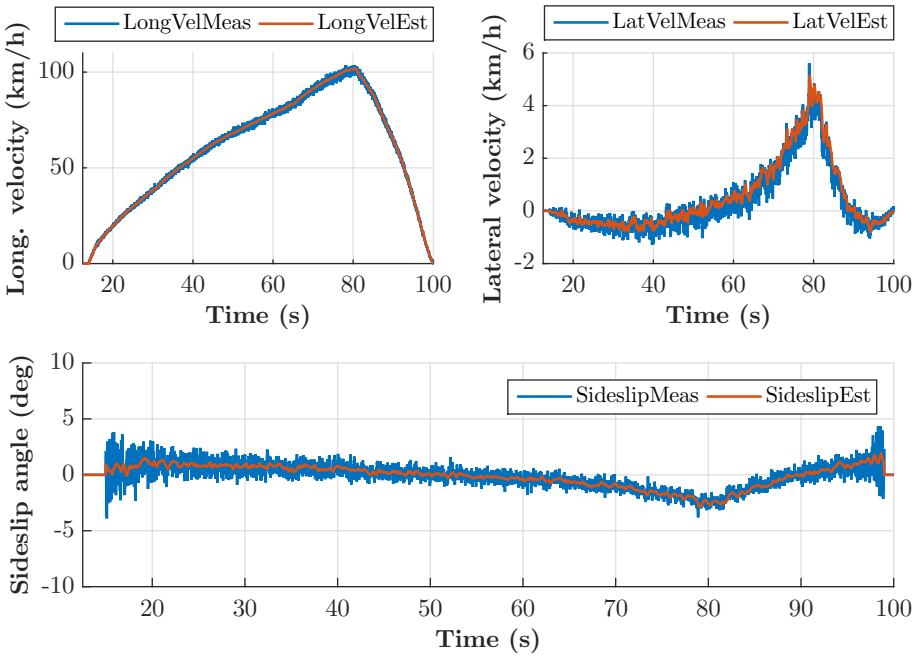

Fig. F.3 Validation of the state estimator during steady cornering maneuver: sideslip angle, longitudinal and lateral velocity

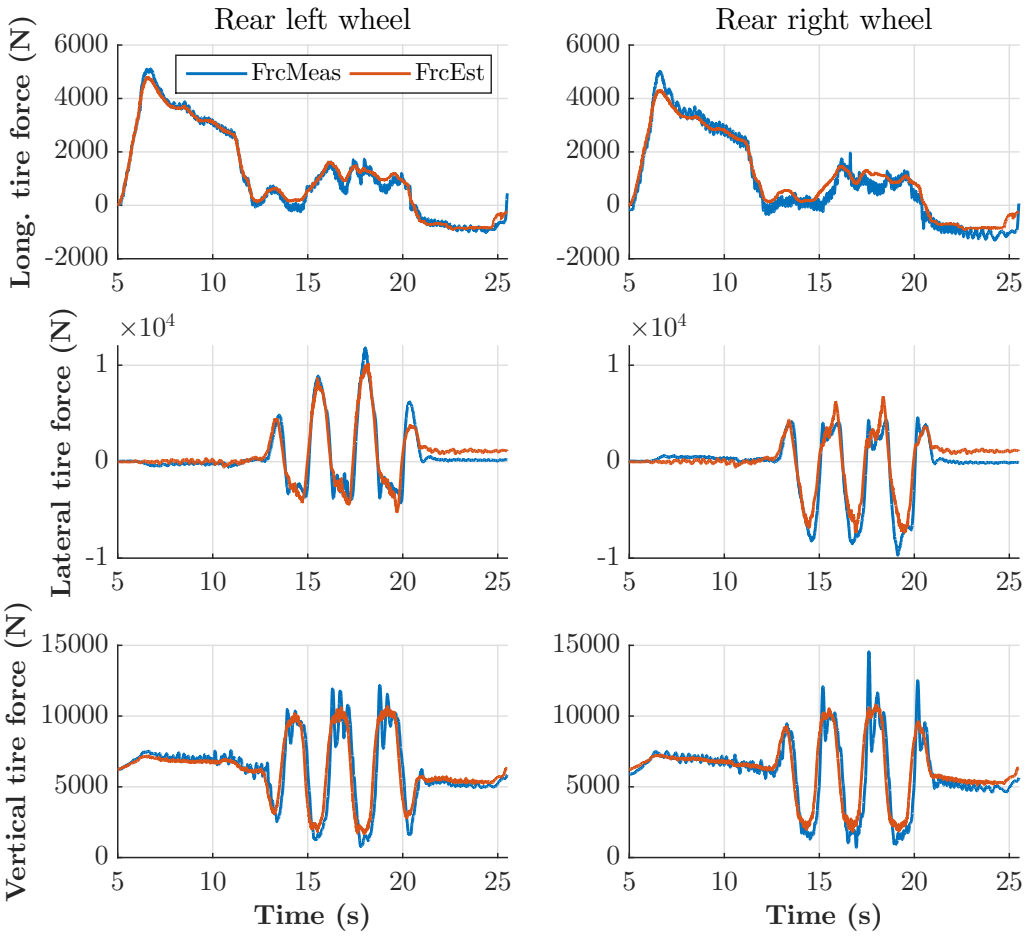

Fig. F.4 Validation of the state estimator during step response maneuver: longitudinal, lateral and vertical tire forces

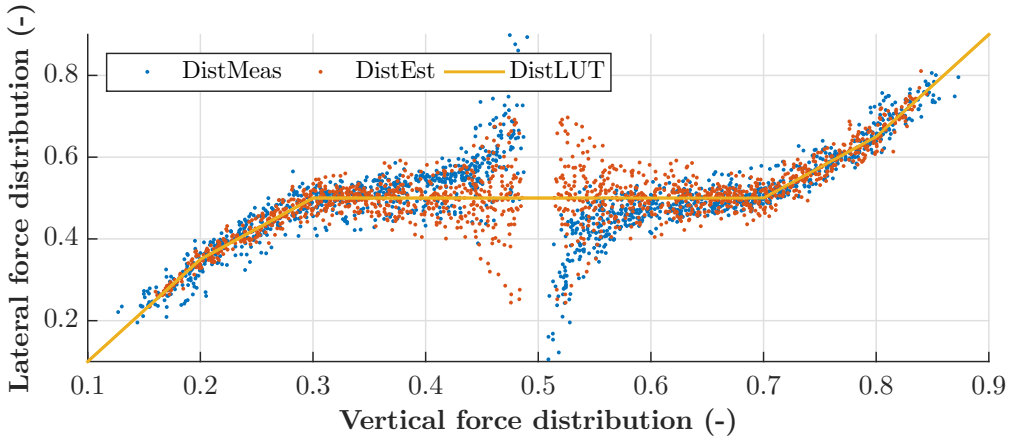

Fig. F.5 Lateral and vertical tire forces distribution between left and right tires: lookup-table for combined slip cases

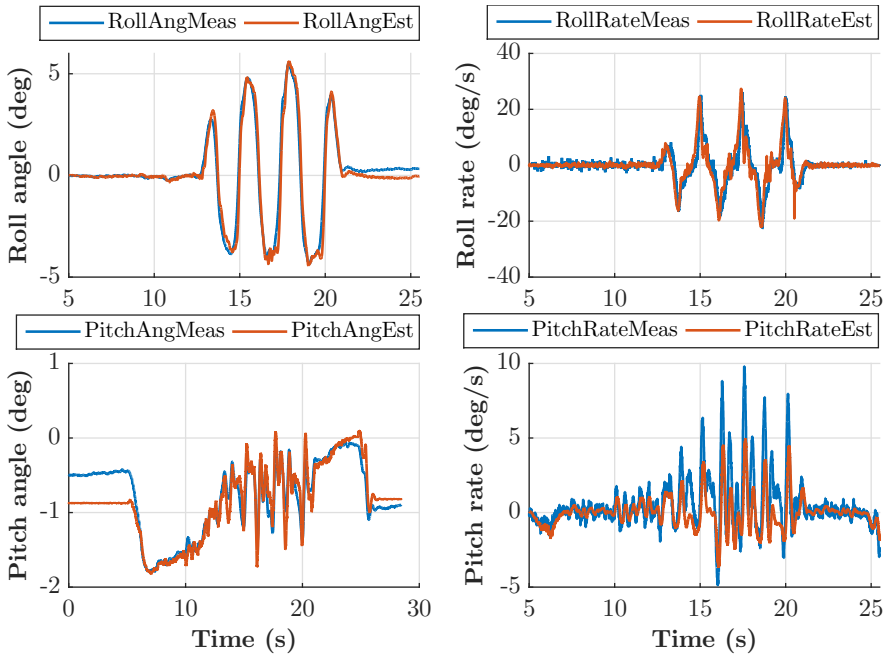

Fig. F.6 Validation of the state estimator during step response maneuver: pitch and roll motion

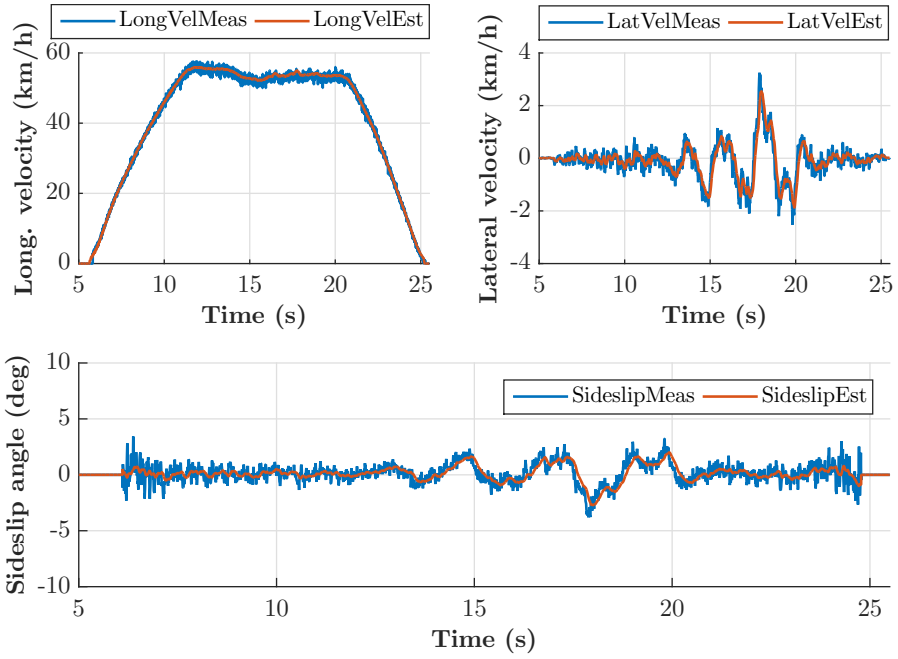

Fig. F.7 Validation of the state estimator during step response maneuver: sideslip angle, longitudinal and lateral velocity

Appendix G

Numerical assessment of road tests with vehicle demonstrators

Table G.1 WSC numerical evaluation for the braking in low friction conditions with OBMs and brake blending

Evaluation criterion	Rule-based EHB	Rule-based DEHB	Continuous OBM and DEHB
Mean wheel slip FL, (-)	0.24	0.14	0.14
Mean wheel slip FR, (-)	0.23	0.14	0.14
Mean wheel slip RL, (-)	0.08	0.08	0.10
Mean wheel slip RR, (-)	0.20	0.09	0.10
Wheel slip first peak FL, (-)	0.40	0.57	0.12
Wheel slip first peak FR, (-)	0.35	0.58	0.12
Wheel slip first peak RL, (-)	0.36	0.33	0.09
Wheel slip first peak RR, (-)	0.38	0.29	0.08
Mean deceleration, (m/s^2)	1.4	1.4	1.9
Braking distance, (m)	100.2	100.7	80.7
ABSIP, (-)	1.4	1.4	1.7
Jerk STD, (m/s^3)	0.7	0.8	0.3

Table G.2 WSC numerical evaluation for the braking in low friction conditions with DEHB

Evaluation metric	Control						
	RB	PI	PI RA	SMPI	SMPI RA	ISM	ISM RA
Low road friction conditions							
Median braking distance (m)	49.9	37.2	36.9	35.6	35.3	35.2	34.5
Max. braking distance (m)	54.4	37.5	37.7	35.9	35.9	36.0	35.7
Min. braking distance (m)	45.3	34.8	34.7	33.6	33.6	33.7	33.7
Wheel slip FL RMSD (-)	-	0.05	0.05	0.04	0.04	0.03	0.03
Wheel slip FR RMSD (-)	-	0.06	0.06	0.04	0.04	0.04	0.03
Wheel slip RL RMSD (-)	-	0.03	0.03	0.03	0.03	0.02	0.02
Wheel slip RR RMSD (-)	-	0.03	0.03	0.03	0.03	0.03	0.02
Deceleration STD (m/s^2)	0.11	0.06	0.05	0.06	0.05	0.06	0.05
High road friction conditions							
Median braking distance (m)	44.1	43.6	42.6	42.4	42.3	40.7	40.1
Max. braking distance (m)	44.5	44.7	43.9	43.3	43.1	41.1	40.2
Min. braking distance (m)	43.2	42.6	41.9	41.7	41.7	40.1	39.2
Wheel slip FL RMSD (-)	-	0.14	0.18	0.08	0.08	0.04	0.03
Wheel slip FR RMSD (-)	-	0.14	0.18	0.09	0.10	0.05	0.04
Wheel slip RL RMSD (-)	-	0.12	0.13	0.04	0.03	0.04	0.04
Wheel slip RR RMSD (-)	-	0.12	0.14	0.04	0.04	0.05	0.04
Deceleration STD (m/s^2)	0.11	0.12	0.11	0.11	0.11	0.08	0.08

Table G.3 WSC numerical evaluation for the braking in low friction conditions with IWMs

Evaluation criterion	FOSM	VSPI	ISM	CTA
Wheel slip FL RMSD, (-)	0.02	0.03	0.03	0.03
Wheel slip FR RMSD, (-)	0.03	0.03	0.02	0.02
Wheel slip RL RMSD, (-)	0.03	0.04	0.03	0.04
Wheel slip RR RMSD, (-)	0.03	0.03	0.02	0.02
Wheel slip first peak FL, (-)	0.08	0.12	0.10	0.15
Wheel slip first peak FR, (-)	0.06	0.11	0.11	0.14
Wheel slip first peak RL, (-)	0.09	0.15	0.13	0.18
Wheel slip first peak RR, (-)	0.06	0.1	0.07	0.08
Mean deceleration, (m/s^2)	1.9	1.6	2.0	2.0
Braking distance, (m)	13.1	16.2	12.8	12.3
Deceleration STD, (m/s^2)	0.76	0.59	0.62	0.58